

ORNL/TM-10219
ENDF-344

**OAK RIDGE
NATIONAL
LABORATORY**

MARTIN MARIETTA

**Calculated Neutron-Induced
Cross Sections for $^{58,60}\text{Ni}$ from
1 to 20 MeV and Comparisons
with Experiments**

D. M. Hetrick
C. Y. Fu
D. C. Larson

OPERATED BY
MARTIN MARIETTA ENERGY SYSTEMS, INC.
FOR THE UNITED STATES
DEPARTMENT OF ENERGY

Printed in the United States of America. Available from
National Technical Information Service
U.S. Department of Commerce
5285 Port Royal Road, Springfield, Virginia 22161
NTIS price codes—Printed Copy: A06 Microfiche A01

This report was prepared as an account of work sponsored by an agency of the United States Government. Neither the United States Government nor any agency thereof, nor any of their employees, makes any warranty, express or implied, or assumes any legal liability or responsibility for the accuracy, completeness, or usefulness of any information, apparatus, product, or process disclosed, or represents that its use would not infringe privately owned rights. Reference herein to any specific commercial product, process, or service by trade name, trademark, manufacturer, or otherwise, does not necessarily constitute or imply its endorsement, recommendation, or favoring by the United States Government or any agency thereof. The views and opinions of authors expressed herein do not necessarily state or reflect those of the United States Government or any agency thereof.

Engineering Physics and Mathematics Division

**CALCULATED NEUTRON-INDUCED CROSS SECTIONS FOR $^{58,60}\text{Ni}$
FROM 1 TO 20 MeV AND COMPARISONS WITH EXPERIMENTS**

D. M. Hetrick,* C. Y. Fu, and D. C. Larson

Manuscript Completed — March 15, 1987
Date Published — June 1987

NOTICE This document contains information of a preliminary nature.
It is subject to revision or correction and therefore does not represent a
final report.

*Computing and Telecommunications Division

Prepared for the
Office of Basic Energy Sciences

Prepared by the
OAK RIDGE NATIONAL LABORATORY
Oak Ridge, Tennessee 37831
operated by
MARTIN MARIETTA ENERGY SYSTEMS, INC.
for the
U.S. DEPARTMENT OF ENERGY
under contract DE-AC05-84OR21400

CONTENTS

List of Tables	v
List of Figures	vii
Acknowledgments	xiii
Abstract	1
1. Introduction	1
2. Parameter Determination	2
2.1 Neutron Optical-Model Potential	2
2.2 Charged-Particle Optical-Model Parameters	2
2.3 The Direct Reaction Model and Parameters	2
2.4 Discrete Energy Levels and Level-Density Parameters	2
2.5 Giant Dipole Resonance Parameters	15
2.6 (n,t) , $(n,^3\text{He})$, and (n,d) Cross	
Sections" 15 .sp	
3. Computational Methods and Procedures	16
4. Comparison of Calculations with Experiments	16
4.1 Total Cross Section	16
4.2 Nonelastic Cross Section	18
4.3 Elastic Cross Section	18
4.4 Total Inelastic Scattering Cross Section	18
4.5 Angular Distributions for Inelastic Scattering	18
4.6 Inelastic Scattering to Discrete Levels	40
4.7 Angular Distributions of Neutron Production Cross Sections	40
4.8 Neutron Emission Spectra	40
4.9 Proton and Alpha-Particle Emission Spectra	48
4.10 Binary and Tertiary Reaction Cross Sections	48
4.11 Gamma-Ray Excitation Functions	61
4.12 Integrated Yield of Secondary Gamma Rays	61
4.13 Gamma-Ray Production Cross Sections and Spectral Comparisons	61
5. Comparison of Calculation with ENDF/B-V	76
6. Summary	76
References	83

LIST OF TABLES

Table 1. Neutron optical-model parameters	3
Table 2. Proton optical-model parameters	4
Table 3. Alpha optical-model parameters	4
Table 4. Deformation parameters of ^{58}Ni levels	5
Table 5. Deformation parameters of ^{60}Ni levels	5
Table 6. Energy levels and gamma-ray branching ratios of ^{58}Ni	8
Table 7. Energy levels and gamma-ray branching ratios of ^{58}Co	8
Table 8. Energy levels and gamma-ray branching ratios of ^{55}Fe	9
Table 9. Energy levels and gamma-ray branching ratios of ^{57}Co	9
Table 10. Energy levels and gamma-ray branching ratios of ^{54}Fe	10
Table 11. Energy levels and gamma-ray branching ratios of ^{57}Ni	10
Table 12. Energy levels and gamma-ray branching ratios of ^{60}Ni	11
Table 13. Energy levels and gamma-ray branching ratios of ^{60}Co	11
Table 14. Energy levels and gamma-ray branching ratios of ^{57}Fe	12
Table 15. Energy levels and gamma-ray branching ratios of ^{59}Co	12
Table 16. Energy levels and gamma-ray branching ratios of ^{56}Fe	13
Table 17. Energy levels and gamma-ray branching ratios of ^{59}Ni	14
Table 18. Energy levels of ^{61}Ni	14
Table 19. Level density parameters	15

LIST OF FIGURES

Fig. 1.	Calculated direct inelastic excitation cross sections for ^{58}Ni	6
Fig. 2.	Calculated direct inelastic excitation cross sections for ^{60}Ni	6
Fig. 3.	Comparison of calculated and experimental total cross sections for Ni	17
Fig. 4.	Comparison of calculated and experimental nonelastic cross sections for Ni	19
Fig. 5.	Comparison of calculated and experimental elastic cross sections for ^{58}Ni	20
Fig. 6.	Comparison of calculated and experimental elastic cross sections for ^{60}Ni	20
Fig. 7.	Comparison of calculated and experimental elastic cross sections for ^{nat}Ni	21
Fig. 8.	Comparison of calculated and experimental total inelastic scattering cross sections for ^{58}Ni	22
Fig. 9.	Comparison of calculated and experimental total inelastic scattering cross sections for ^{60}Ni	22
Fig. 10.	Comparison of calculated and experimental total inelastic scattering cross sections for ^{nat}Ni	23
Fig. 11.	Comparison of calculated and experimental differential cross sections for exciting the 1.454-MeV level at $E_n = 2.0$ MeV	24
Fig. 12.	Comparison of calculated and experimental differential cross sections for exciting the 1.454-MeV level at $E_n = 2.5$ MeV	24
Fig. 13.	Comparison of calculated and experimental differential cross sections for exciting the 1.454-MeV level at $E_n = 3.0$ MeV	25
Fig. 14.	Comparison of calculated and experimental differential cross sections for exciting the 1.454-MeV level at $E_n = 5.0$ MeV	25
Fig. 15.	Comparison of calculated and experimental differential cross sections for exciting the 1.454-MeV level at $E_n = 5.5$ MeV	26
Fig. 16.	Comparison of calculated and experimental differential cross sections for exciting the 2.459-MeV level at $E_n = 3.0$ MeV	26
Fig. 17.	Comparison of calculated and experimental differential cross sections for exciting the 2.459-MeV level at $E_n = 5.0$ MeV	27
Fig. 18.	Comparison of calculated and experimental differential cross sections for exciting the 2.459-MeV level at $E_n = 5.5$ MeV	27
Fig. 19.	Comparison of calculated and experimental differential cross sections for exciting the 2.776-, 2.903-, 2.943-, and 3.038-MeV levels at $E_n = 5.0$ MeV	28

Fig. 20.	Comparison of calculated and experimental differential cross sections for exciting the 2.776-, 2.903-, 2.943-, and 3.038-MeV levels at $E_n = 5.5$ MeV	28
Fig. 21.	Comparison of calculated and experimental differential cross sections for exciting the 3.265- and 3.421-MeV levels at $E_n = 5.0$ MeV	29
Fig. 22.	Comparison of calculated and experimental differential cross sections for exciting the 3.265- and 3.421-MeV levels at $E_n = 5.5$ MeV	29
Fig. 23.	Comparison of calculated and experimental differential cross sections for exciting the 1.333-MeV level at $E_n = 2.0$ MeV	30
Fig. 24.	Comparison of calculated and experimental differential cross sections for exciting the 1.333-MeV level at $E_n = 2.5$ MeV	30
Fig. 25.	Comparison of calculated and experimental differential cross sections for exciting the 1.333-MeV level at $E_n = 3.0$ MeV	31
Fig. 26.	Comparison of calculated and experimental differential cross sections for exciting the 1.333-MeV level at $E_n = 4.0$ MeV	31
Fig. 27.	Comparison of calculated and experimental differential cross sections for exciting the 1.333-MeV level at $E_n = 5.0$ MeV	32
Fig. 28.	Comparison of calculated and experimental differential cross sections for exciting the 1.333-MeV level at $E_n = 6.5$ MeV	32
Fig. 29.	Comparison of calculated and experimental differential cross sections for exciting the 1.333-MeV level at $E_n = 7.5$ MeV	33
Fig. 30.	Comparison of calculated and experimental differential cross sections for exciting the 1.333-MeV level at $E_n = 8.5$ MeV	33
Fig. 31.	Comparison of calculated and experimental differential cross sections for exciting the 2.159-MeV level at $E_n = 3.0$ MeV	34
Fig. 32.	Comparison of calculated and experimental differential cross sections for exciting the 2.159-MeV level at $E_n = 3.25$ MeV	34
Fig. 33.	Comparison of calculated and experimental differential cross sections for exciting the 2.159- and 2.285-MeV levels at $E_n = 4.0$ MeV	35
Fig. 34.	Comparison of calculated and experimental differential cross sections for exciting the 2.159- and 2.285-MeV levels at $E_n = 5.0$ MeV	35
Fig. 35.	Comparison of calculated and experimental differential cross sections for exciting the 2.159- and 2.285-MeV levels at $E_n = 6.5$ MeV	36
Fig. 36.	Comparison of calculated and experimental differential cross sections for exciting the 2.159- and 2.285-MeV levels at $E_n = 7.5$ MeV	36

Fig. 37.	Comparison of calculated and experimental differential cross sections for exciting the 2.159- and 2.285-MeV levels at $E_n = 8.5$ MeV	37
Fig. 38.	Comparison of calculated and experimental differential cross sections for exciting the 2.506-MeV level at $E_n = 3.26$ MeV	37
Fig. 39.	Comparison of calculated and experimental differential cross sections for exciting the 2.506- and 2.626-MeV levels at $E_n = 4.0$ MeV	38
Fig. 40.	Comparison of calculated and experimental differential cross sections for exciting the 2.506- and 2.626-MeV levels at $E_n = 5.0$ MeV	38
Fig. 41.	Comparison of calculated and experimental differential cross sections for exciting the 2.506- and 2.626-MeV levels at $E_n = 6.5$ MeV	39
Fig. 42.	Comparison of calculated and experimental differential cross sections for exciting the 2.506- and 2.626-MeV levels at $E_n = 7.5$ MeV	39
Fig. 43.	Comparison of calculated and experimental differential cross sections for exciting the 2.506- and 2.626-MeV levels at $E_n = 8.5$ MeV	40
Fig. 44.	Comparison of calculated and experimental $^{58}\text{Ni}(n,n')$ cross sections for exciting the 1.454-MeV level	41
Fig. 45.	Comparison of calculated and experimental $^{58}\text{Ni}(n,n')$ cross sections for exciting the 2.459-MeV level	41
Fig. 46.	Comparison of calculated and experimental $^{58}\text{Ni}(n,n')$ cross sections for exciting the 2.776-MeV level	42
Fig. 47.	Comparison of calculated and experimental $^{58}\text{Ni}(n,n')$ cross sections for exciting the 2.776-, 2.903-, 2.943-, and 3.038-MeV levels	42
Fig. 48.	Comparison of calculated and experimental $^{58}\text{Ni}(n,n')$ cross sections for exciting the 3.265- and 3.421-MeV levels	43
Fig. 49.	Comparison of calculated and experimental $^{60}\text{Ni}(n,n')$ cross sections for exciting the 1.333-MeV level	43
Fig. 50.	Comparison of calculated and experimental $^{60}\text{Ni}(n,n')$ cross sections for exciting the 2.159-MeV level	44
Fig. 51.	Comparison of calculated and experimental $^{60}\text{Ni}(n,n')$ cross sections for exciting the 2.159- and 2.285-MeV levels	44
Fig. 52.	Comparison of calculated and experimental $^{60}\text{Ni}(n,n')$ cross sections for exciting the 2.506- and 2.626-MeV levels	45
Fig. 53.	Comparison of calculated and experimental neutron production cross sections	46

Fig. 54. Neutron emission spectra from the TNG calculation compared with experimental data. The data of Clayeux and Voignier (CL72) and Mathur et al. (MA69) were taken at 90°, the data of Takahashi et al. (TA83) were taken at 80°, and the other measured data sets shown (HE75, VO80, and SA72) are angle integrated. Contributions from the various neutron-producing components are shown (they sum to the total). The curves labeled (n,np) and $(n,n\alpha)$ include the (n,pn) and $(n,\alpha n)$ components, respectively	47
Fig. 55. Comparison of calculated experimental proton production spectra for ^{58}Ni . The measurements were taken at incident energies of 14.8 and 14.1 MeV; the TNG calculation was for $E_n = 14.5$ MeV. The data of Grimes et al. (GR79, HA77) are angle integrated; the data of Colli et al. (CO62) were taken at 15°	49
Fig. 56. Comparison of calculated and experimental alpha production spectra for ^{58}Ni . The measurement was taken at an incident energy of 14.8 MeV, the TNG calculation was for $E_n = 14.5$ MeV	50
Fig. 57. Comparison of calculated and experimental proton production spectra for ^{60}Ni . The measurements were taken at incident energies of 14.8 and 14.1 MeV; the TNG calculation was for $E_n = 14.5$ MeV. The data of Grimes et al. (GR79, HA77) are angle integrated; the data of Colli et al. (CO62) were taken at 15°	51
Fig. 58. Comparison of calculated and experimental alpha production spectra for ^{60}Ni . The measurements were taken at incident energies of 14.8 and 14.1 MeV and are angle integrated; the TNG calculation was for $E_n = 14.5$ MeV.	52
Fig. 59. Comparison of calculated and experimental $^{58}\text{Ni}(n,p)$ cross sections	53
Fig. 60. Comparison of calculated and experimental $^{60}\text{Ni}(n,p)$ cross sections	54
Fig. 61. Comparison of calculated and experimental $^{58}\text{Ni}(n,np) + (n,pn)$ cross sections	55
Fig. 62. Comparison of calculated and experimental cross sections for the total proton emission of ^{58}Ni . The $^{58}\text{Ni}(n,p)$ data from Fig. 59 for incident energies less than approximately 9.0 MeV could have been included in this figure.	56
Fig. 63. Comparison of calculated and experimental cross sections for the total proton emission of ^{60}Ni . The $^{60}\text{Ni}(n,p)$ data from Fig. 60 for incident energies less than approximately 10.0 MeV could have been included in this figure.	56
Fig. 64. Comparison of calculated and experimental $^{58}\text{Ni}(n,2n)$ cross sections	57
Fig. 65. Comparison of calculated and experimental $^{nat}\text{Ni}(n,2n)$ cross sections. The solid line is the sum of the TNG calculations for $^{58}\text{Ni}(n,2n)$ and $^{60}\text{Ni}(n,2n)$ multiplied by 0.71 and 0.29 respectively. The dashed line is the sum of the TNG calculations for ^{58}Ni and ^{60}Ni added to the calculations of Divadeenam (DI79) for ^{61}Ni , ^{62}Ni , and ^{64}Ni (each were multiplied by its fractional natural abundance).	58
Fig. 66. Comparison of calculated and experimental $^{58}\text{Ni}(n,\alpha)$ cross sections	59
Fig. 67. Comparison of calculated and experimental cross sections for the total alpha emission of ^{58}Ni	59

Fig. 68. Comparison of calculated and experimental cross sections for the total alpha emission of ^{60}Ni	60
Fig. 69. Comparison of calculated and experimental $^{nat}\text{Ni}(n,\alpha)$ cross sections	60
Fig. 70. Comparison of calculated and experimental data of the excitation function for the $E_\gamma = 1.454$ MeV transition following $^{58}\text{Ni}(n,n'\gamma)$	62
Fig. 71. Comparison of calculated and experimental data of the excitation function for the $E_\gamma = 1.005$ MeV transition following $^{58}\text{Ni}(n,n'\gamma)$	62
Fig. 72. Comparison of calculated and experimental data of the excitation function for the $E_\gamma = 1.322$ MeV transition following $^{58}\text{Ni}(n,n'\gamma)$	63
Fig. 73. Comparison of calculated and experimental data of the excitation function for the $E_\gamma = 1.449$ MeV transition following $^{58}\text{Ni}(n,n'\gamma)$	63
Fig. 74. Comparison of calculated and experimental data of the excitation function for the $E_\gamma = 1.584$ MeV transition following $^{58}\text{Ni}(n,n'\gamma)$	64
Fig. 75. Comparison of calculated and experimental data of the excitation function for the $E_\gamma = 1.811$ MeV transition following $^{58}\text{Ni}(n,n'\gamma)$	64
Fig. 76. Comparison of calculated and experimental data of the excitation function for the $E_\gamma = 1.333$ MeV transition following $^{60}\text{Ni}(n,n'\gamma)$	65
Fig. 77. Comparison of calculated and experimental data of the excitation function for the $E_\gamma = 0.826$ MeV transition following $^{60}\text{Ni}(n,n'\gamma)$	66
Fig. 78. Comparison of calculated and experimental data of the excitation function for the $E_\gamma = 0.467$ MeV transition following $^{60}\text{Ni}(n,n'\gamma)$	66
Fig. 79. Comparison of calculated and experimental data of the excitation function for the $E_\gamma = 1.791$ MeV transition following $^{60}\text{Ni}(n,n'\gamma)$	67
Fig. 80. Comparison of calculated and experimental data of the excitation function for the $E_\gamma = 0.952$ MeV transition following $^{60}\text{Ni}(n,n'\gamma)$	67
Fig. 81. Comparison of calculated and experimental data of the excitation function for the $E_\gamma = 1.293$ MeV transition following $^{60}\text{Ni}(n,n'\gamma)$	68
Fig. 82. Comparison of calculated and experimental data of the excitation function for the $E_\gamma = 1.937$ MeV transition following $^{60}\text{Ni}(n,n'\gamma)$	68
Fig. 83. Comparison of calculated and experimental data of the excitation function for the $E_\gamma = 1.985$ MeV transition following $^{60}\text{Ni}(n,n'\gamma)$	69
Fig. 84. Comparison of calculated and experimental data of the excitation function for the $E_\gamma = 0.644$ MeV transition following $^{60}\text{Ni}(n,n'\gamma)$	69
Fig. 85. Integrated yield of secondary gamma rays with $E_\gamma > 1.00$ MeV as a function of incident neutron energy. Gamma-ray scattering angles θ_γ are given in the legend	70

Fig. 86. Secondary gamma-ray spectra versus gamma-ray energy from the TNG calculation (incident energy $E_n = 5.5$ MeV) compared with the data of Dickens et al. (DI73)	71
Fig. 87. Secondary gamma-ray spectra versus gamma-ray energy from the TNG calculation (incident energy $E_n = 9.5$ MeV) compared with the data of Dickens et al. (DI73)	72
Fig. 88. Secondary gamma-ray spectra versus gamma-ray energy from the TNG calculation (incident energy $E_n = 14.5$ MeV) compared with the data of Dickens et al. (DI73)	73
Fig. 89. Secondary gamma-ray spectra versus gamma-ray energy from the TNG calculation (incident energy $E_n = 14.5$ MeV) compared with the data of Drake et al. (DR78)	74
Fig. 90. Secondary gamma-ray spectra versus gamma-ray energy from the TNG calculation (incident energy $E_n = 14.5$ MeV) compared with the data of Shin et al. (SH80)	75
Fig. 91. Comparison of the TNG calculation with ENDF/B-V for the total inelastic scattering cross section	77
Fig. 92. Comparison of the TNG calculation with ENDF/B-V for the integrated yield of secondary neutrons as a function of incident neutron energy. The elastic contribution is not included	77
Fig. 93. Comparison of (n,xn) from ENDF/B-V with the TNG calculation for incident neutron energy of 5.5 MeV	78
Fig. 94. Comparison of (n,xn) from ENDF/B-V with the TNG calculation for incident neutron energy of 9.5 MeV	78
Fig. 95. Comparison of (n,xn) from ENDF/B-V with the TNG calculation for incident neutron energy of 14.5 MeV	79
Fig. 96. Comparison of the TNG calculation with ENDF/B-V for the (n,p) cross section	79
Fig. 97. Comparison of the TNG calculation with ENDF/B-V for the (n,α) cross section	80
Fig. 98. Comparison of the TNG calculation with ENDF/B-V for the integrated yield of secondary gamma rays as a function of incident neutron energy	80
Fig. 99. Comparison of $(n,x\gamma)$ from ENDF/B-V with the TNG calculation for incident neutron energy of 5.5 MeV	81
Fig. 100. Comparison of $(n,x\gamma)$ from ENDF/B-V with the TNG calculation for incident neutron energy of 9.5 MeV	81
Fig. 101. Comparison of $(n,x\gamma)$ from ENDF/B-V with the TNG calculation for incident neutron energy of 14.5 MeV	82

ACKNOWLEDGMENTS

This research was sponsored jointly by the Office of Basic Energy Sciences and the Office of Fusion Energy, U.S. Department of Energy, under contract DE-AC05-84OR21400 with Martin Marietta Energy Systems, Inc.

We are grateful to Shirley White and Sue Damewood for preparing this report for publication.

CALCULATED NEUTRON-INDUCED CROSS SECTIONS FOR $^{58,60}\text{Ni}$ FROM 1 TO 20 MeV AND COMPARISONS WITH EXPERIMENTS

D. M. Hetrick, C. Y. Fu, and D. C. Larson

ABSTRACT

Nuclear model codes were used to compute cross sections for neutron-induced reactions on both ^{58}Ni and ^{60}Ni for incident energies from 1 to 20 MeV. The input parameters for the model codes were determined through analysis of experimental data in this energy region. Discussion of the models used, the input data, the resulting calculations, extensive comparisons to measured data, and comparisons to the Evaluated Nuclear Data File (ENDF/B-V) for Ni (MAT 1328) are included in this report.

1. INTRODUCTION

The nuclear data needs specified by the National Nuclear Data Center (NNDC) include evaluated neutron cross sections for nickel, an important material for fusion reactor applications. It has been shown that deficiencies exist for nickel in the Evaluated Nuclear Data File (ENDF/B-V) for the neutron emission spectra from contributing reactions (HE79). Since neutron-emission cross sections as a function of angle and energy are important for neutron-transport calculations for fusion-engineering feasibility demonstrations, an extensive effort was made to reproduce the rather sparse experimental data and use realistic models to provide reliable interpolation and extrapolation to other energy and angular regions where no data were available. Guided by experimental data, we have performed a comprehensive set of nuclear model calculations for neutron reactions on $^{58,60}\text{Ni}$ for incident energies between 1 and 20 MeV in which we have particularly addressed the NNDC requests for nickel as noted in Ref. ND83. This report documents these calculations, and these results, together with experimental data, will form the basis for the ENDF/B-VI evaluations for $^{58,60}\text{Ni}$.

Nuclear model codes were employed in this analysis. Several published optical-model parameter sets (WI64, PE76, KI85, HA82) were tried as input for the Hauser-Feshbach code TNG (FU80, FU80a, SH86) in order to determine which gave the best overall fit to measured data. The Distorted Wave Born Approximation (DWBA) program DWUCK (KU72) was used to compute direct-interaction cross sections needed as input for TNG. The applicability of TNG to cross-section evaluations has been extended as TNG is now capable of using variable energy bin widths for outgoing particle energies (SH86). The TNG code provides energy and angular distributions of particles emitted in the compound and precompound reactions, ensures consistency among all reactions, and maintains energy balance.

The optical-model parameter sets, discrete energy levels, and other parameters needed as input for TNG are discussed in Chapter 2. Chapter 3 includes a discussion of the computational methods and procedures for the calculations. Figures showing calculated results compared to measured data are given in Chapter 4, along with some brief discussions. In Chapter 5, the calculations are compared to cross sections from the ENDF/B-V evaluation for nickel. A short summary is given in Chapter 6.

2. PARAMETER DETERMINATION

2.1 NEUTRON OPTICAL-MODEL POTENTIAL

Since optical-model parameters are essential input for our nuclear model calculations, effort was spent to find a good documented set of neutron optical-model parameters for $n + {}^{58,60}\text{Ni}$ so as to reproduce the nonelastic, elastic, and total cross sections. Deficiencies exist for nickel in ENDF/B-V for the neutron emission spectra from contributing reactions (HE79). However, the elastic angular distributions in ENDF/B-V for nickel are in good agreement with measured data (DI79, BH74). Thus, we especially emphasized fitting the available nonelastic cross-section data, since for evaluation purposes measured data are used for the total cross section.

Several published neutron optical-model parameter sets (WI64, PE76, KI85, HA82) were tried as input to the Hauser-Feshbach code TNG (FU80, FU80a, SH86). Although the local neutron optical-model potential due to Harper and Alford (HA82) gave the best overall fit to measured data for the total cross section (LA80), the resulting calculated nonelastic cross section was approximately 25 percent too small in the energy range from 2 to 6 MeV compared to available measured data. However, the potential by Wilmore and Hodgson (WI64, PE76) resulted in a very good fit to the nonelastic cross section for incident energies from 1 to 20 MeV and a satisfactory fit to the total cross section (see Section 4). Other potentials that were tried (PE76, KI85, and for example, see YO85) did not fit the nonelastic, total, and some of the reaction cross sections as well. Therefore, the neutron optical-model potential by Wilmore and Hodgson was chosen and used as input to the TNG code for both ${}^{58}\text{Ni}$ and ${}^{60}\text{Ni}$. Values for this potential are given in Table 1.

2.2 CHARGED-PARTICLE OPTICAL-MODEL PARAMETERS

The proton optical-model parameters are taken from the work of Becchetti and Greenlees (BE69). The potential used for the protons is given in Table 2. Optical-model parameters for the alpha particles were taken from Huizenga and Igo (HU62). They are given in Table 3.

2.3 THE DIRECT REACTION MODEL AND PARAMETERS

The Distorted Wave Born Approximation (DWBA) program DWUCK (KU72) was used to calculate the direct-interaction component of the inelastic-scattering cross sections to a number of levels in ${}^{58,60}\text{Ni}$ for which information was available. Inputs to this code were the neutron optical-model parameters of Table 1 and the deformation parameters, β_2^2 , shown in Table 4 for ${}^{58}\text{Ni}$ and in Table 5 for ${}^{60}\text{Ni}$. β_2^2 values from numerous references (see Tables) were averaged to obtain the β_2^2 values shown in Tables 4 and 5. The resulting calculated direct inelastic excitation cross sections, shown in Figs. 1 and 2, were used as input to the TNG code for the purpose of including the direct interaction effects in the gamma-ray cascades calculation. All TNG results were automatically reduced to maintain the same total reaction cross section.

2.4 DISCRETE ENERGY LEVELS AND LEVEL-DENSITY PARAMETERS

The statistical-model calculations with TNG require a complete description of the energy levels of the residual nuclei for the various open channels. The low-energy region of excitation of these nuclei can be adequately described in terms of discrete levels for which we usually know the energy, spin and parity (J^π), and gamma-ray deexcitation branching ratios, hereinafter referred to as branching ratios.

Table 1. Neutron optical-model parameters

V (MeV)	$= 47.01 - 0.267E - 0.0018E^2$
W (MeV)	$= 0.0$
W_D (MeV)	$= 9.52 - 0.053E$
U (MeV)	$= 7.0$
r_v (fm)	$= 1.322 - 7.6A \times 10^{-4} + 4A^2 \times 10^{-6} - 8A^3 \times 10^{-9}$
r_w (fm)	$= 1.266 - 3.7A \times 10^{-4} + 2A^2 \times 10^{-6} - 4A^3 \times 10^{-9}$
r_u (fm)	$= r_v$
a_v (fm)	$= 0.66$
a_w (fm)	$= 0.48$
a_u (fm)	$= 0.66$

E = incident energy (MeV),

V = real well depth,

W = imaginary well depth (Wood-Saxon),

W_D = imaginary well depth (Wood-Saxon derivative),

U = spin-orbit potential depth,

A = mass number of the target nucleus,

r_v, r_w, r_u = radii for various potentials,

a_v, a_w, a_u = diffuseness for various potentials.

Table 2. Proton optical-model parameters^a

$V \text{ (MeV)} = 54.0 - 0.32E + \left[\frac{0.4Z}{A^{1/3}} + 24.0 \left(\frac{N - Z}{A} \right) \right]$	$r_v \text{ (fm)} = 1.17$	$a_w \text{ (fm)} = 0.75$
$W \text{ (MeV)} = 0.22E - 2.7, (W \geq 0.0)$	$r_w \text{ (fm)} = 1.32$	$a_v \text{ (fm)} = 0.51 + 0.7 \left(\frac{N - Z}{A} \right)$
$W_D \text{ (MeV)} = 11.8 - 0.25E + 12.0 \left(\frac{N - Z}{A} \right), (W_D \geq 0.0)$	$r_c \text{ (fm)} = 1.25$	

^aParameter definitions are as in Table 1; r_c is the Coulomb radius.

Table 3. Alpha Optical-Model Parameters^a

$V \text{ (MeV)} = 50.0$	$r_v \text{ (fm)} = 1.17 + \frac{1.77}{A^{1/3}}$	$a_v \text{ (fm)} = 0.576$
$W \text{ (MeV)} = 0.0$	$r_w \text{ (fm)} = r_v$	$a_w \text{ (fm)} = 0.576$
$W_D \text{ (MeV)} = 5.7 + 0.087 \times A^b$	$r_c \text{ (fm)} = 1.17$	

^aParameter definitions are as in Tables 1 and 2.

^bFitted to Huizenga and Igo's tabulated values for $A = 20 - 235$.

Table 4. Deformation parameters of ^{58}Ni Levels

Level (MeV)	J^π	β_{f}^2	Ref.
1.454	2^+	0.035	JA67, IN68, JO69a, DJ82, WI80, IN81
2.459	4^+	0.006	JA67, WI80, IN81, IN68
2.776	2^+	0.00044	WI80
3.038	2^+	0.0029	JA67, IN68, WI80
3.265	2^+	0.004	JA67, IN68, WI80, IN81
4.470	3^-	0.0196	JA67, IN68, JO69a, WI80, IN81

Table 5. Deformation parameters of ^{60}Ni Levels

Level (MeV)	J^π	β_{f}^2	Ref.
1.333	2^+	0.055	IN68, JO69a, JO65, BA74, CH83, HA83, HA81, IN81
2.159	2^+	0.0005	IN68, HA83
2.506	4^+	0.007	IN68, BA74, CH83, HA83, IN81
3.12	4^+	0.0032	IN68, HA83
4.045	3^-	0.026	IN68, JO65, BA74, JO69a, CH83, HA83, IN81

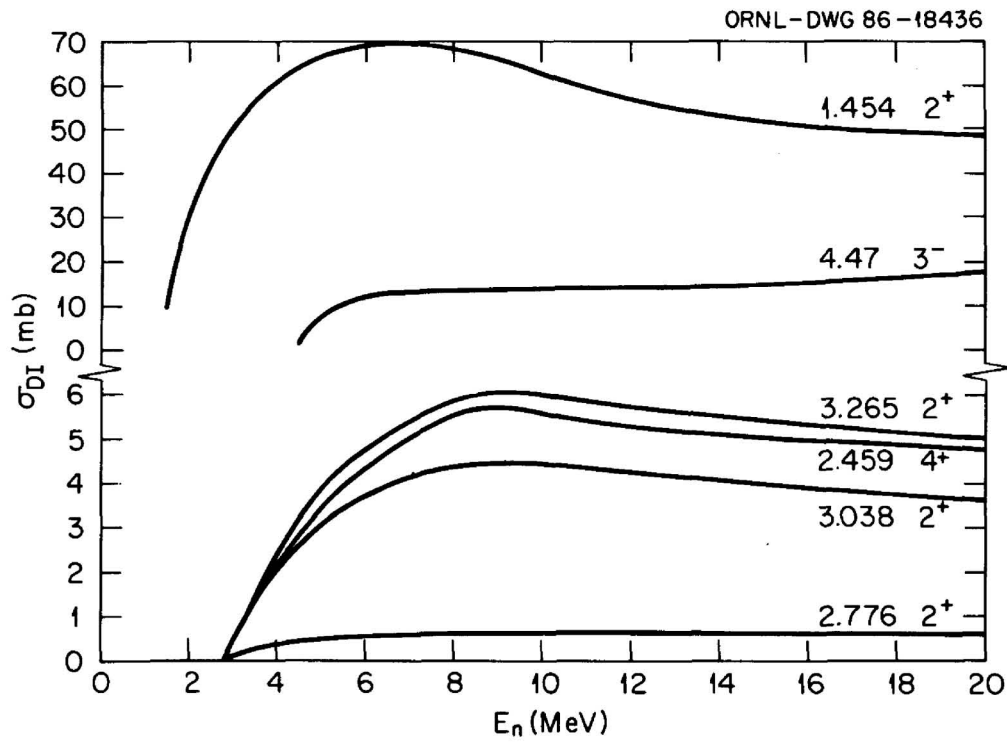


Fig. 1. Calculated direct inelastic excitation cross sections for ^{58}Ni .

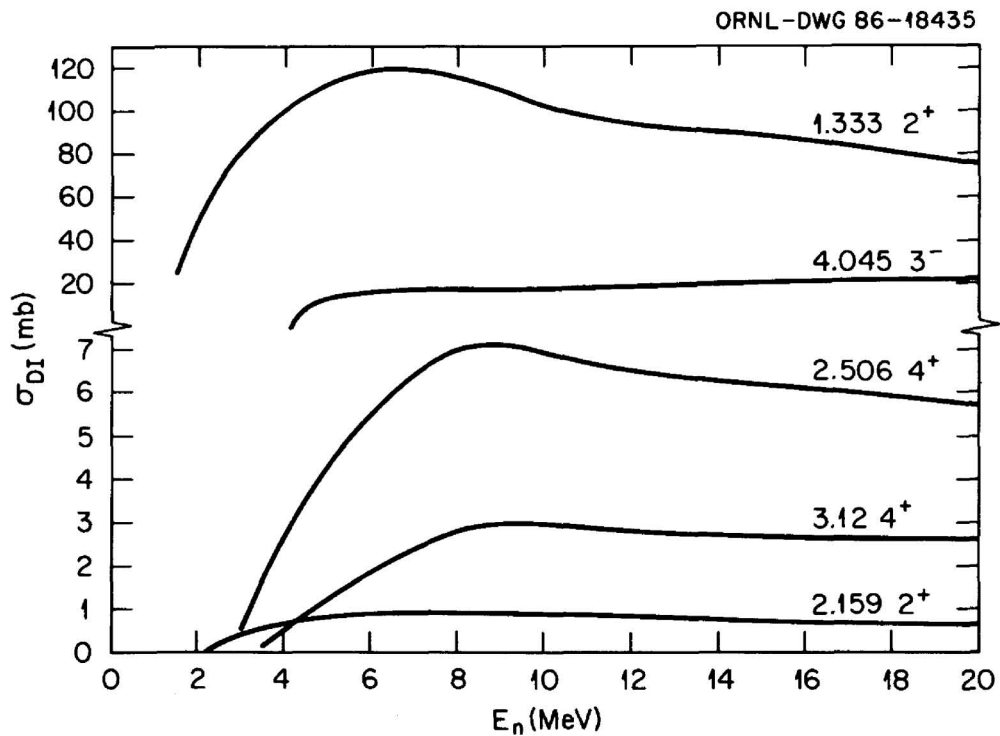


Fig. 2. Calculated direct inelastic excitation cross sections for ^{60}Ni .

As the excitation energy increases, our knowledge of these levels becomes incomplete, and eventually, as their number increases, we prefer to describe them in terms of a level density formula. In this section we give the discrete levels used in the calculations and discuss the level density formulae and parameters.

The reactions for which we need level information for the residual nuclei are: $^{58}\text{Ni}(n,n')^{58}\text{Ni}$, $^{58}\text{Ni}(n,p)^{58}\text{Co}$, $^{58}\text{Ni}(n,\alpha)^{55}\text{Fe}$, $^{58}\text{Ni}(n,np)^{57}\text{Co}$, $^{58}\text{Ni}(n,n\alpha)^{54}\text{Fe}$, $^{58}\text{Ni}(n,2n)^{57}\text{Ni}$, $^{58}\text{Ni}(n,\gamma)^{59}\text{Ni}$, $^{60}\text{Ni}(n,n')^{60}\text{Ni}$, $^{60}\text{Ni}(n,p)^{60}\text{Co}$, $^{60}\text{Ni}(n,\alpha)^{57}\text{Fe}$, $^{60}\text{Ni}(n,np)^{59}\text{Co}$, $^{60}\text{Ni}(n,n\alpha)^{56}\text{Fe}$, $^{60}\text{Ni}(n,2n)^{59}\text{Ni}$, and $^{60}\text{Ni}(n,\gamma)^{61}\text{Ni}$. The level energies, J^π values and gamma-ray branching ratios adopted for these nuclei are given in Tables 6 to 18. There are a few levels where the energies are known, but J^π values or branching ratios are experimentally undetermined. These J^π values and branching ratios were assigned as indicated by the parentheses in the tables. In most cases, these values are as given in the references (see below); others were estimated from systematics. Excited states were reported having excitation energies larger than for levels shown in Tables 6 through 18. However, the branching ratios for these higher levels were not known and thus the levels were not used in the calculations.

The information on the levels and gamma-ray branching ratios of ^{58}Ni in Table 6 was taken from the compilation of Kocher and Auble (KO76a). We include the 4.47-MeV level because it is collective and the cross section for exciting this level was computed by DWUCK (KU72) and input to TNG. Also, as seen earlier (Table 4), the β_2^2 value for this level is large, which gives rise to a significant contribution to the inelastic-scattering and gamma-ray production cross sections. Although there are many other levels in this energy region (i.e., above 3.5 MeV), the cross section for exciting these levels can be adequately accounted for in the TNG calculation (FU80) with the level density formulae.

For ^{58}Co , the level energies, the adopted J^π values, and gamma-ray branching ratios are given in Table 7. They were taken from Ref. KO76a. Table 8 shows the levels, J^π values, and branching ratios for ^{55}Fe . The levels and J^π values were taken from Ref. BR78 and the branching ratios were taken from the compilation of Kocher (KO76b). Level information from ^{57}Co , given in Table 9, was taken from Ref. BR78 and the branching ratios are from Auble (AU77a). For ^{54}Fe (see Table 10), the level energies and adopted J^π values are from Ref. BR78 and the branching ratios were compiled from the work of Verheul and Auble (VE78). The information on levels and J^π values of ^{57}Ni , given in Table 11, was taken from Ref. BR78 and the branching ratios were obtained from Ref. AU77a.

For ^{60}Ni , the level energies, their J^π values and branching ratios adopted are given in Table 12. These were taken from Ref. AU79. As explained above for ^{58}Ni , we include the 4.045-MeV level because it is collective. There are many other levels in this energy region (i.e., above 3.4 MeV), but the level density formulae (FU80) can adequately account for cross sections exciting these "other" levels.

Table 13 shows the levels, J^π values, and branching ratios for ^{60}Co . This information was taken from the compilation of Auble (AU79), with the exception of the J^π value for the 0.786-MeV level, which is from Ref. BR78. For ^{57}Fe (see Table 14), the information was obtained from Ref. BE83. Table 15 shows the levels, J^π values, and branching ratios for ^{59}Co . The branching ratios were taken from the compilation of Kim (KI76) and the level energies and J^π values were taken from Ref. BR78. For ^{56}Fe (see Table 16), the level energies and adopted J^π values were compiled from Ref. BR78. The branching ratios were taken from both Ref. BR78 and from the work of Auble (AU77a). Table 17 shows the level information for ^{59}Ni , taken from Ref. BR78. For ^{61}Ni , the level energies and J^π values were taken from the work of Ekström and Lyttkens (EK83), and are given in Table 18.

To represent the continuum excitation energy region occurring above the highest-energy discrete level (continuum cutoff E_c), the level-density formulae as described by Fu (FU76 and FU80) were used. The level-density parameters of the residual nuclei of all reactions analyzed are given in Table 19. The formulae of Gilbert and Cameron (GI65) were used in computing most of the parameters. However, it

Table 6. Energy levels and gamma-ray branching ratios of ^{58}Ni

Initial state			Branching ratios to state N						
N	J^π	E (keV)	1	2	3	4	5	7	
1	0^+	0							
2	2^+	1454	100						
3	4^+	2459		100					
4	2^+	2776	4	96					
5	1^+	2903	6	94					
6	0^+	2943		11		11	78		
7	2^+	3038	42	57		1			
8	2^+	3265	63	37					
9	$3^{(+)}$	3421			95			5	
10	3^-	4470		100					

Table 7. Energy levels and gamma-ray branching ratios of ^{58}Co

Initial state			Branching ratios to state N						
N	J^π	E (keV)	1	2	3	4	5	6	7
1	2^+	0							
2	5^+	25	100						
3	4^+	53	71	29					
4	3^+	111	53		47				
5	3^+	366	99			1			
6	5^+	374		4	96				
7	4^+	458		83	1	15	1		
8	$(4)^+$	886		8	6	51	20	15	
9	$(3)^+$	1040	29				24		47

Table 8. Energy levels and gamma-ray branching ratios of ^{55}Fe

N	Initial state		Branching ratios to state N									
	J^π	E (keV)	1	2	3	4	5	6	9	13	15	
1	$3/2^-$	0										
2	$1/2^-$	412	100									
3	$5/2^-$	931	98	2								
4	$7/2^-$	1317	96		4							
5	$7/2^-$	1409	46		54							
6	$1/2^-$	1919	68	32								
7	$3/2^-$	2052	23	77								
8	$5/2^-$	2144	18	3	43	36						
9	$9/2^-$	2212				2	98					
10	$5/2^-$	2256					100					
11	$9/2^-$	2300			92	8						
12	$3/2^-$	2470	100									
13	$11/2^-$	2539				100						
14	$5/2^-$	2578	84	7	6	3						
15	$13/2^{(-)}$	2813									100	
16	$(5/2^-)$	2871	88		12							
17	$(7/2^-)$	2938	55			45						
18	$11/2^{(-)}$	2983							100			
19	$(9/2^-)$	2984					100					
20	$3/2^-$	3027	65	35								
21	$(11/2^-)$	3072								83	17	

Table 9. Energy levels and gamma-ray branching ratios of ^{57}Co

N	Initial state		Branching ratios to state N						
	J^π	E (keV)	1	2	3	4	5	7	
1	$7/2^-$	0							
2	$9/2^-$	1224	100						
3	$3/2^-$	1378	100						
4	$(1/2^-)$	1505			100				
5	$11/2^-$	1689	46	54					
6	$3/2^-$	1757	100						
7	$7/2^-$	1897	41	59					
8	$5/2^-$	1920	100						
9	$5/2^-$	2133	83		14	3			
10	$7/2^-$	2311	10	70	20				
11	$(11/2^-)$	2486	65	12			12	11	
12	$(13/2^-)$	2524					100		
13	$(11/2^-)$	2560	42	42			16		
14	$7/2^-$	2611	100						

Table 10. Energy levels and gamma-ray branching ratios of ^{54}Fe

Initial state			Branching ratios to state N				
N	J^π	E (keV)	1	2	3	8	9
1	0^+	0000					
2	2^+	1408	100				
3	4^+	2538		100			
4	0^+	2561		100			
5	6^+	2950			100		
6	2^+	2959	55	45			
7	2^+	3166	81	19			
8	4^+	3295		16	84		
9	$3(+)$	3345		57	43		
10	4^+	3834		91	9		
11	(5^+)	4029			5	95	
12	4^+	4048		50			50
13	$3(+)$	4074		92	8		
14	4^+	4265		21	79		
15	0^+	4292		100			
16	2^+	4579	30	70			

Table 11. Energy levels and gamma-ray branching ratios of ^{57}Ni

Initial state			Branching ratios to state N	
N	J^π	E (keV)	1	2
1	$3/2^-$	0		
2	$5/2^-$	769	100	
3	$1/2^-$	1113	100	
4	$5/2(-)$	2443	100	
5	$7/2^-$	2577	100	
6	$(3/2^-)$	3007	100	
7	$7/2^-$	3230	40	60
8	$(7/2)^-$	3370		100

Table 12. Energy levels and gamma-ray branching ratios of ^{60}Ni

Initial state			Branching ratios to state N				
N	J^π	E (keV)	1	2	3	5	6
1	0^+	0					
2	2^+	1333	100				
3	2^+	2159	15	85			
4	0^+	2285		100			
5	4^+	2506		100			
6	3^+	2626		30	70		
7	4^+	3120		100			
8	2^+	3124	10	90			
9	$(3)^+$	3186		24	46	30	
10	1^+	3194	15	50	35		
11	2^+	3270	15	45	20		20
12	(0^+)	3318		100			
13	3^-	4045		69	31		

Table 13. Energy levels and gamma-ray branching ratios of ^{60}Co

Initial state			Branching ratios to state N									
N	J^π	E (keV)	1	2	3	4	5	6	7	8	10	
1	5^+	0										
2	2^+	59	100									
3	4^+	277	100									
4	3^+	288	100									
5	5^+	436	46		54							
6	3^+	506	100									
7	$(2)^+$	543		43	57							
8	3^+	614		97	3							
9	1^+	739		60					40			
10	4^+	786	52			42	3	2		1		
11	(3^+)	1004	8	48	24				19		1	
12	4^+	1006			26					71	3	

Table 14. Energy levels and gamma-ray branching ratios of ^{57}Fe

Initial state			Branching ratios to state N				
N	J^π	E (keV)	1	2	3	4	5
1	$1/2^-$	0					
2	$3/2^-$	14	100				
3	$5/2^-$	136	11	89			
4	$3/2^-$	367	14	79	7		
5	$5/2^-$	706	5	85	9	1	
6	$7/2^-$	1007		32	68		
7	$9/2^-$	1198	100				
8	$1/2^-$	1265	3	4		93	
9	$7/2^-$	1357		22		23	55
10	$3/2^-$	1627	5	61		26	8
11	$3/2^-$	1725	67	2		9	22

Table 15. Energy levels and gamma-ray branching ratios of ^{59}Co

Initial state			Branching ratios to state N				
N	J^π	E (keV)	1	2	3	4	6
1	$7/2^-$	0					
2	$3/2^-$	1099	100				
3	$9/2^-$	1190	100				
4	$3/2^-$	1291	100				
5	$1/2^-$	1435		50		50	
6	$11/2^-$	1459	100				
7	$5/2^-$	1482	90	10			
8	$7/2^-$	1745	60		40		
9	$7/2^-$	2063			60		40
10	$(5/2^-)$	2088	100				

Table 16. Energy levels and gamma-ray branching ratios of ^{56}Fe

Initial state			Branching ratios to state N								
N	J^π	E (keV)	1	2	3	4	5	6	8	10	11
1	0^+	0									
2	2^+	847	100								
3	4^+	2085		100							
4	2^+	2658	2	98							
5	0^+	2942		100							
6	2^+	2960	2	98							
7	(1^+)	3120		100							
8	4^+	3123			100						
9	2^+	3370	15	85							
10	6^+	3388			100						
11	3^+	3445		78	21	1					
12	1^+	3449	50	50							
13	2^+	3602	65	35							
14	0^+	3607		100							
15	6^+	3756			82					18	
16	2^+	3832	11	63		26					
17	3^+	3857		6	92				2		
18	$(3)^+$	4049		80	19			1			
19	(3^+)	4100		60	25	2		1	12		
20	(4^+)	4120		18	79	1		1	1		
21	4^+	4298		25	10	1			64		
22	(0^+)	4302		100							
23	3^+	4395		90					10		
24	$(2)^+$	4401		78			6				16
25	(4^+)	4458		3	38				59		
26	3^-	4510		31	16	50					3

Table 17. Energy levels and gamma-ray branching ratios of ^{59}Ni

N	Initial state		Branching ratios to state N				
	J^π	E (keV)	1	2	3	4	5
1	$3/2^-$						
2	$5/2^-$	339	100				
3	$1/2^-$	465	100				
4	$3/2^-$	878	99	1			
5	$5/2^-$	1190	92	8			
6	$1/2^-$	1302	75	1	11	13	
7	$7/2^-$	1338		100			
8	$5/2^-$	1680	14	84	2		
9	$(3/2^-)$	1735	61	17	11		11
10	$(9/2^-)$	1739		100			

Table 18. Energy levels of ^{61}Ni

Initial state			Initial state		
N	J^π	E (keV)	N	J^π	E (keV)
1	$3/2^-$	0	12	$3/2^-$	1729
2	$5/2^-$	67	13	$9/2^-$	1808
3	$1/2^-$	283	14	$9/2^-$	1988
4	$1/2^-$	656	15	$5/2^-$	1998
5	$5/2^-$	909	16	$7/2^-$	2018
6	$7/2^-$	1015	17	$9/2^+$	2122
7	$3/2^-$	1100	18	$1/2^-$	2123
8	$5/2^-$	1132	19	$11/2^-$	2129
9	$3/2^-$	1185	20	$(3/2^-)$	2410
10	$7/2^-$	1455	21	$7/2^-$	2464
11	$5/2^-$	1610			

Table 19. Level density parameters

Residual Nuclei	T (MeV)	E_o (MeV)	a (MeV ⁻¹)	Δ (MeV)	σ	E_c (MeV)	E_x (MeV)
⁵⁸ Ni	1.607	-0.0972	5.438	2.47	11.896	3.52	11.01
⁵⁸ Co	1.303	-1.89	7.062	0.507	14.259	1.044	6.58
⁵⁵ Fe	1.576	-1.758	5.909	1.54	12.476	3.076	10.88
⁵⁷ Co	1.485	-1.249	5.951	1.27	12.868	2.723	9.326
⁵⁴ Fe	1.576	0.2635	5.568	2.84	11.615	4.656	11.14
⁵⁷ Ni	1.439	0.6294	4.999	1.20	10.811	3.71	6.332
⁵⁹ Ni	1.541	-1.877	6.003	1.20	13.283	1.746	10.24
⁶⁰ Ni	1.395	-0.1853	6.539	2.49	14.632	3.339	10.49
⁶⁰ Co	1.204	-2.252	8.13	0.49	16.898	0.79	6.864
⁵⁷ Fe	1.358	-1.341	6.923	1.54	14.97	1.975	9.719
⁵⁹ Co	1.249	-0.7826	7.058	1.29	15.617	2.154	8.031
⁵⁶ Fe	1.474	-0.2907	6.355	2.81	13.581	4.539	11.64
⁶¹ Ni	1.331	-1.556	7.029	1.20	15.902	2.526	9.152

T = nuclear temperature

E_o = parameter for matching lower energy level density to the higher one

$a = \pi^2 g/6$ (g = density of uniformly spaced single particle states)

Δ = pairing energy correction

σ^2 = spin cut-off parameter = $2c \sqrt{(E - \Delta)/a}$ where E is the excitation energy,

E_c = continuum cutoff

E_x = tangency point

was found that for computing the spin-cutoff parameter " σ^2 " a formula due to Facchini and Saetta-Menichella (FA68) produced better results and was used for excitation energies greater than the tangency point (E_x). The spin cutoff parameter at E_c was based on the cumulative sum of the discrete values. In between E_x and E_c , the spin cutoff parameter was assumed to vary linearly with the excitation energy.

2.5 GIANT DIPOLE RESONANCE PARAMETERS

The giant dipole resonance parameters used as input to TNG in this analysis are those reported by Fuller et al. (FU73). For ⁵⁸Ni the resonance has a peak cross section of 125 mb, the width of the resonance is 4.8 MeV, and the energy of the resonance peak is 19.5 MeV. The resonance for ⁶⁰Ni has a peak cross section of 90 mb, width of 5.5 MeV, and energy of the resonance peak of 19 MeV.

2.6 (n,t), ($n,^3\text{He}$), and (n,d) CROSS SECTIONS

The only measured data points found for the (n,t) reaction were less than 0.1 mb and were in the energy range from 14.4 to 14.7 MeV (BI75, QA76a, SU79). Since this cross section is very small, the (n,t) reaction was ignored in the TNG calculations. No measured data were found for the ($n,^3\text{He}$)

reaction and this reaction was also ignored. The (n,t) and $(n,^3\text{He})$ reactions were not included in ENDF/B-V. For (n,d) , the cross sections reported by Grimes et al. (GR79) and Glover and Purser (GL61) at 14.8 MeV agree reasonable well with the ENDF/B-V values. Therefore, the ENDF/B-V cross sections for (n,d) were used in this analysis. These cross sections were not computed by the TNG code but were input to it as correction factors to reduce proportionately the other TNG calculated cross sections.

3. COMPUTATIONAL METHODS AND PROCEDURES

Nuclear model calculations play an important role in modern evaluations for the interpolation and extrapolation of cross sections to energy regions where no data exist, and for predictions of reaction cross sections for which there are few or no experimental data. However, in order to ensure internal consistency, the model calculations should simultaneously reproduce as much of the experimental information as possible for as many reaction channels as reliable data are available. As noted earlier, the model code TNG (FU80, FU80a, SH86) was used exclusively for this analysis. The applicability of TNG to cross-section evaluations has been extended as TNG is now capable of using variable energy bin widths for outgoing particle energies (SH86).

Calculations for both ^{58}Ni and ^{60}Ni at a number of incident energies from 1.0 to 20.0 MeV were performed. Parameters required as input to TNG are now summarized. The discrete energy levels for each of the residual nuclei and the gamma-ray branching ratios (Tables 6 through 18), the level density parameters (Table 19), the direct inelastic cross sections calculated by DWUCK (KU72) as discussed in Section 2, the optical-model parameters (Tables 1 through 3), the giant dipole resonance parameters, and the (n,d) cross section were all used as input to the TNG computer code. Parameters required for the precompound mode of reaction were the same as determined previously in a global analysis (FU80) and were found to be satisfactory for the present calculations.

TNG simultaneously computes cross sections for all energetically possible binary reactions and tertiary reactions, and also computes the resulting gamma-ray production cross sections. Also, TNG computes the compound and precompound cross sections in a consistent fashion and conserves angular momentum in both compound and precompound reactions. Thus, the resulting cross-section sets are consistent and energy balance is ensured. The results from TNG are found to agree reasonably well with available data, and these comparisons are discussed in the next section.

4. COMPARISON OF CALCULATIONS WITH EXPERIMENTS

In this section the TNG calculated cross sections are compared with available data obtained from the National Nuclear Data Center CSISRS file (CS86). When the comparisons were made for natural nickel, the cross sections for ^{58}Ni were multiplied by 0.71 and for ^{60}Ni were multiplied by 0.29 and summed to obtain the results. Together, $^{58,60}\text{Ni}$ account for 94.4% of natural nickel. Calculations for the minor isotopes $^{61,62,64}\text{Ni}$ were not performed.

4.1 TOTAL CROSS SECTION

The TNG computed total cross section is compared to the measured data of Larson (LA80) in Fig. 3. The calculation is too large in the energy range less than 5.0 MeV. As noted earlier, the total cross section σ_t is the sum of the elastic and nonelastic cross section. The nonelastic cross section is the

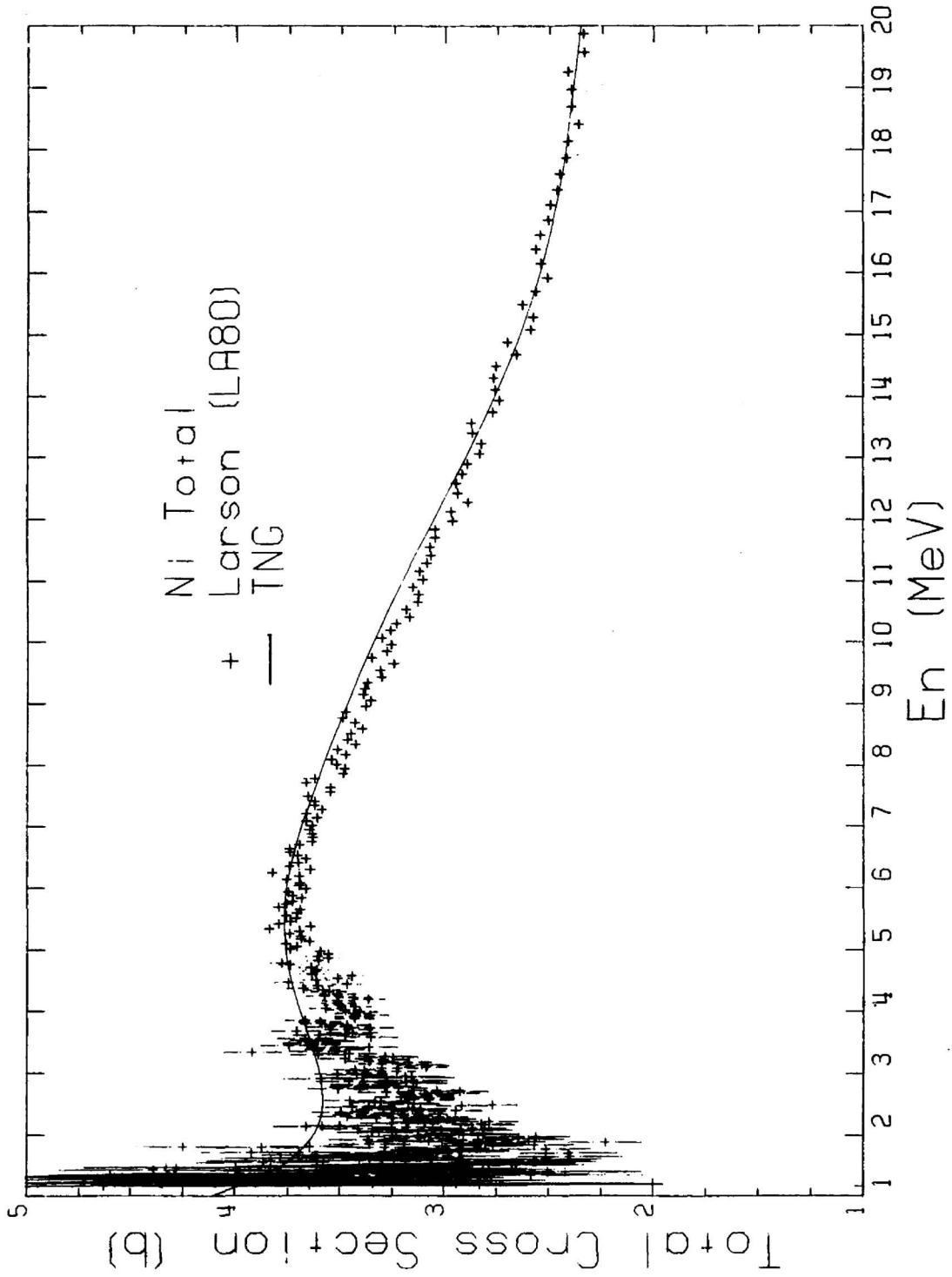


Fig. 3. Comparison of calculated and experimental total cross sections for nickel.

sum of all the individual reaction cross sections, which we work hard to reproduce with TNG. For the evaluation (of which these calculations will become a part) the elastic cross section will be obtained by subtracting the nonelastic cross section from the total cross section, and the calculated elastic and total cross sections are not used. Thus it is important to use optical model parameters which reproduce the nonelastic cross section; it is less important how well the elastic and total cross sections are reproduced, as long as the elastic angular distributions are described reasonably well by the optical model parameters chosen.

4.2 NONELASTIC CROSS SECTION

Comparison of the nonelastic cross section with experiment is shown in Fig. 4. The measured elastic cross sections from Bauer et al. (BA63), Hansen et al. (HA73), and Kinney and Perey (KI74) were subtracted from the total cross section of Larson (LA80) and included in this figure in order to further check the calculation. The good agreement lends support to the optical-model parameters used for the $n + {}^{58,60}\text{Ni}$ channel.

4.3 ELASTIC CROSS SECTION

Measured data for the elastic cross section of ${}^{58}\text{Ni}$, ${}^{60}\text{Ni}$, and natural Ni are compared with the TNG calculations in Figs. 5 through 7. The differences seen between the calculated elastic cross sections for ${}^{58}\text{Ni}$ and ${}^{60}\text{Ni}$ are due mainly to the contributions from the compound elastic cross sections, as the shape elastic cross sections are very similar. As for the total cross sections, the elastic cross-section calculation is too large at incident energies less than 5.5 MeV. As noted earlier, the elastic cross section is the difference between the total and nonelastic cross section and measured data are used for the total cross section in ENDF. The elastic angular distributions in ENDF/B-V for nickel are in good agreement with experimental data (DI79, BH74) and thus emphasis was placed on fitting the measured nonelastic cross section in this analysis.

4.4 TOTAL INELASTIC SCATTERING CROSS SECTION

The TNG calculations of cross sections for total inelastic-scattering of neutrons from ${}^{58}\text{Ni}$, ${}^{60}\text{Ni}$, and natural nickel are compared to experimental data in Figs. 8 through 10. The computed cross sections agree well with the measurements with the exception of the data from Fujita et al. (FU72) and Salnikov et al. (SA70) at 14.0 MeV (See Fig. 10). In these experiments, the outgoing neutrons were detected with a time-of-flight arrangement to perform the analysis. The total inelastic scattering cross section was deduced after allowing for contributions from (n ,particle) reactions. Apparently, the (n ,particle) reaction cross sections were underestimated in obtaining the unreasonably large total inelastic cross sections shown in Fig. 10. Also shown are the data of Larson et al. (LA85) which were obtained from measurement of the ${}^{58,60}\text{Ni } 2_1^+ \rightarrow 0_{g.s.}^+$ gamma rays corrected for the cross sections for gamma rays which bypass the 2_1^+ state and go directly to the ground state.

4.5 ANGULAR DISTRIBUTIONS FOR INELASTIC SCATTERING

The calculated differential ${}^{58,60}\text{Ni } (n,n')$ cross sections for exciting the low-lying discrete levels are compared with measurements in Figs. 11 through 43. The DWBA calculations for inelastic scattering were combined with the TNG computations to obtain the results in these figures. Measurements of angular distributions for both individual levels and groups of levels are presented. The TNG and DWUCK calculations were summed for the groups of levels for the comparisons. The need for nuclear model analyses (and preferably better data) can be seen from these figures for in many cases the measurements disagree.

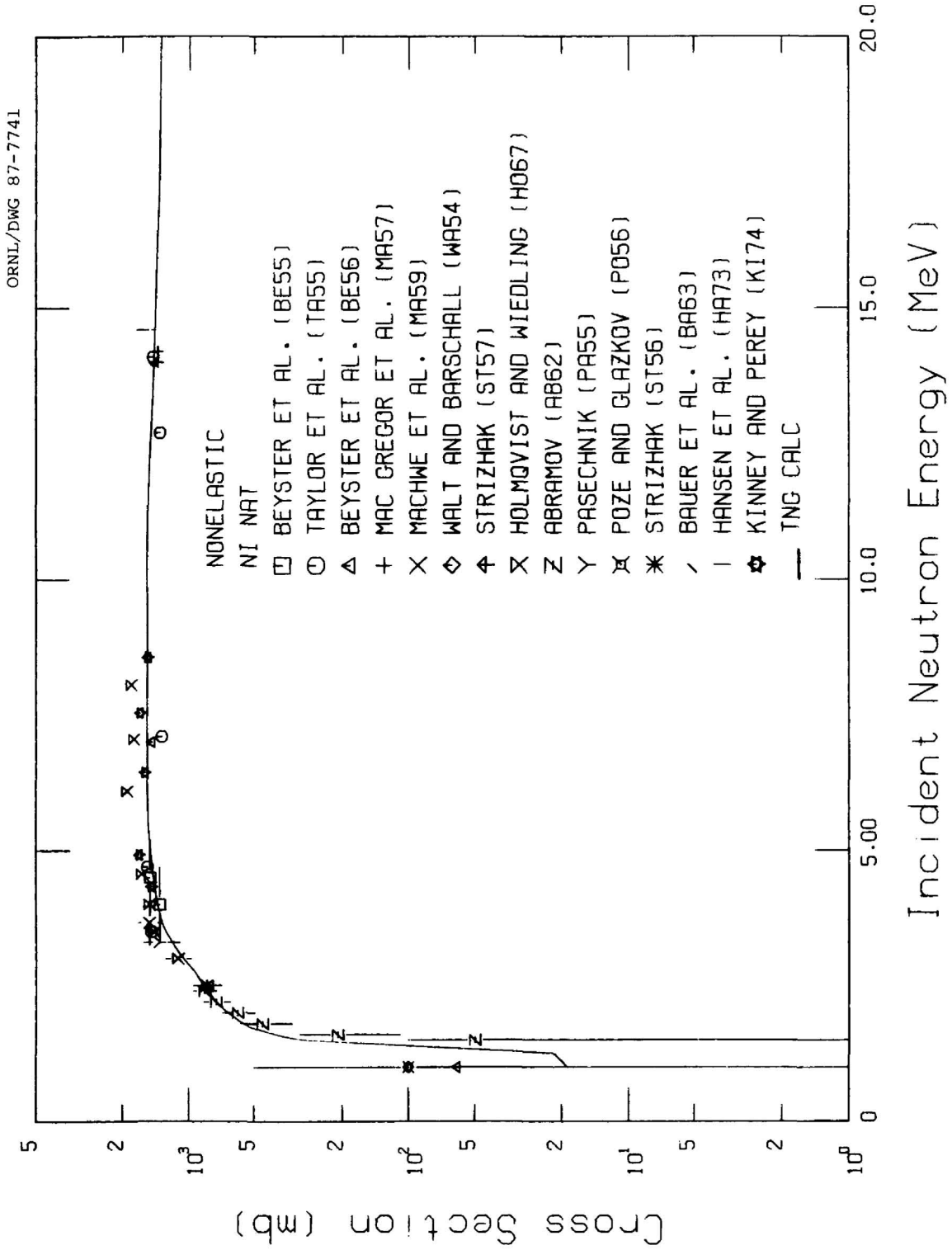


Fig. 4. Comparison of calculated and experimental nonelastic cross sections for nickel.

ORNL/DWG 87-7742

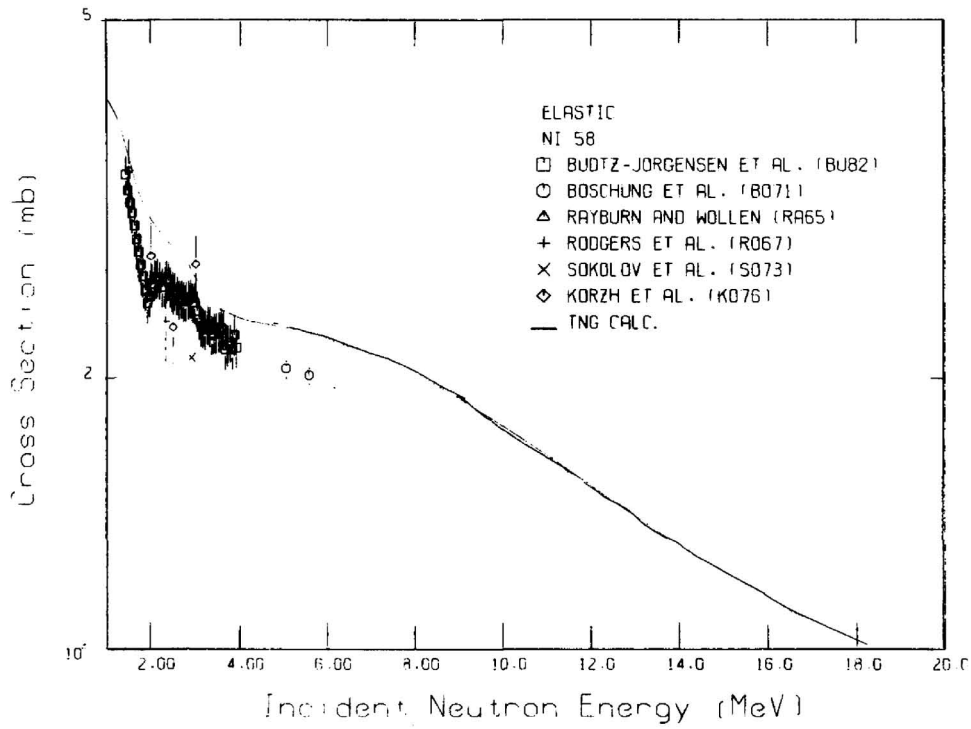


Fig. 5. Comparison of calculated and experimental elastic cross sections for ^{58}Ni .

ORNL/DWG 87-7743

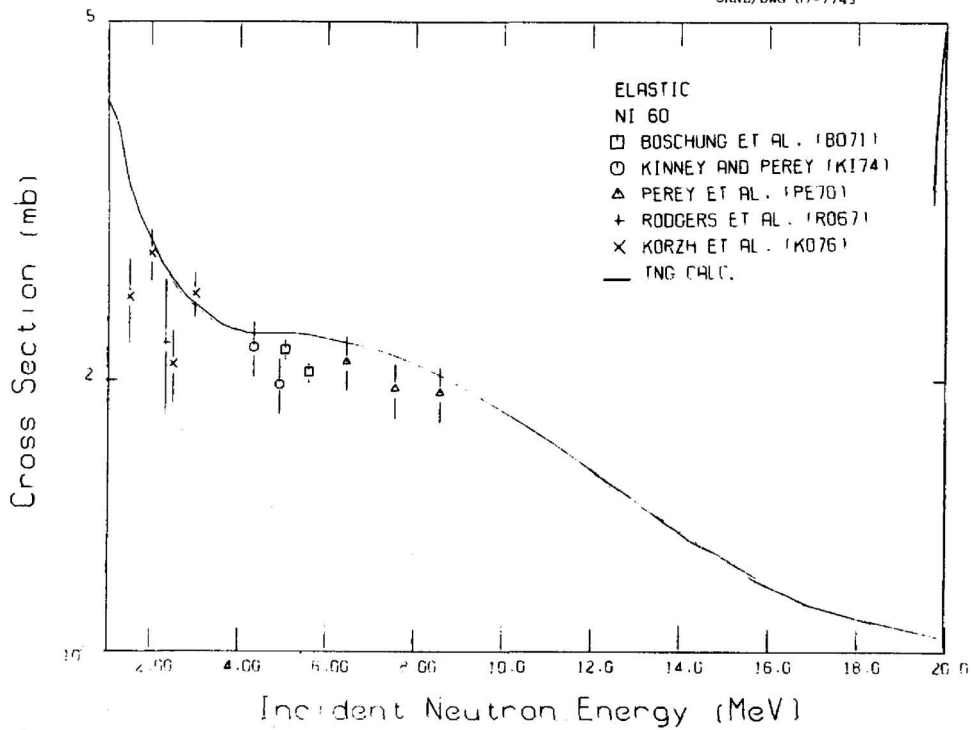


Fig. 6. Comparison of calculated and experimental elastic cross sections for ^{60}Ni .

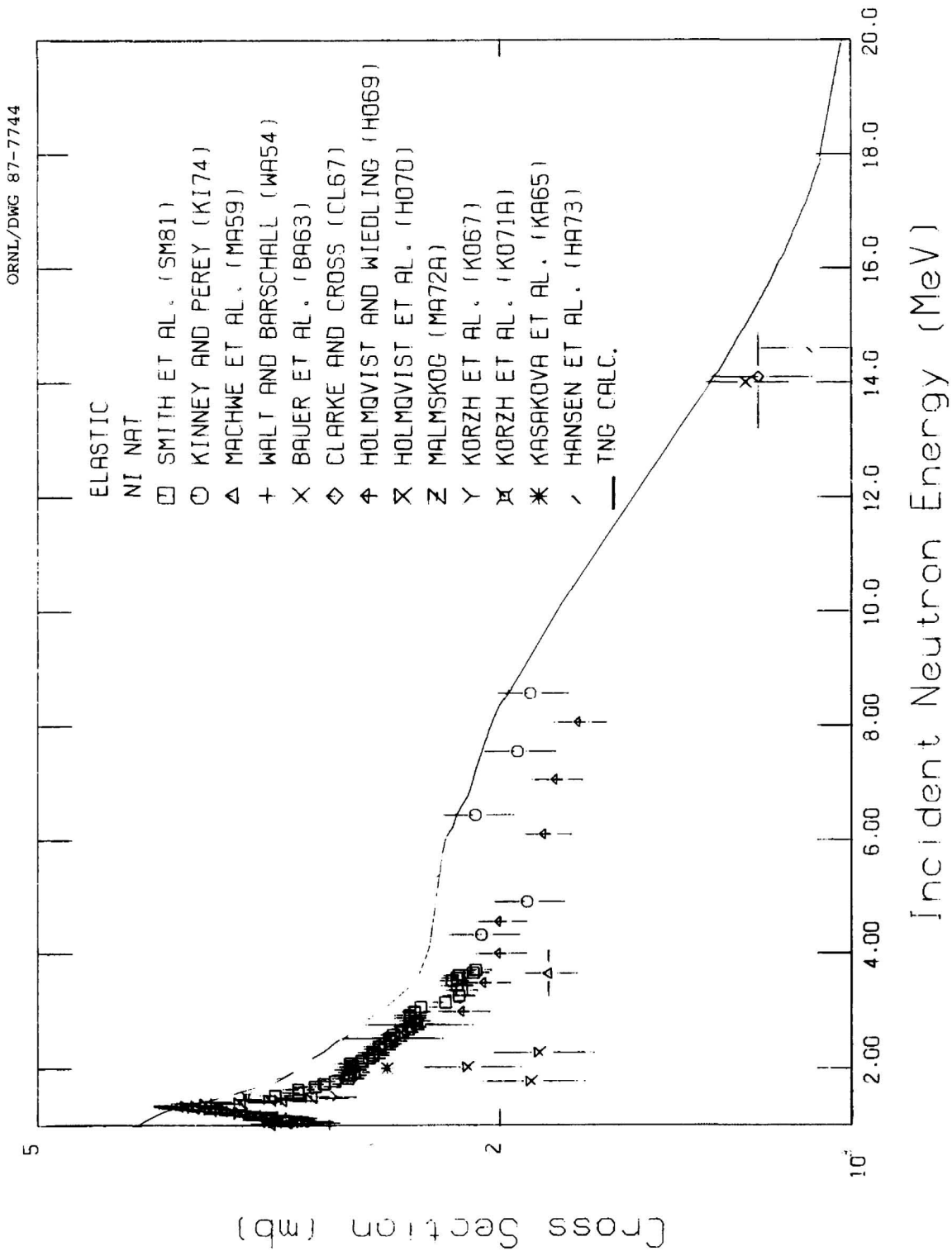


Fig. 7. Comparison of calculated and experimental elastic cross sections for ⁶⁰Ni.

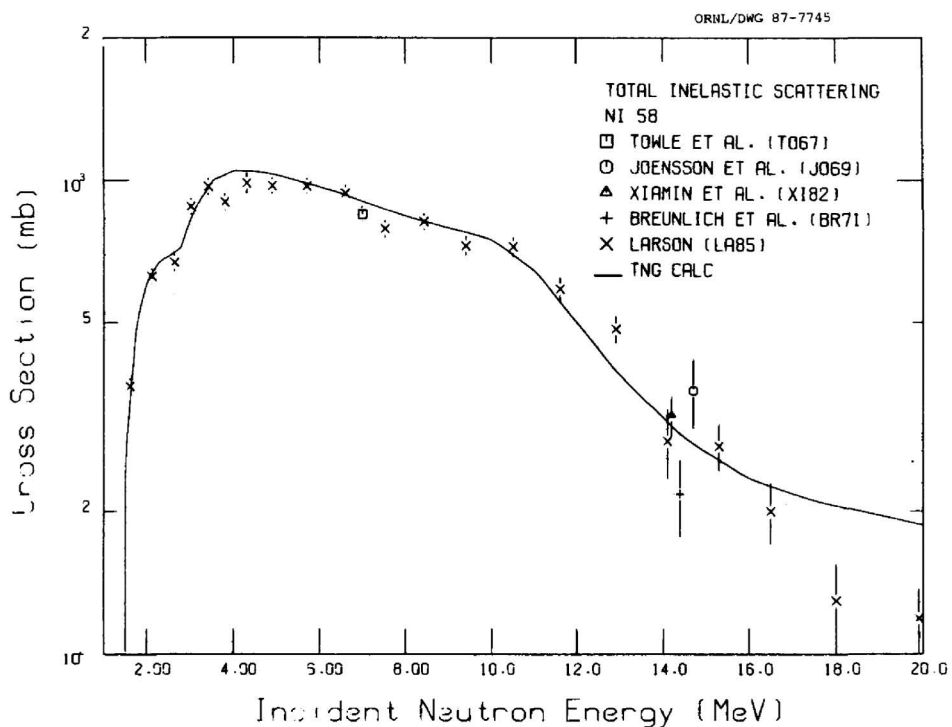


Fig. 8. Comparison of calculated and experimental total inelastic scattering cross sections for ^{58}Ni .

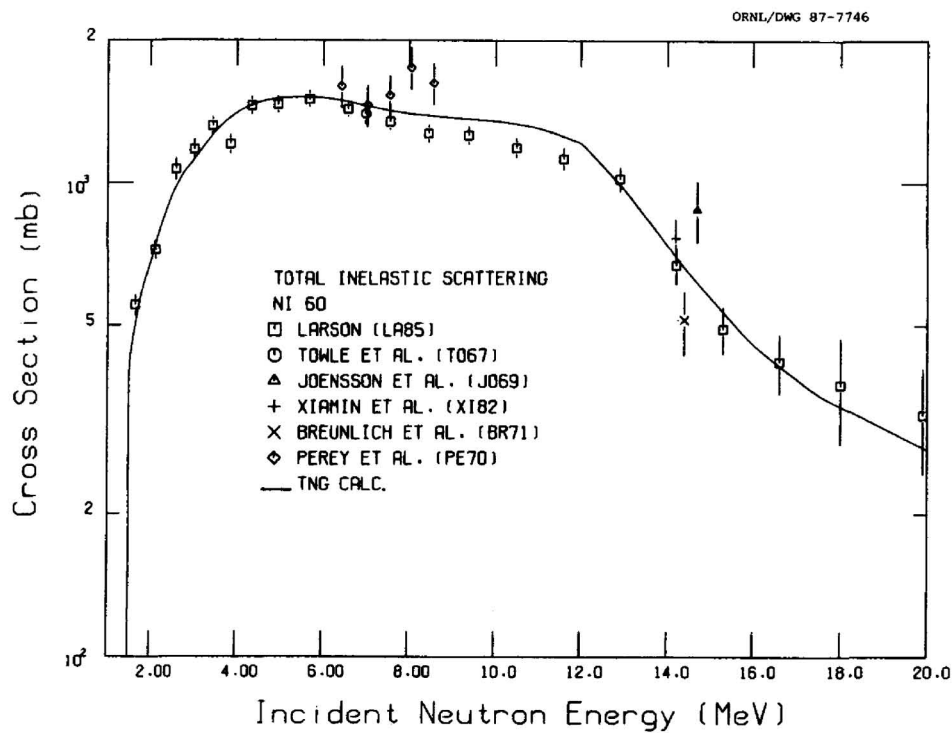


Fig. 9. Comparison of calculated and experimental total inelastic scattering cross sections for ^{60}Ni .

ORNL/DWG 87-7747

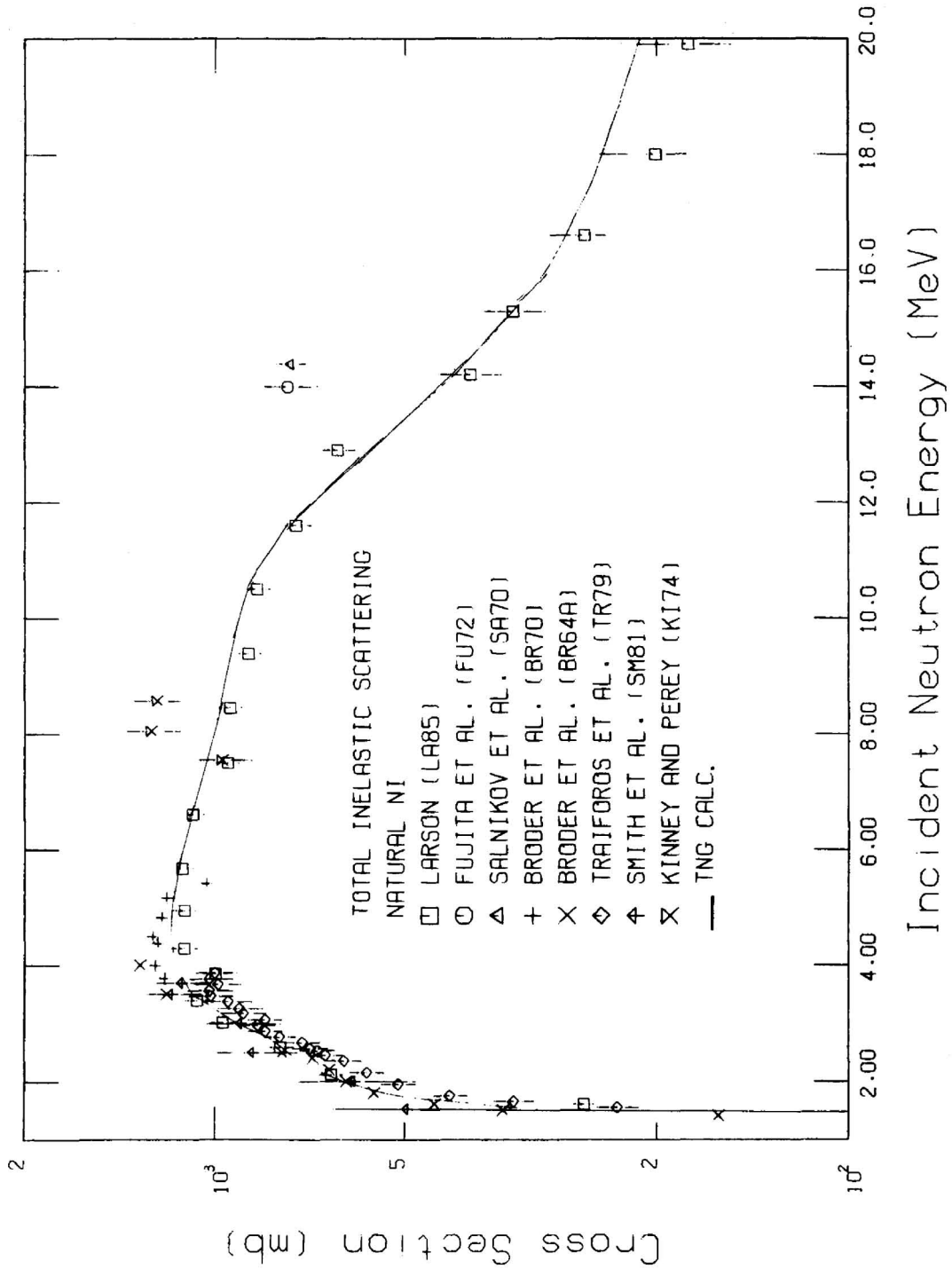


Fig. 10. Comparison of calculated and experimental total inelastic scattering cross sections for ⁵⁸Ni.

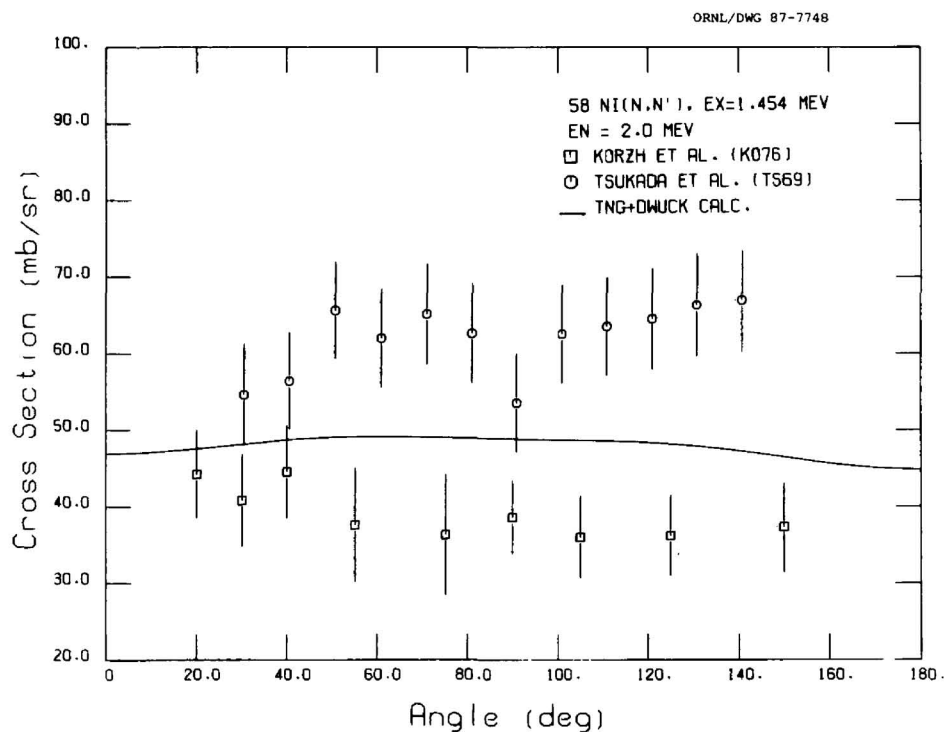


Fig. 11. Comparison of calculated and experimental differential cross sections for exciting the 1.454-MeV level at $E_n = 2.0$ MeV.

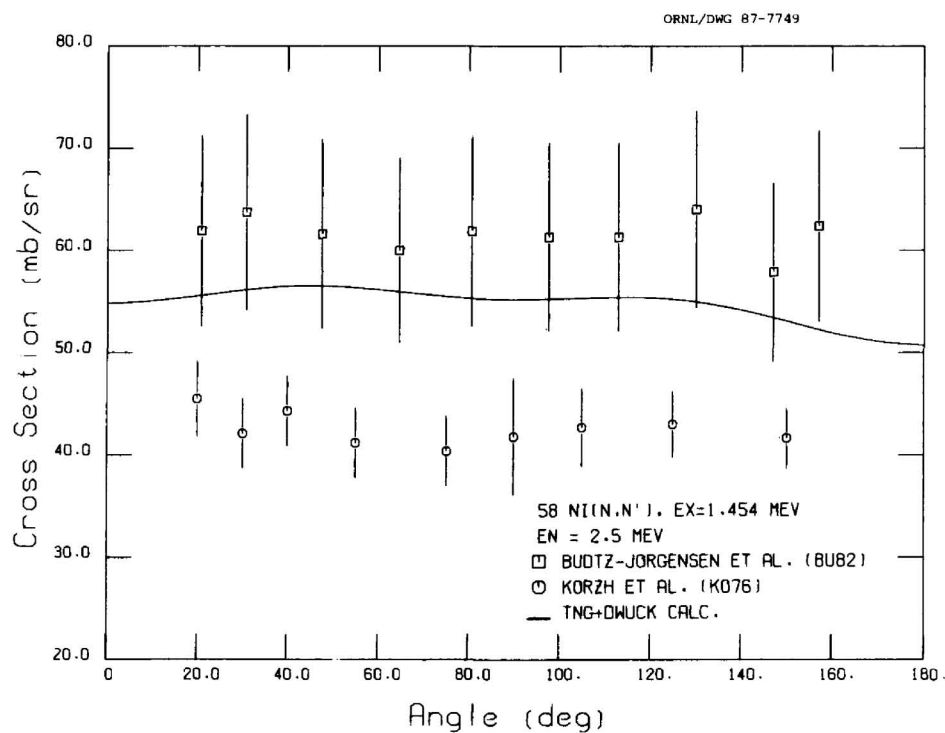


Fig. 12. Comparison of calculated and experimental differential cross sections for exciting the 1.454-MeV level at $E_n = 2.5$ MeV.

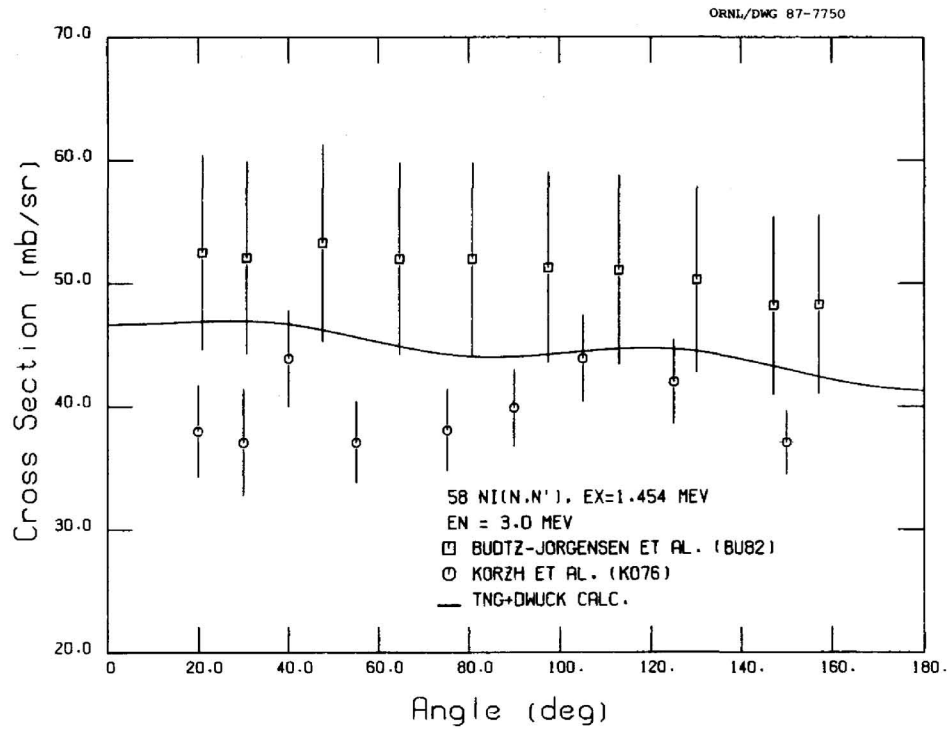


Fig. 13. Comparison of calculated and experimental differential cross sections for exciting the 1.454-MeV level at $E_n = 3.0$ MeV.

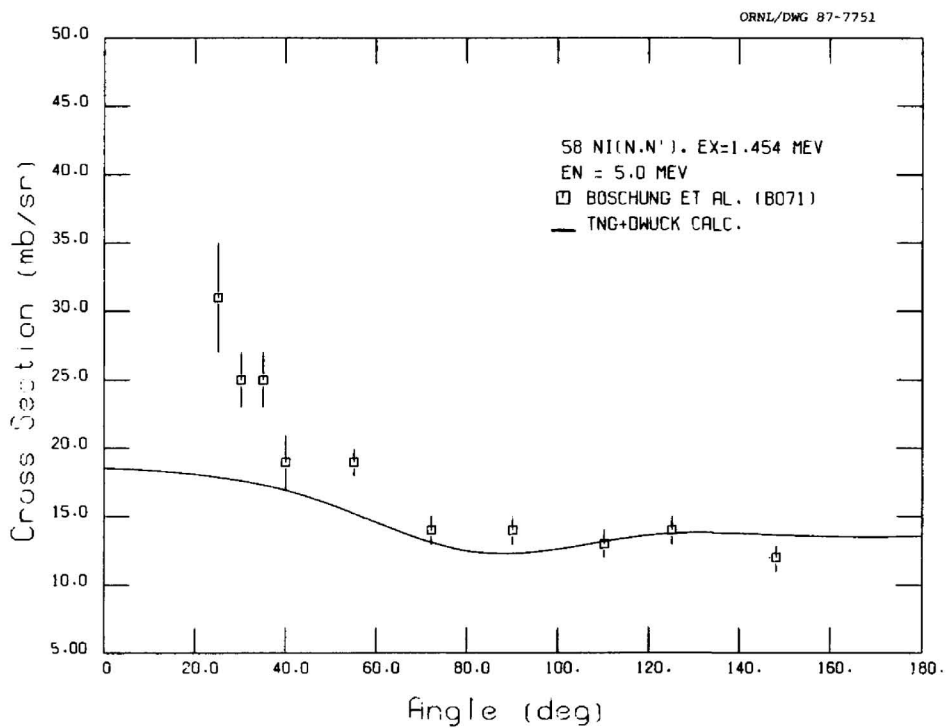


Fig. 14. Comparison of calculated and experimental differential cross sections for exciting the 1.454-MeV level at $E_n = 5.0$ MeV.

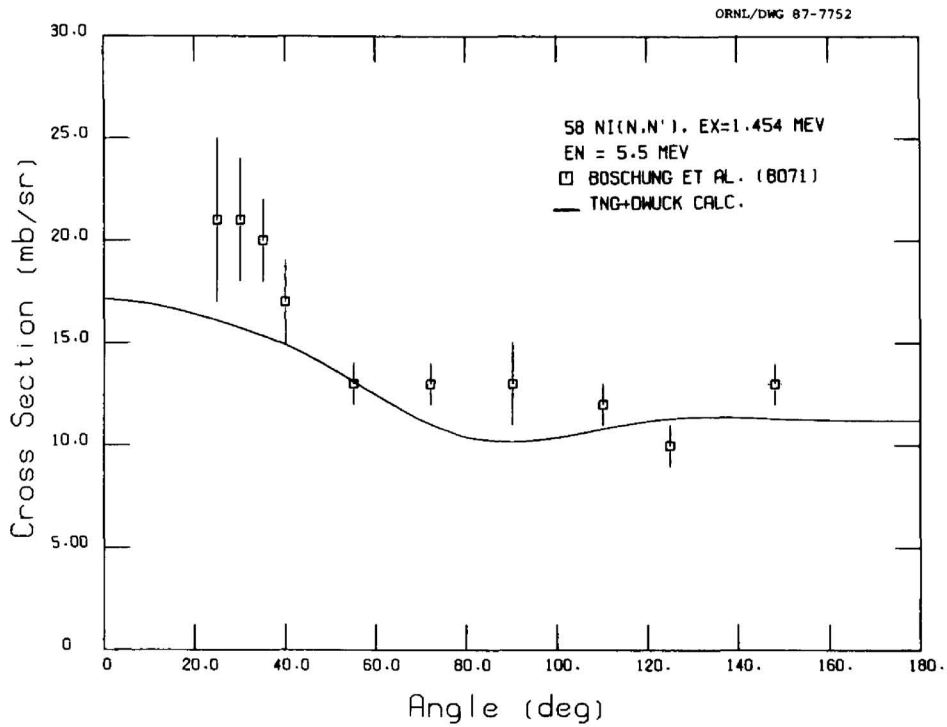


Fig. 15. Comparison of calculated and experimental differential cross sections for exciting the 1.454-MeV level at $E_n = 5.5$ MeV.

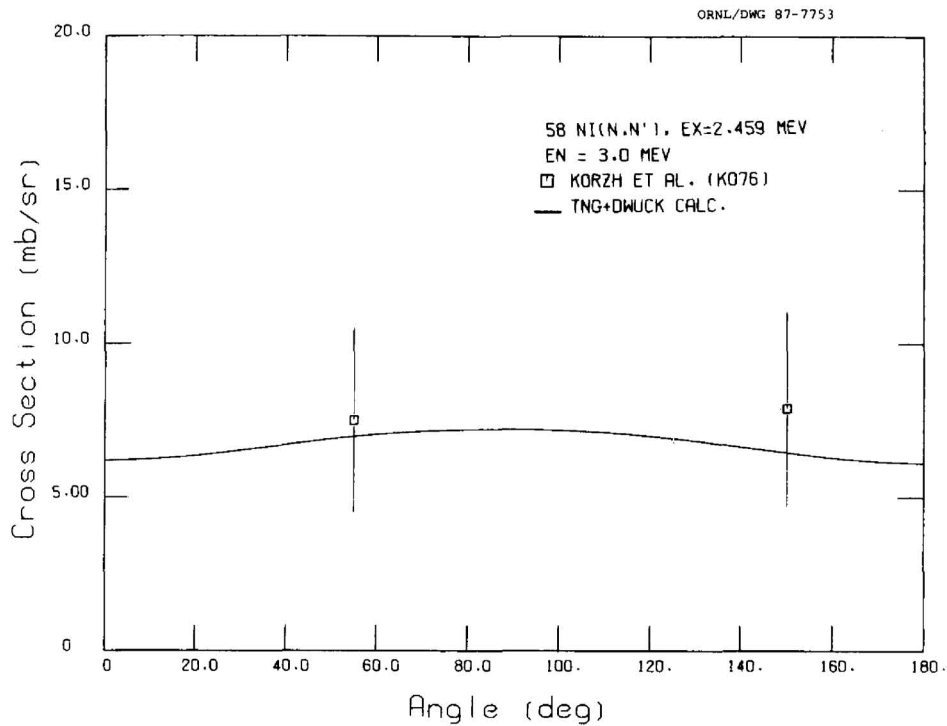


Fig. 16. Comparison of calculated and experimental differential cross sections for exciting the 2.459-MeV level at $E_n = 3.0$ MeV.

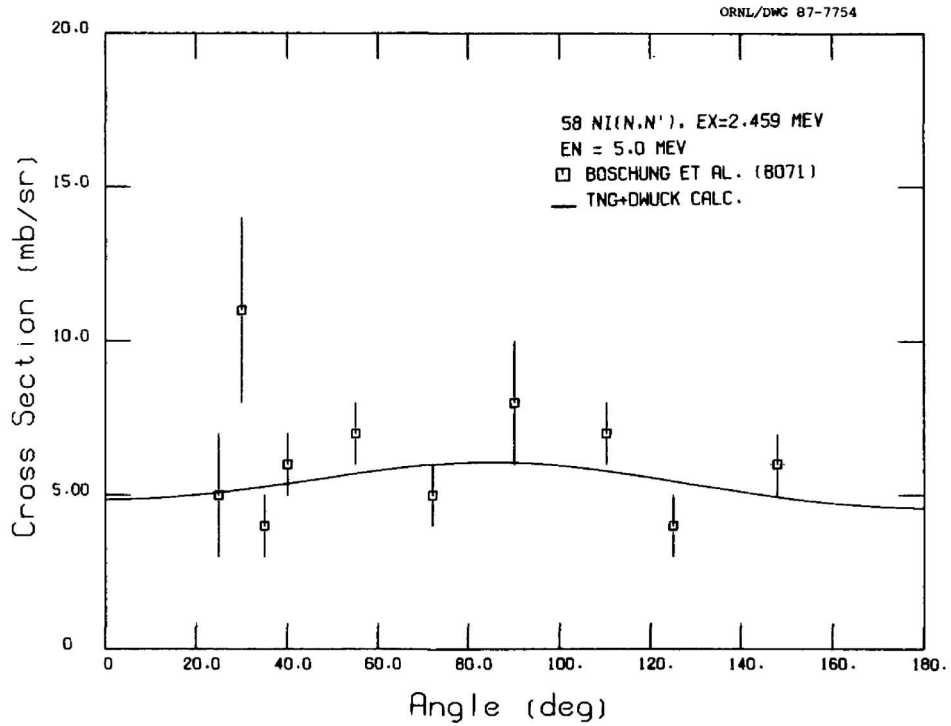


Fig. 17. Comparison of calculated and experimental differential cross sections for exciting the 2.459-MeV level at $E_n = 5.0$ MeV.

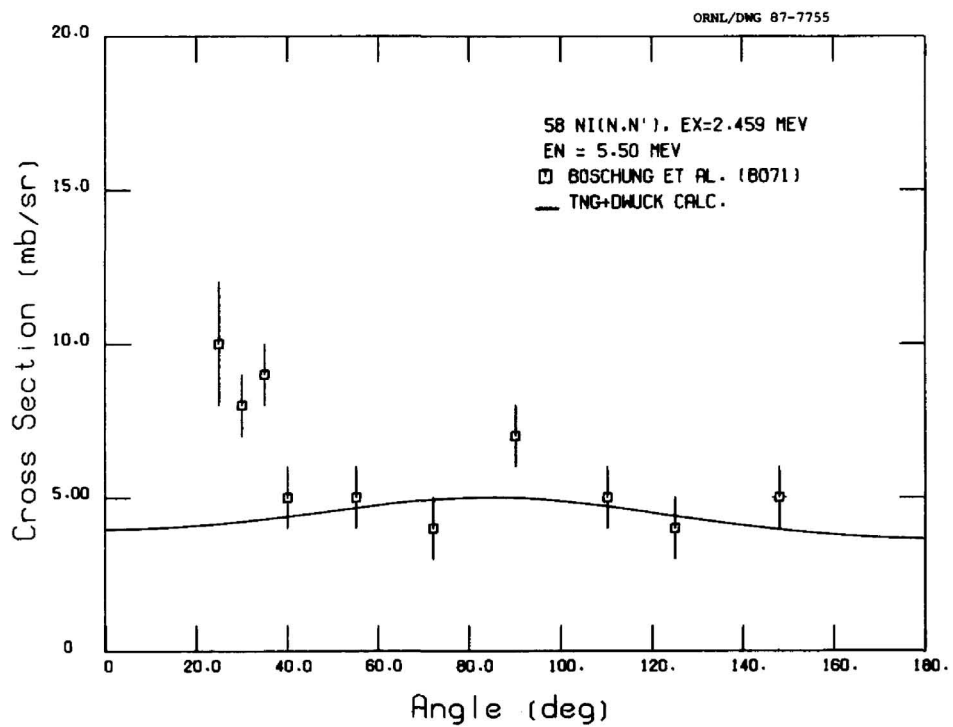


Fig. 18. Comparison of calculated and experimental differential cross sections for exciting the 2.459-MeV level at $E_n = 5.5$ MeV.

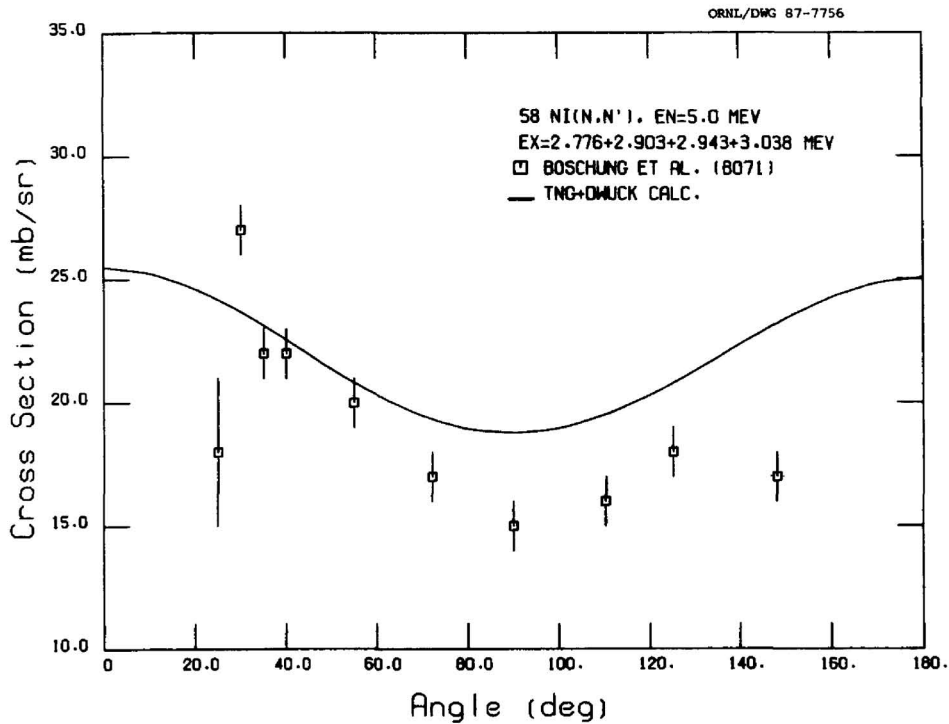


Fig. 19. Comparison of calculated and experimental differential cross sections for exciting the 2.776-, 2.903-, 2.943-, and 3.038-MeV levels at $E_n = 5.0$ MeV.

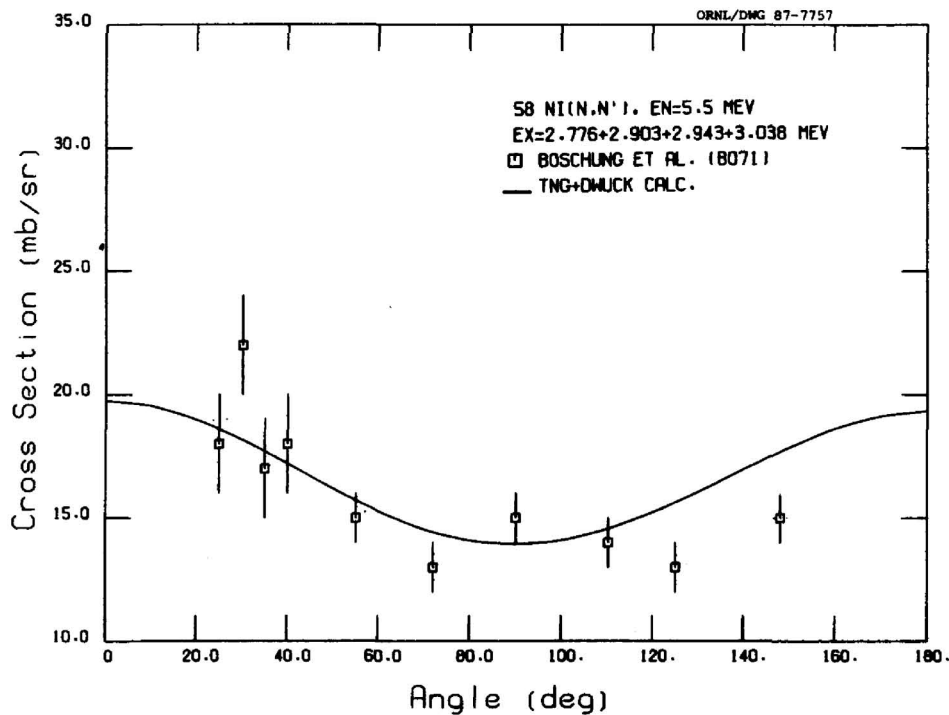


Fig. 20. Comparison of calculated and experimental differential cross sections for exciting the 2.776-, 2.903-, 2.943-, and 3.038-MeV levels at $E_n = 5.5$ MeV.

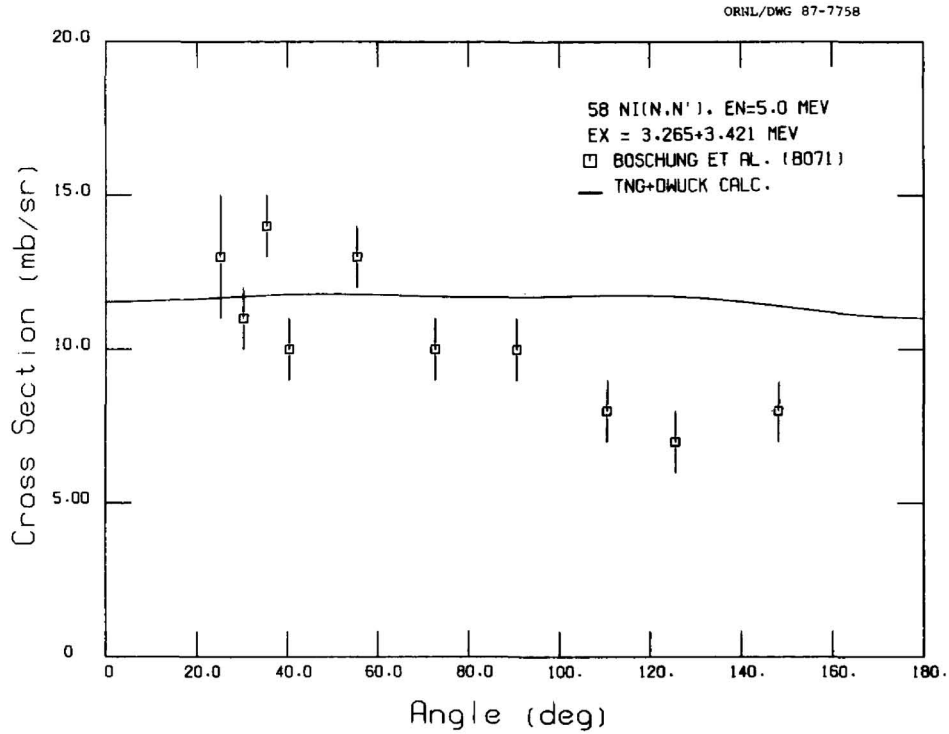


Fig. 21. Comparison of calculated and experimental differential cross sections for exciting the 3.265- and 3.421-MeV levels at $E_n = 5.0$ MeV.

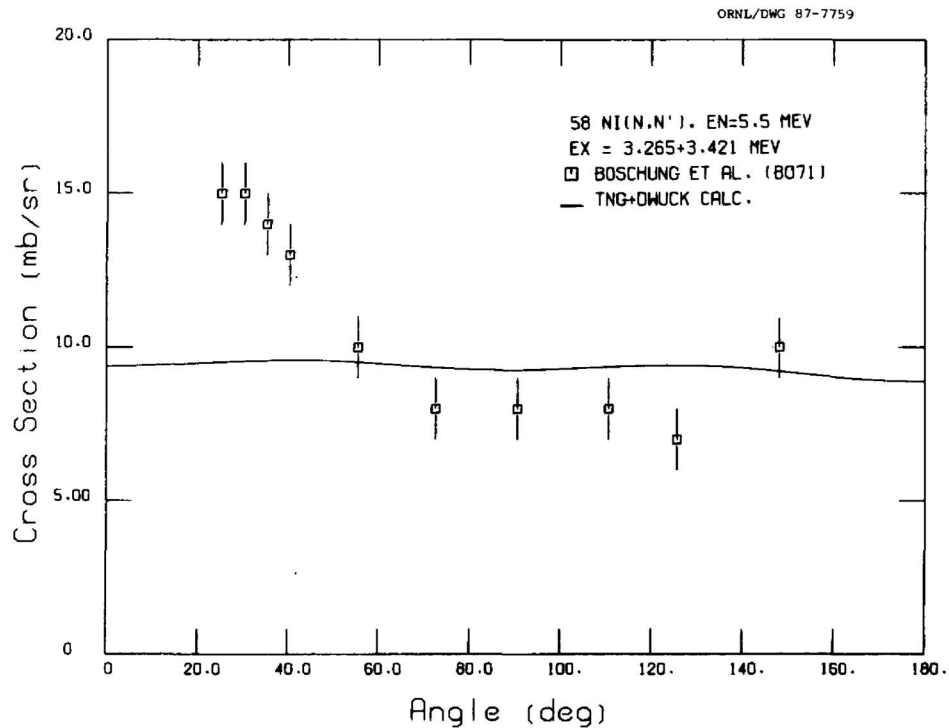


Fig. 22. Comparison of calculated and experimental differential cross sections for exciting the 3.265- and 3.421-MeV levels at $E_n = 5.5$ MeV.

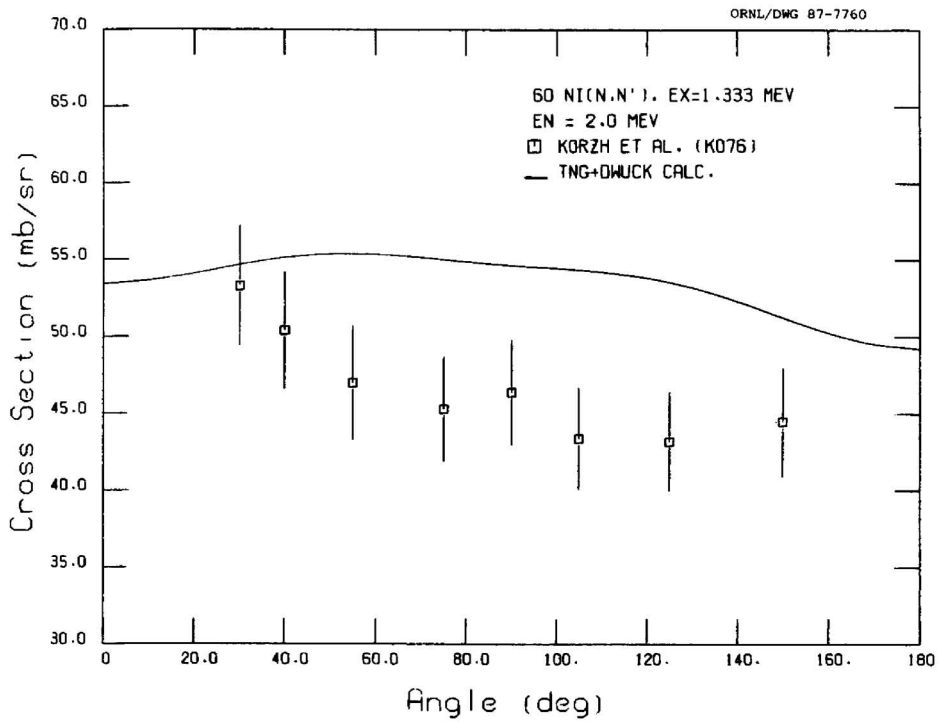


Fig. 23. Comparison of calculated and experimental differential cross sections for exciting the 1.333-MeV level at $E_n = 2.0$ MeV.

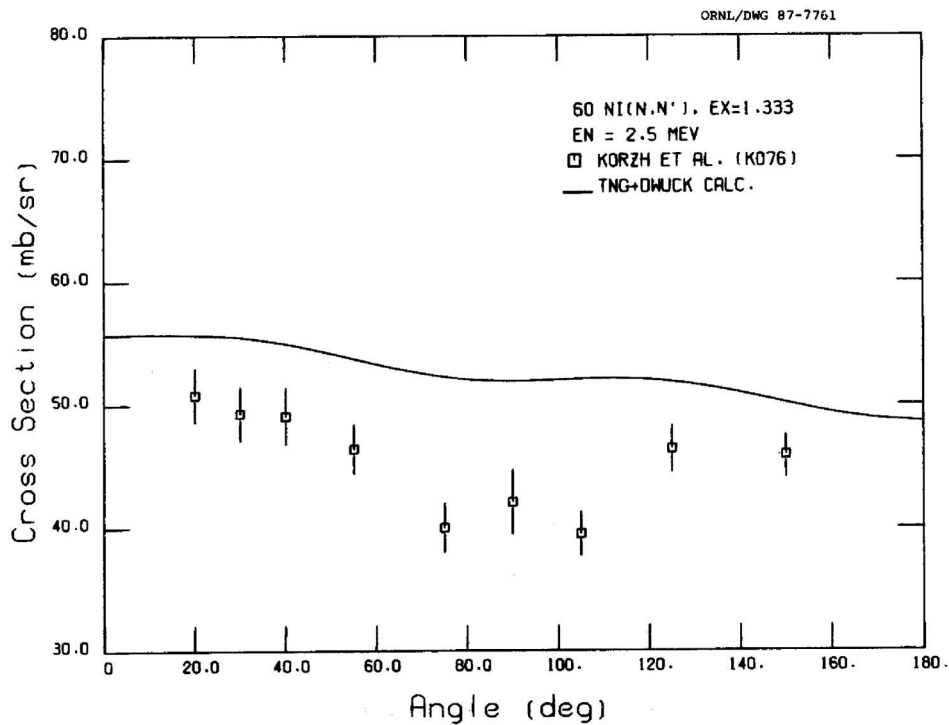


Fig. 24. Comparison of calculated and experimental differential cross sections for exciting the 1.333-MeV level at $E_n = 2.5$ MeV.

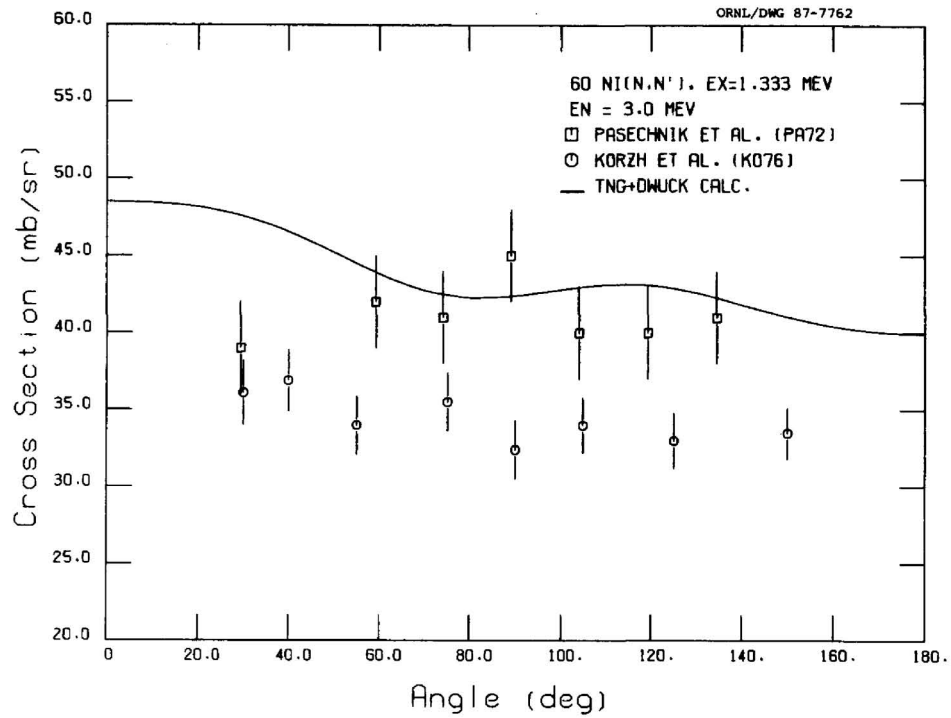


Fig. 25. Comparison of calculated and experimental differential cross sections for exciting the 1.333-MeV level at $E_n = 3.0$ MeV.

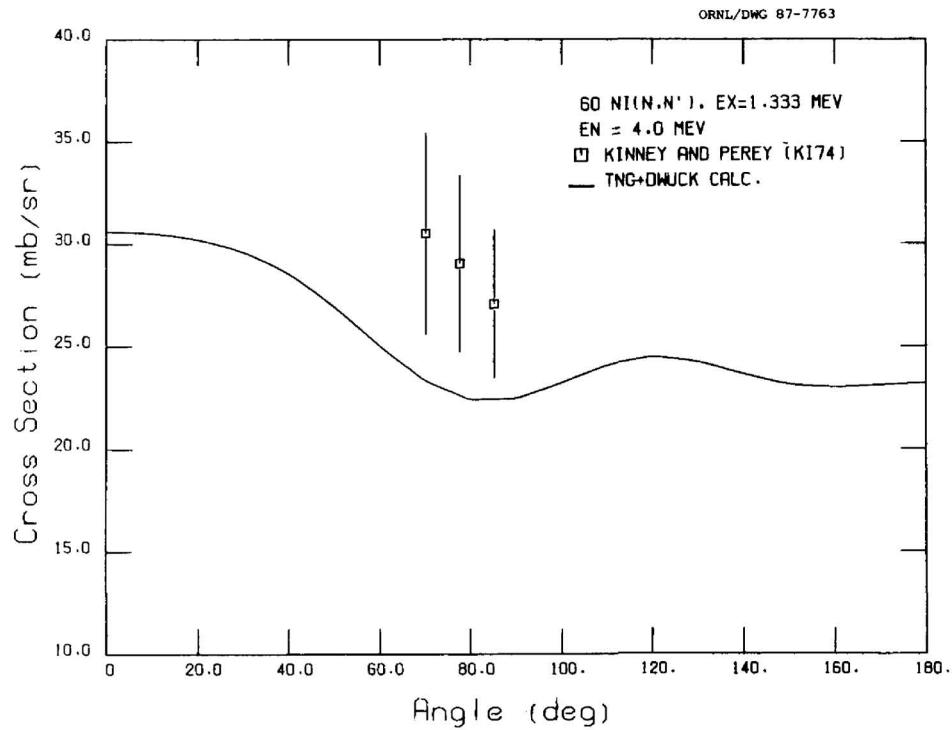


Fig. 26. Comparison of calculated and experimental differential cross sections for exciting the 1.333-MeV level at $E_n = 4.0$ MeV.

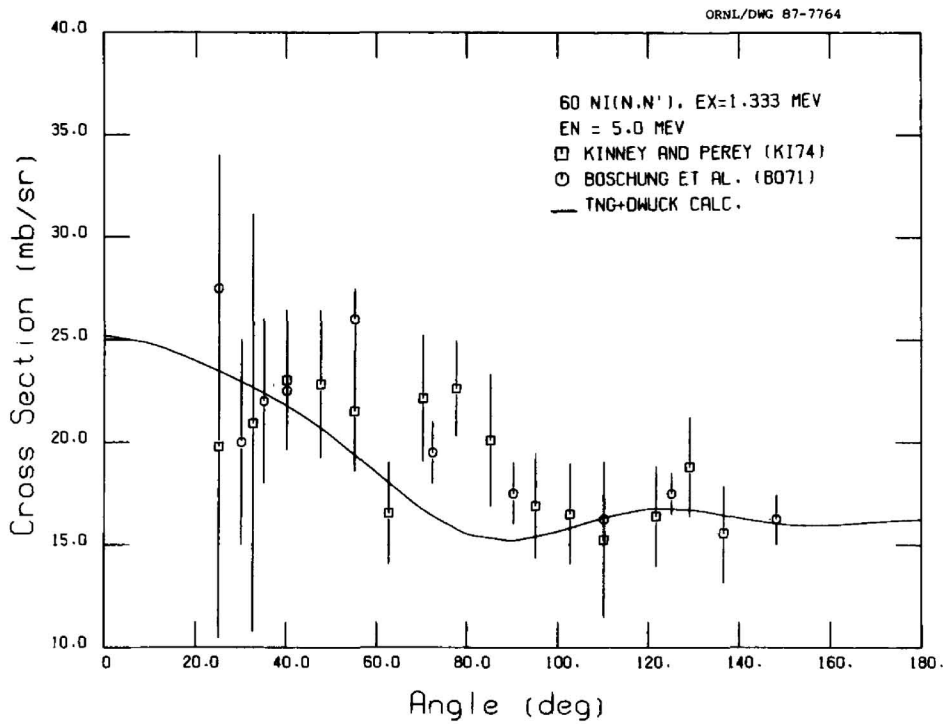


Fig. 27. Comparison of calculated and experimental differential cross sections for exciting the 1.333-MeV level at $E_n = 5.0$ MeV.

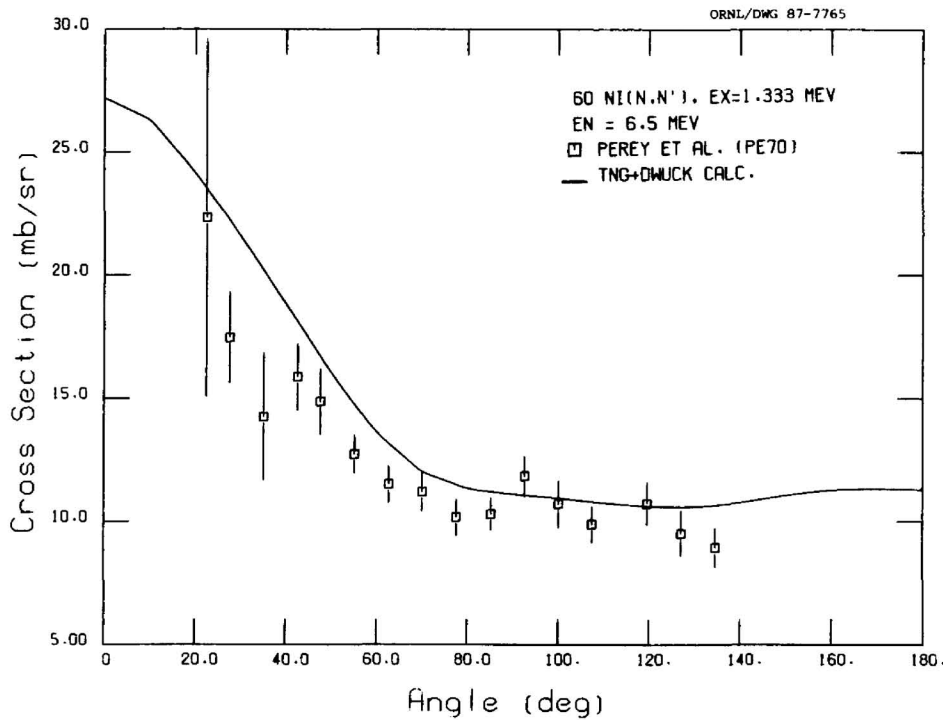


Fig. 28. Comparison of calculated and experimental differential cross sections for exciting the 1.333-MeV level at $E_n = 6.5$ MeV.

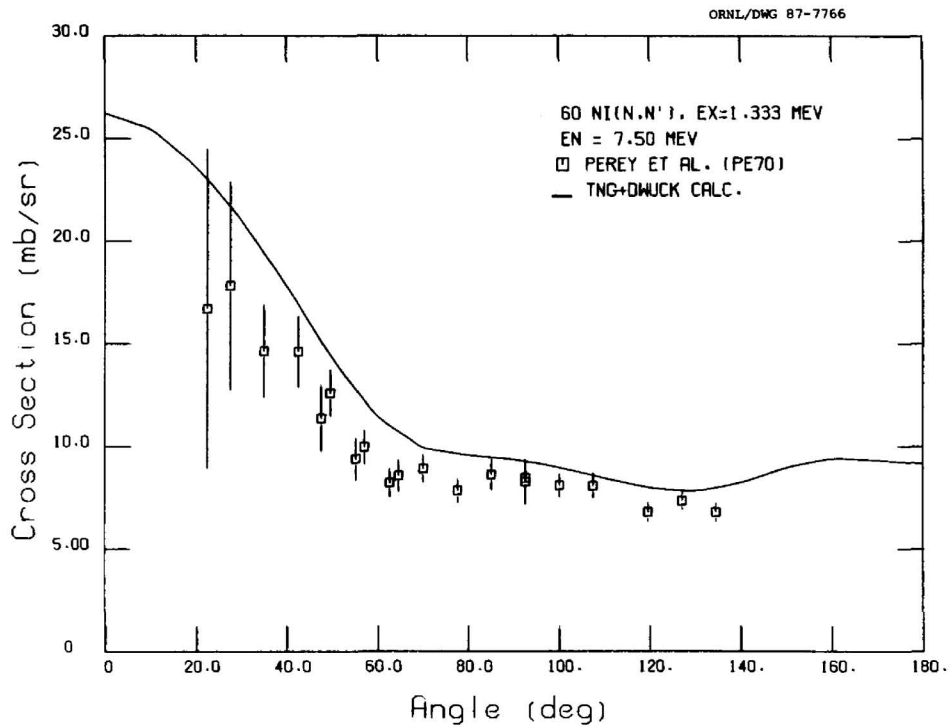


Fig. 29. Comparison of calculated and experimental differential cross sections for exciting the 1.333-MeV level at $E_n = 7.5$ MeV.

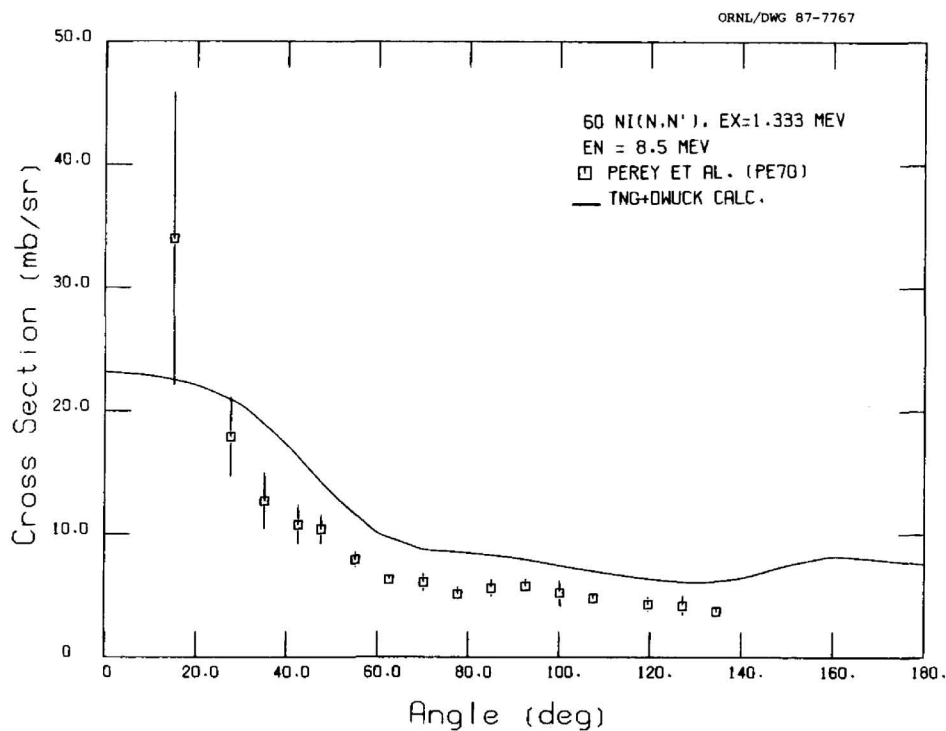


Fig. 30. Comparison of calculated and experimental differential cross sections for exciting the 1.333-MeV level at $E_n = 8.5$ MeV.

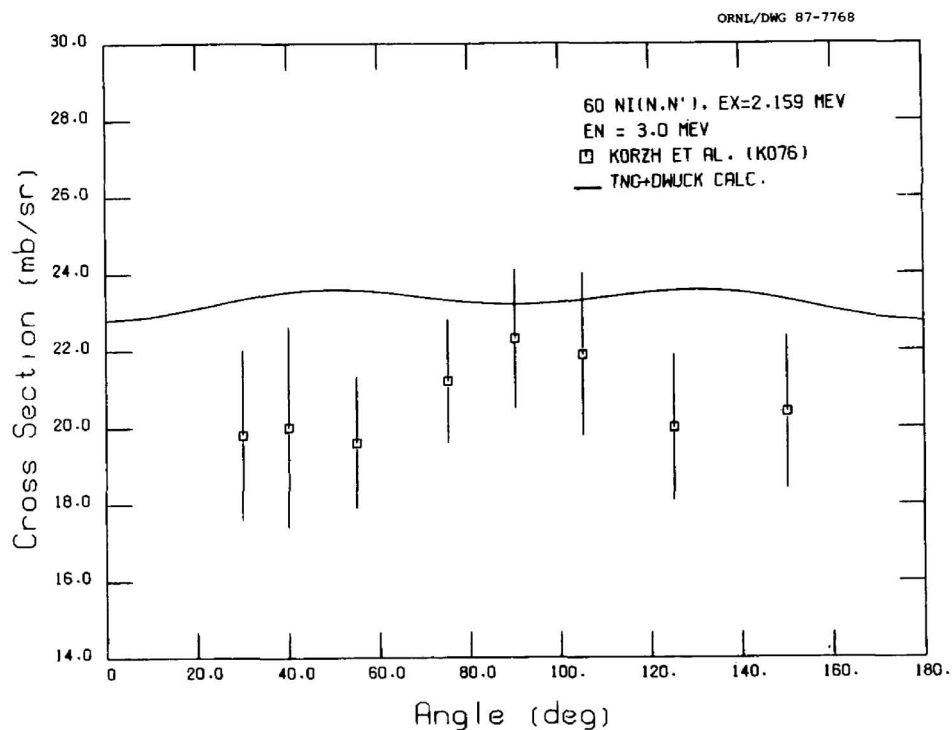


Fig. 31. Comparison of calculated and experimental differential cross sections for exciting the 2.159-MeV level at $E_n = 3.0$ MeV.

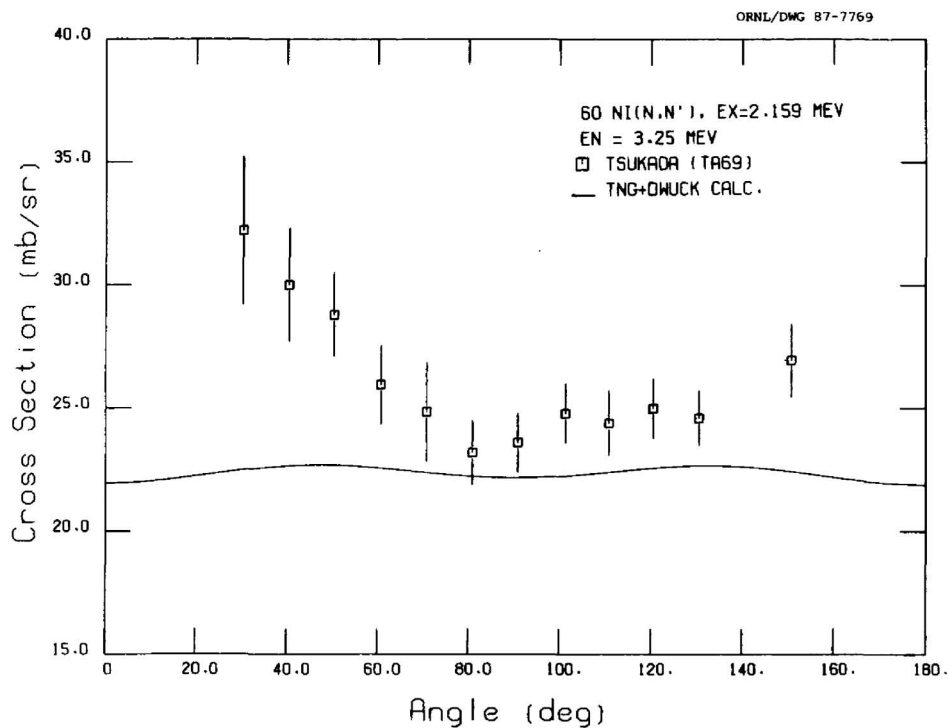


Fig. 32. Comparison of calculated and experimental differential cross sections for exciting the 2.159-MeV level at $E_n = 3.25$ MeV.

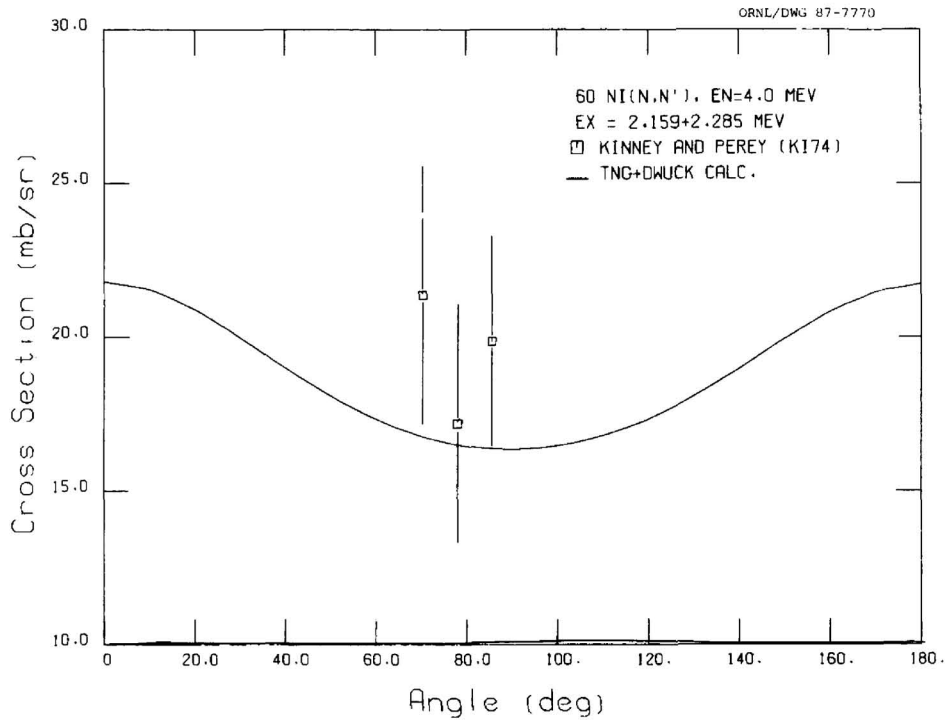


Fig. 33. Comparison of calculated and experimental differential cross sections for exciting the 2.159- and 2.285-MeV levels at $E_n = 4.0$ MeV.

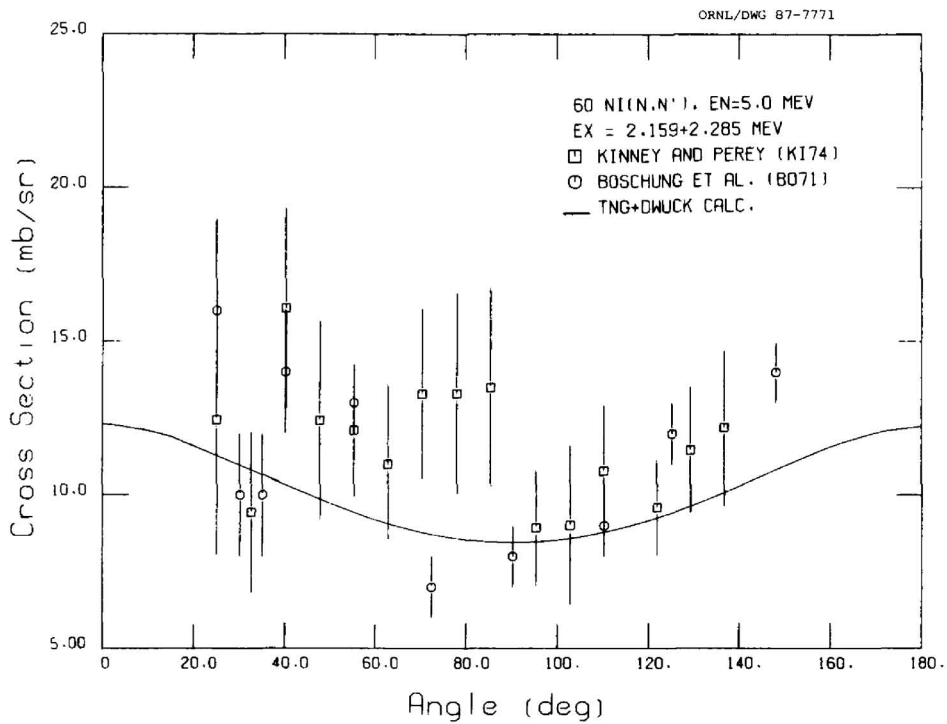


Fig. 34. Comparison of calculated and experimental differential cross sections for exciting the 2.159- and 2.285-MeV levels at $E_n = 5.0$ MeV.

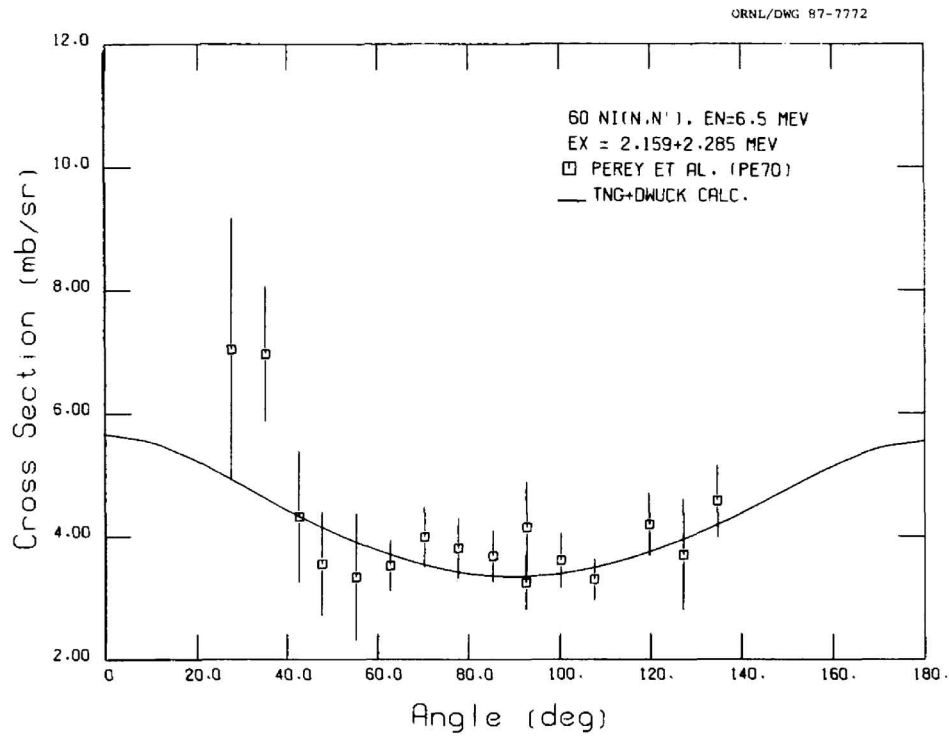


Fig. 35. Comparison of calculated and experimental differential cross sections for exciting the 2.159- and 2.285-MeV levels at $E_n = 6.5$ MeV.

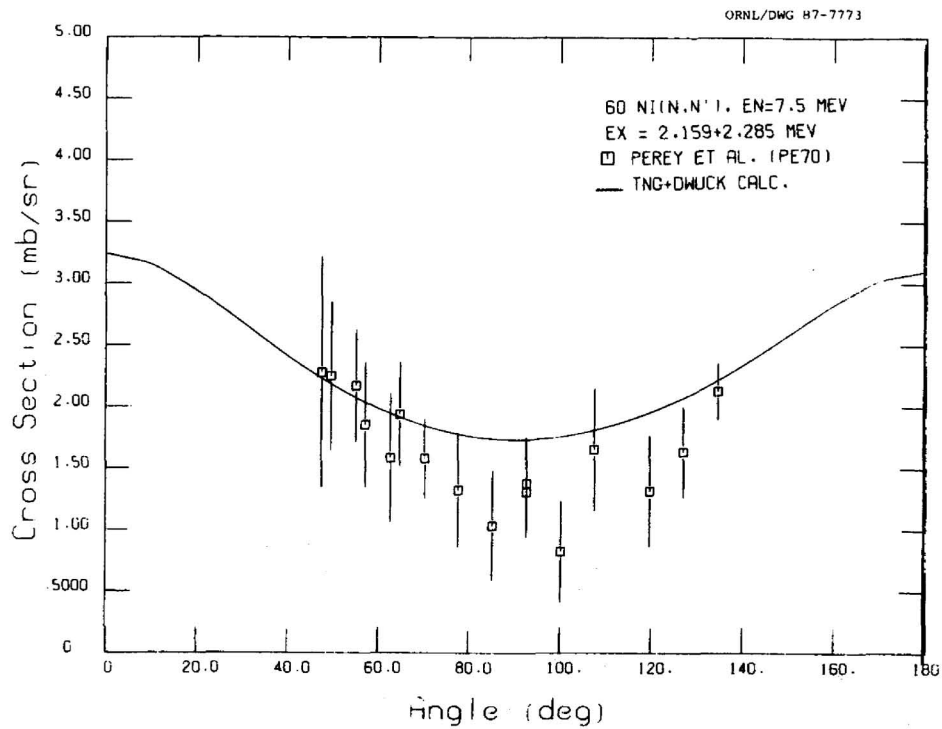


Fig. 36. Comparison of calculated and experimental differential cross sections for exciting the 2.159- and 2.285-MeV levels at $E_n = 7.5$ MeV.

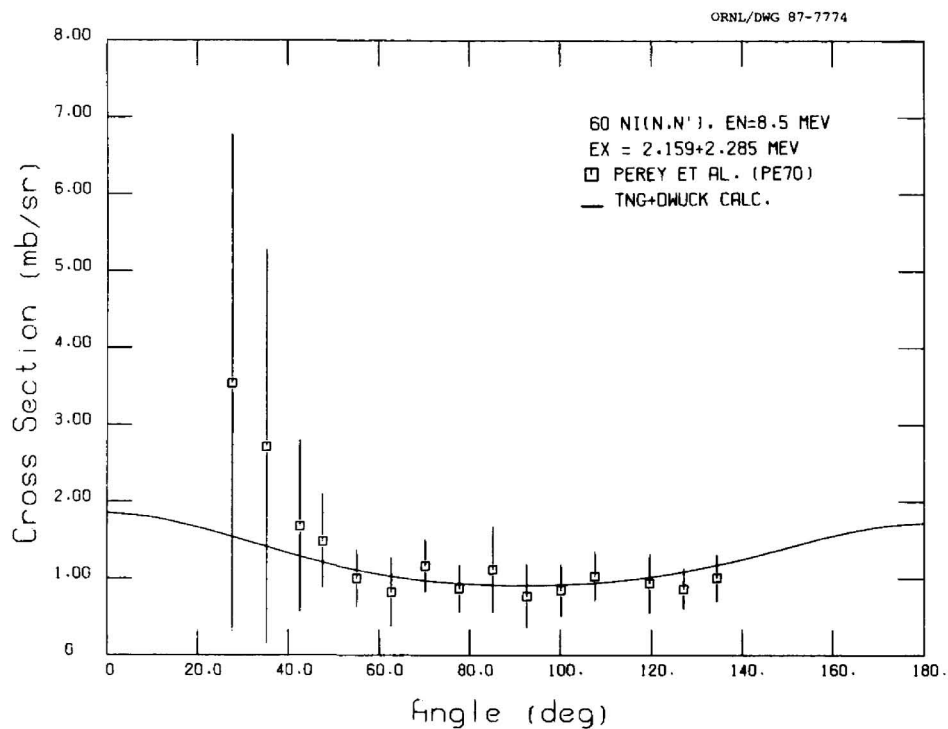


Fig. 37. Comparison of calculated and experimental differential cross sections for exciting the 2.159- and 2.285-MeV levels at $E_n = 8.5$ MeV.

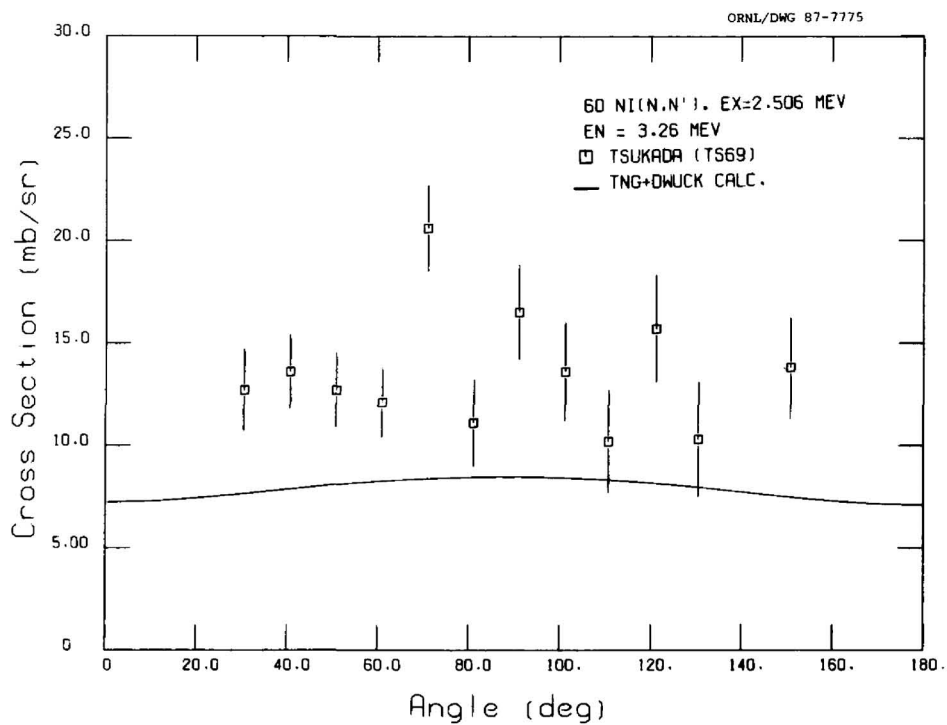


Fig. 38. Comparison of calculated and experimental differential cross sections for exciting the 2.506-MeV level at $E_n = 3.26$ MeV.

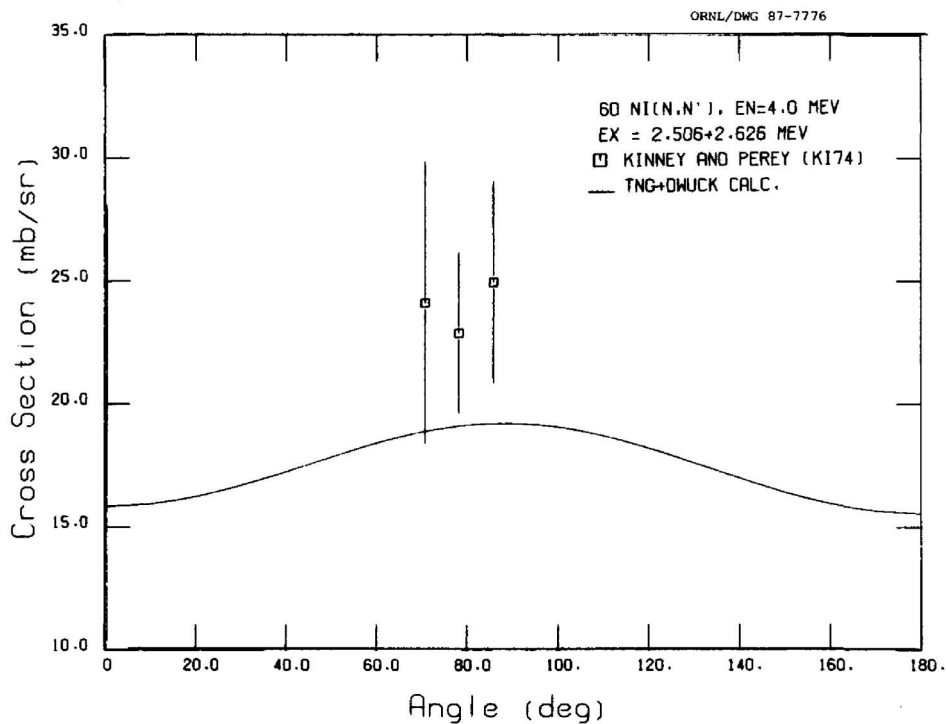


Fig. 39. Comparison of calculated and experimental differential cross sections for exciting the 2.506- and 2.626-MeV levels at $E_n = 4.0$ MeV.

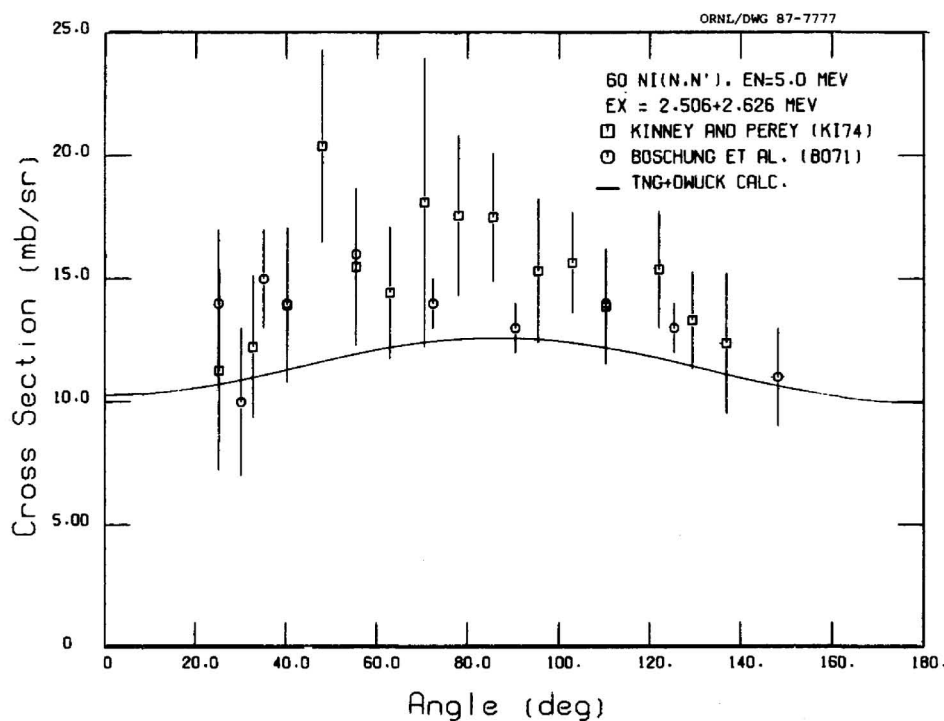


Fig. 40. Comparison of calculated and experimental differential cross sections for exciting the 2.506- and 2.626-MeV levels at $E_n = 5.0$ MeV.

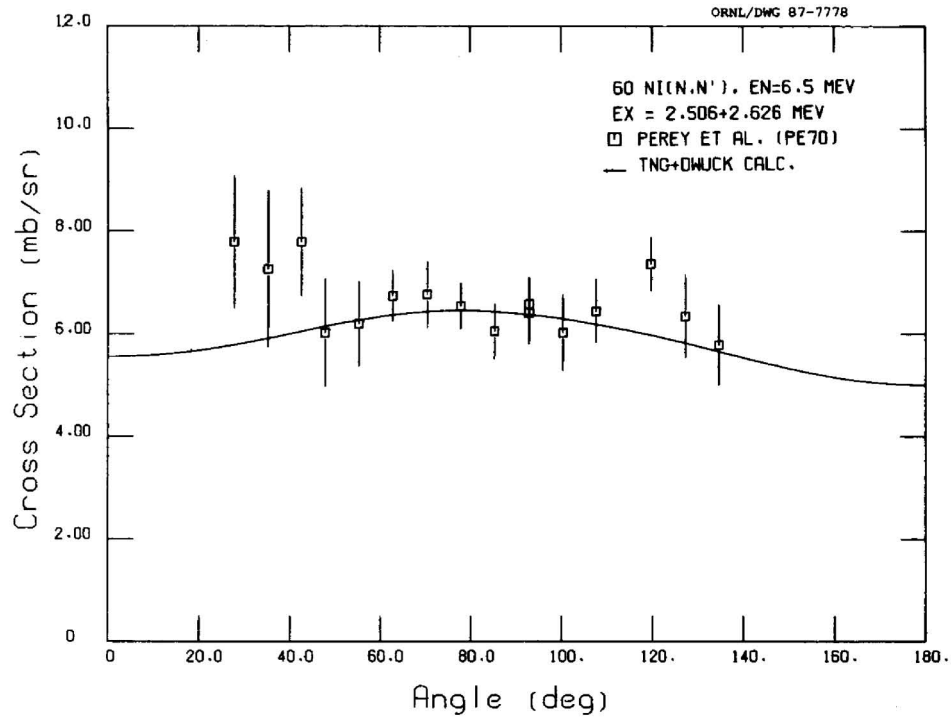


Fig. 41. Comparison of calculated and experimental differential cross sections for exciting the 2.506- and 2.626-MeV levels at $E_n = 6.5$ MeV.

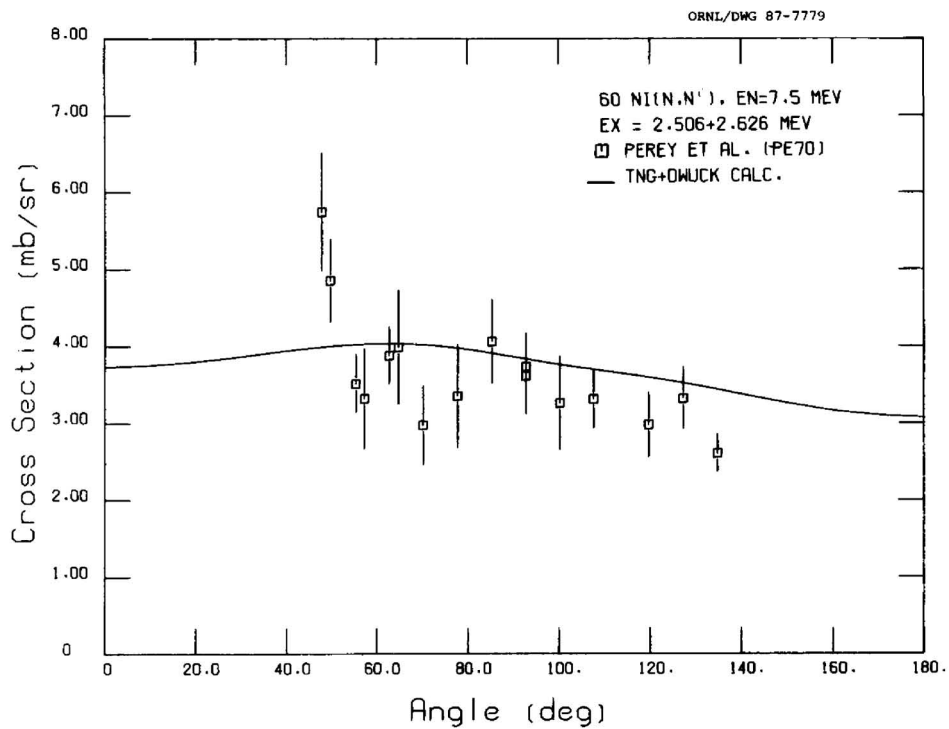


Fig. 42. Comparison of calculated and experimental differential cross sections for exciting the 2.506- and 2.626-MeV levels at $E_n = 7.5$ MeV.

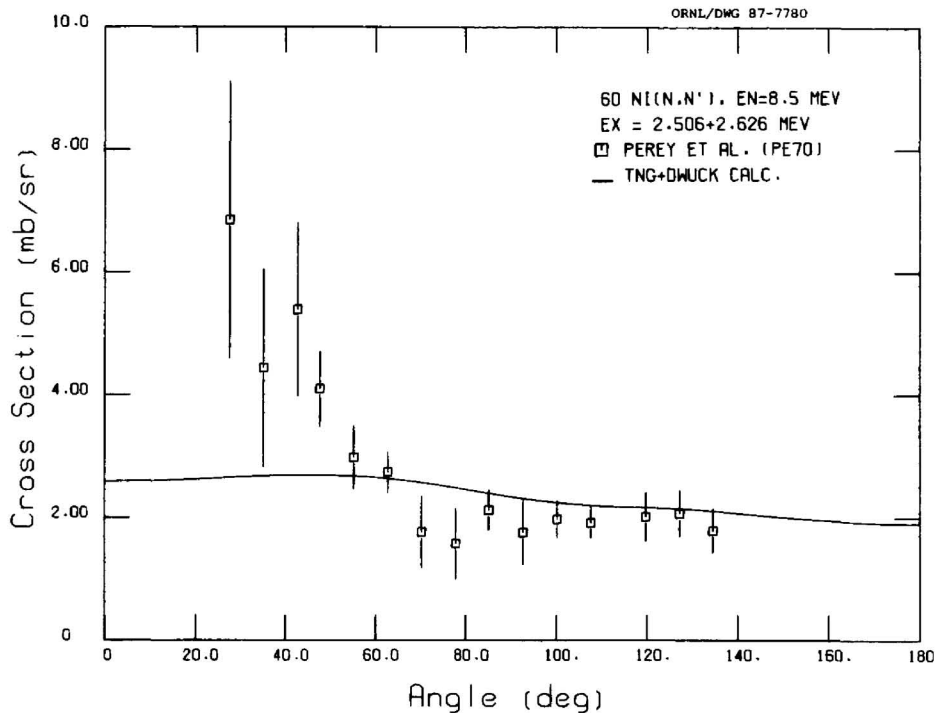


Fig. 43. Comparison of calculated and experimental differential cross sections for exciting the 2.506- and 2.626-MeV levels at $E_n = 8.5$ MeV.

4.6 INELASTIC SCATTERING TO DISCRETE LEVELS

The comparison of calculated and experimental (n,n') cross sections for individual levels and groups of levels for both ^{58}Ni and ^{60}Ni is given in Figs. 44 through 52. The calculated direct interaction cross sections (see Figs. 1 and 2) are included. Disagreement among measured data is quite large (e.g., see Figs. 44 and 49), and the calculation represents a good compromise in these cases. Overall, the agreement is quite good.

4.7 ANGULAR DISTRIBUTIONS OF NEUTRON-PRODUCTION CROSS SECTIONS

The computed angular distributions of neutron production cross sections for nickel at an incident energy of 14.5 MeV and for secondary energies of $E_n' = 4.0-5.0$, 6.0-7.0, and 8.0-9.0 MeV are compared with experiments in Fig. 53. Again, discrepancies exist between the measured data sets. The calculation agrees best with the data of Hermsdorf et al. (HE75) and Salnikov et al. (SA72), but disagrees with the measurements of Takahashi et al. (TA83) and Clayeux and Voignier (CL72).

4.8 NEUTRON EMISSION SPECTRA

Neutron emission spectra were computed for 35 incident energies; however, measurements were available only for the incident neutron energy range from 14.1 to 14.8 MeV. Comparison of the calculated neutron spectra at an incident energy of 14.5 MeV with the experimental data is shown in Fig. 54. The data of Clayeux and Voignier (CL72) and Mathur et al. (MA69) were measured at 90° ,

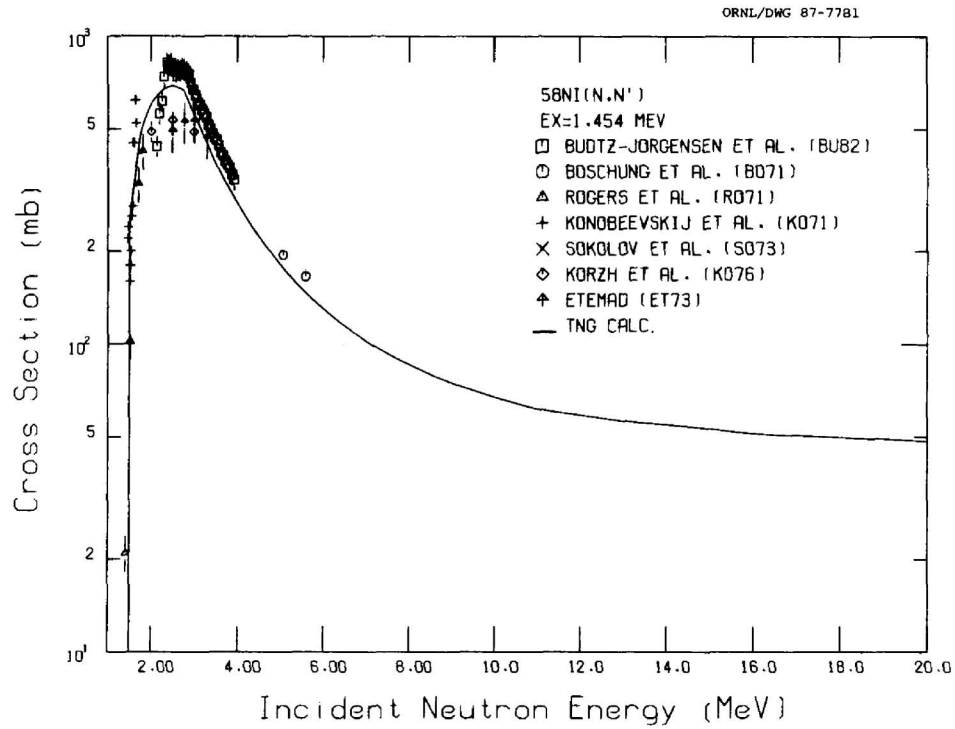


Fig. 44. Comparison of calculated and experimental $^{58}\text{Ni}(n,n')$ cross sections for exciting the 1.454-MeV level.

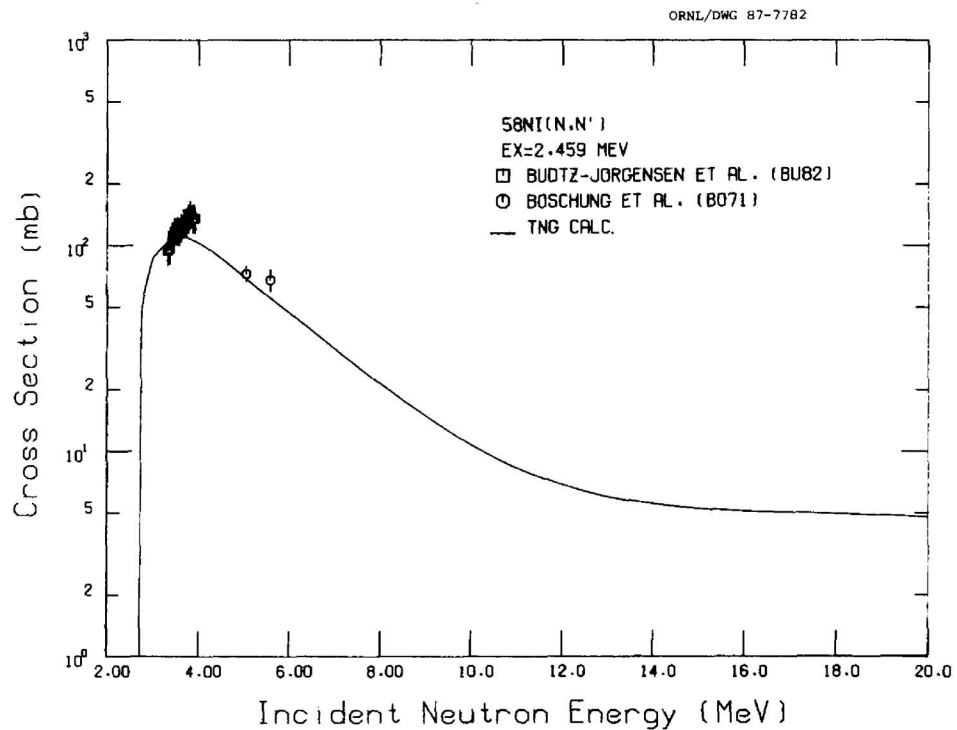


Fig. 45. Comparison of calculated and experimental $^{58}\text{Ni}(n,n')$ cross sections for exciting the 2.459-MeV level.

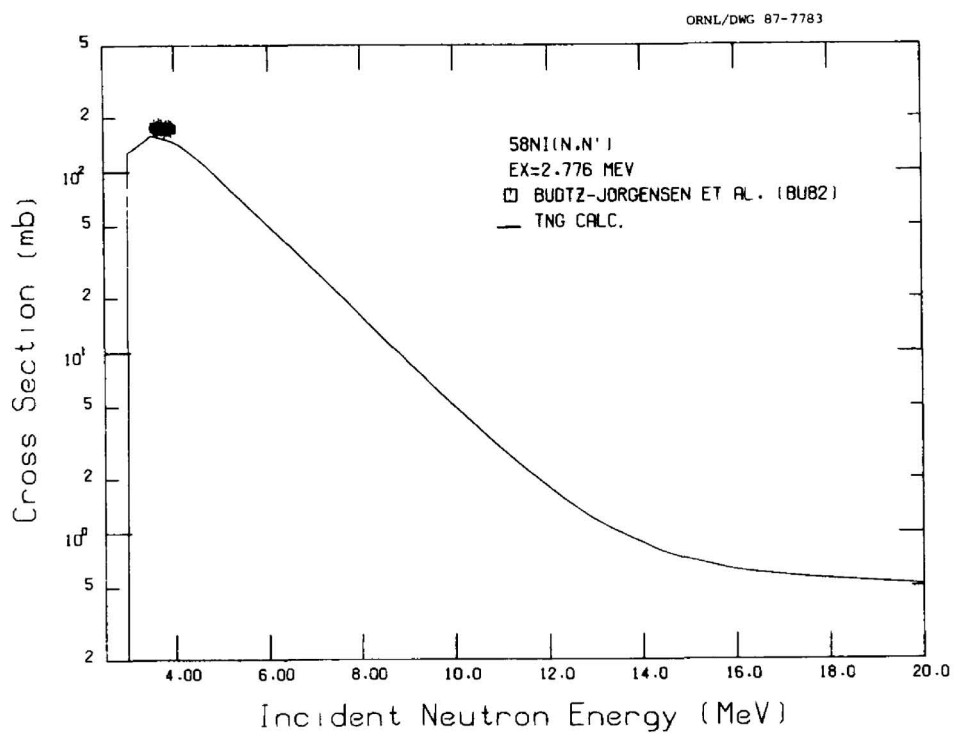


Fig. 46. Comparison of calculated and experimental $^{58}\text{Ni}(n,n')$ cross sections for exciting the 2.776-MeV level.

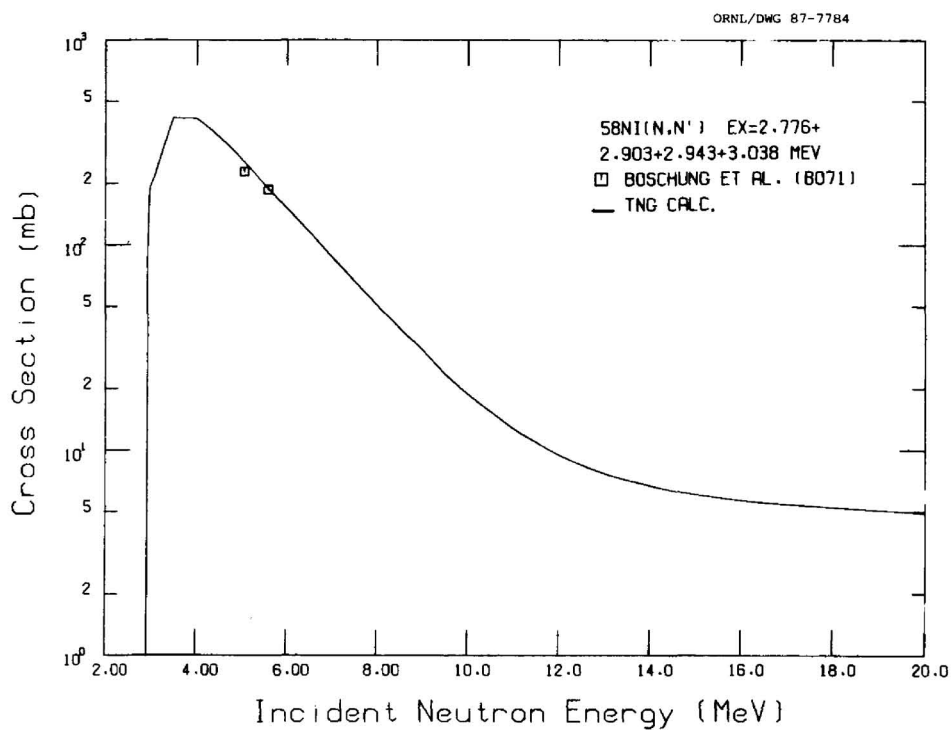


Fig. 47. Comparison of calculated and experimental $^{58}\text{Ni}(n,n')$ cross sections for exciting the 2.776-, 2.903-, 2.943-, and 3.038-MeV levels.

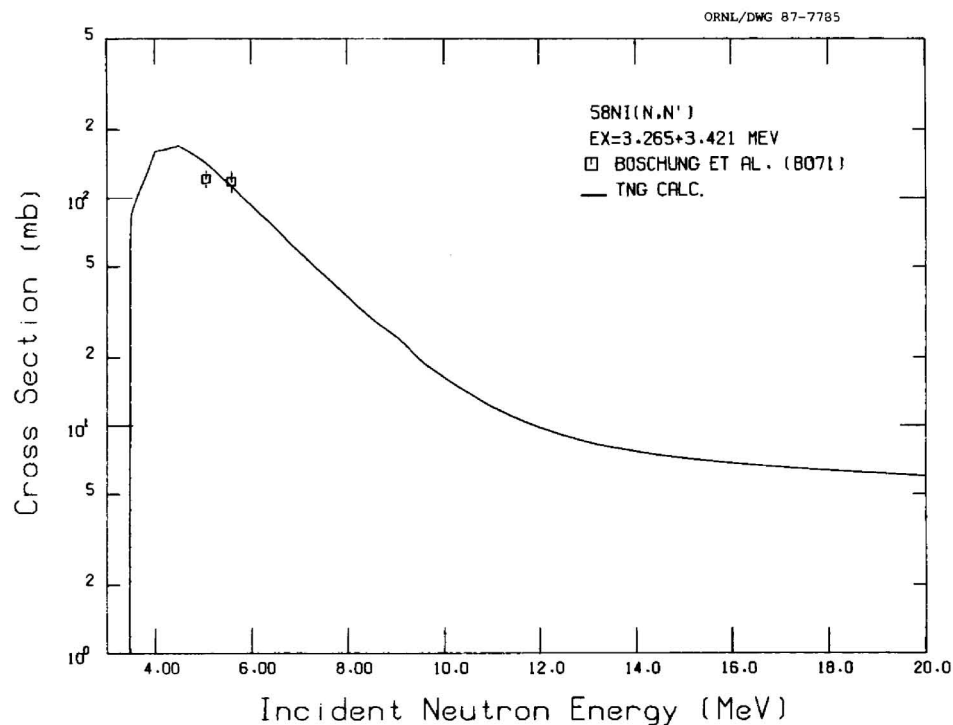


Fig. 48. Comparison of calculated and experimental $^{58}\text{Ni}(n,n')$ cross sections for exciting the 3.265- and 3.421-MeV levels.

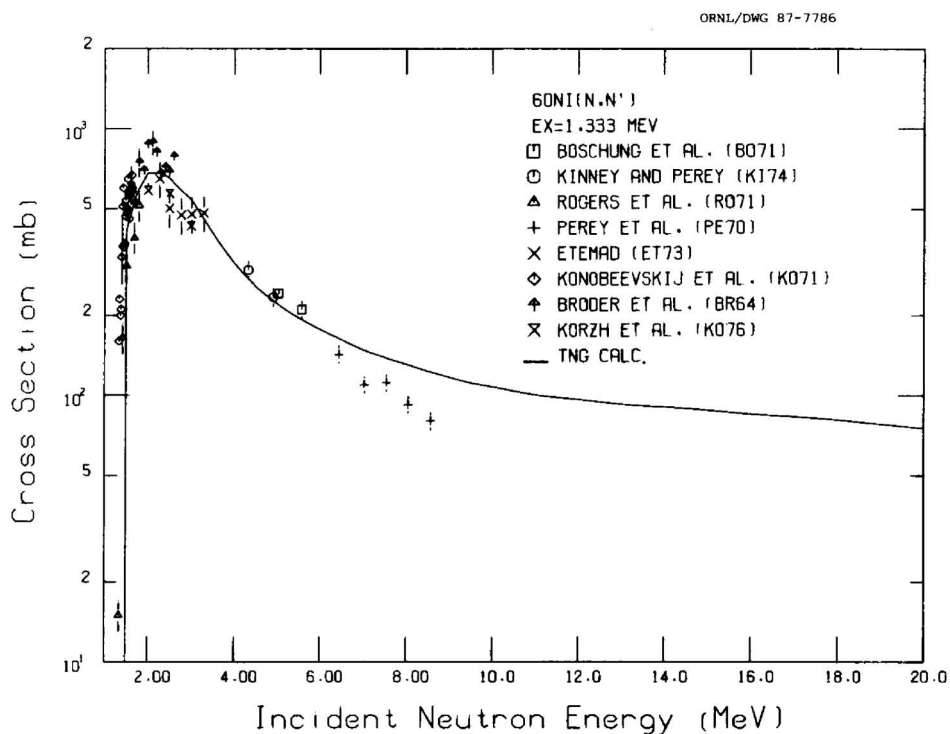


Fig. 49. Comparison of calculated and experimental $^{60}\text{Ni}(n,n')$ cross sections for exciting the 1.333-MeV level.

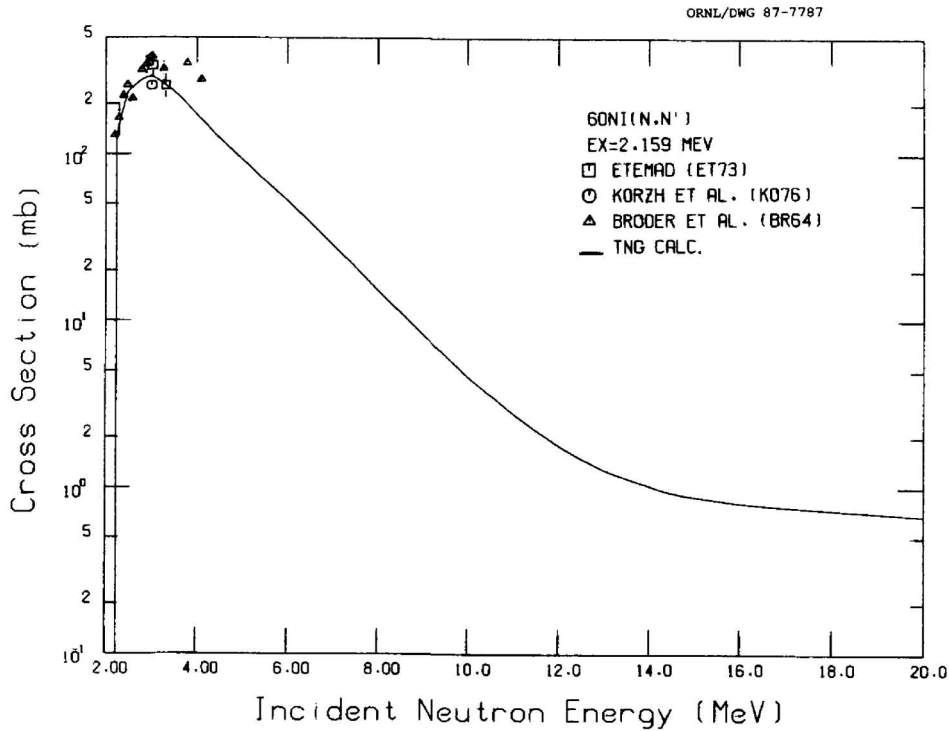


Fig. 50. Comparison of calculated and experimental $^{60}\text{Ni}(n,n')$ cross sections for exciting the 2.159-MeV level.

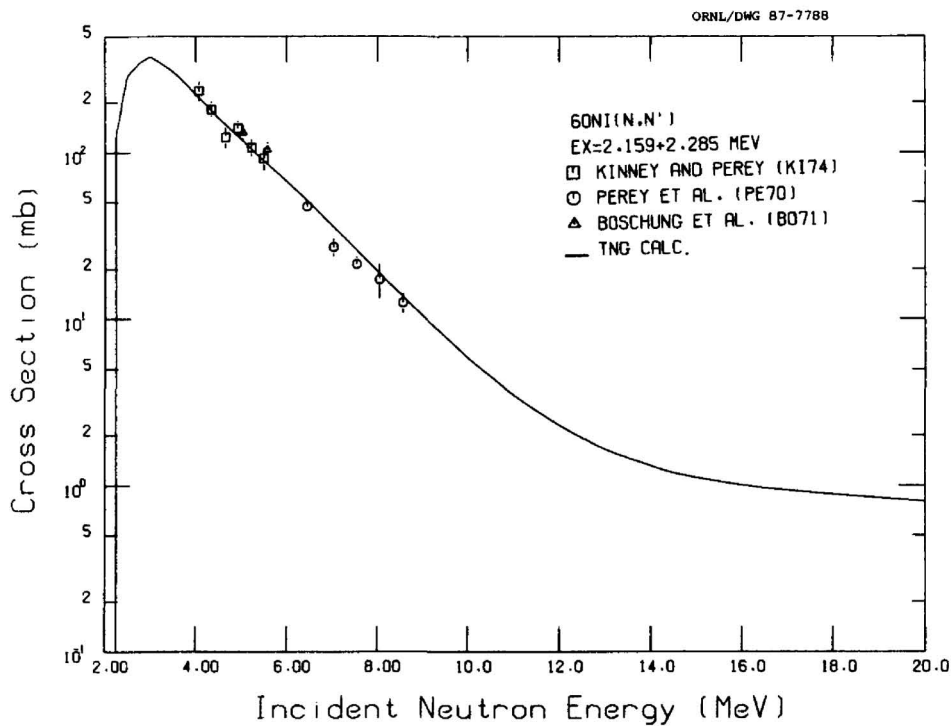


Fig. 51. Comparison of calculated and experimental $^{60}\text{Ni}(n,n')$ cross sections for exciting the 2.159- and 2.285-MeV levels.

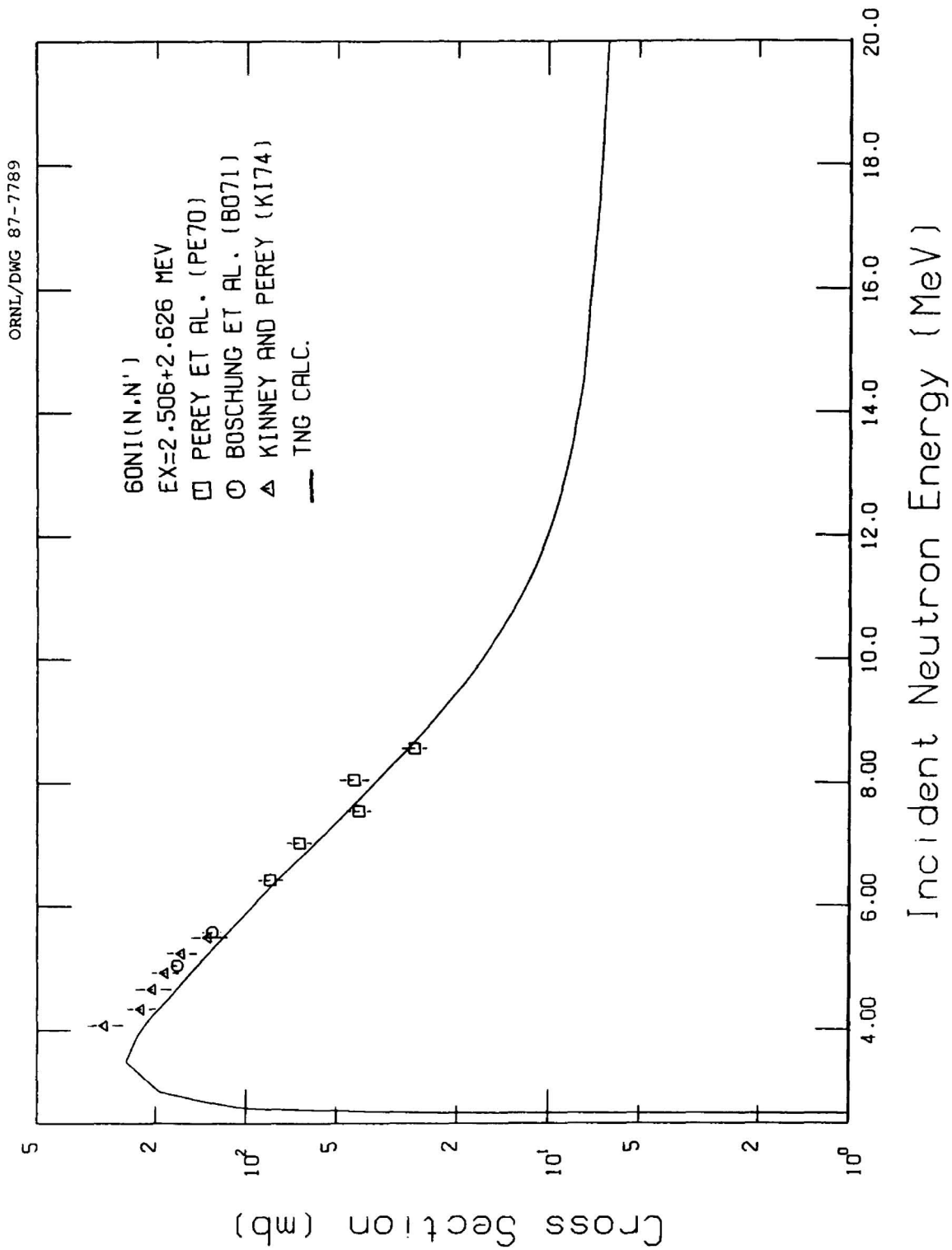


Fig. 52. Comparison of calculated and experimental $^{60}\text{Ni}(n,n')$ cross sections for exciting the 2.506- and 2.626-MeV levels.

ORNL-DWG 85-9840R

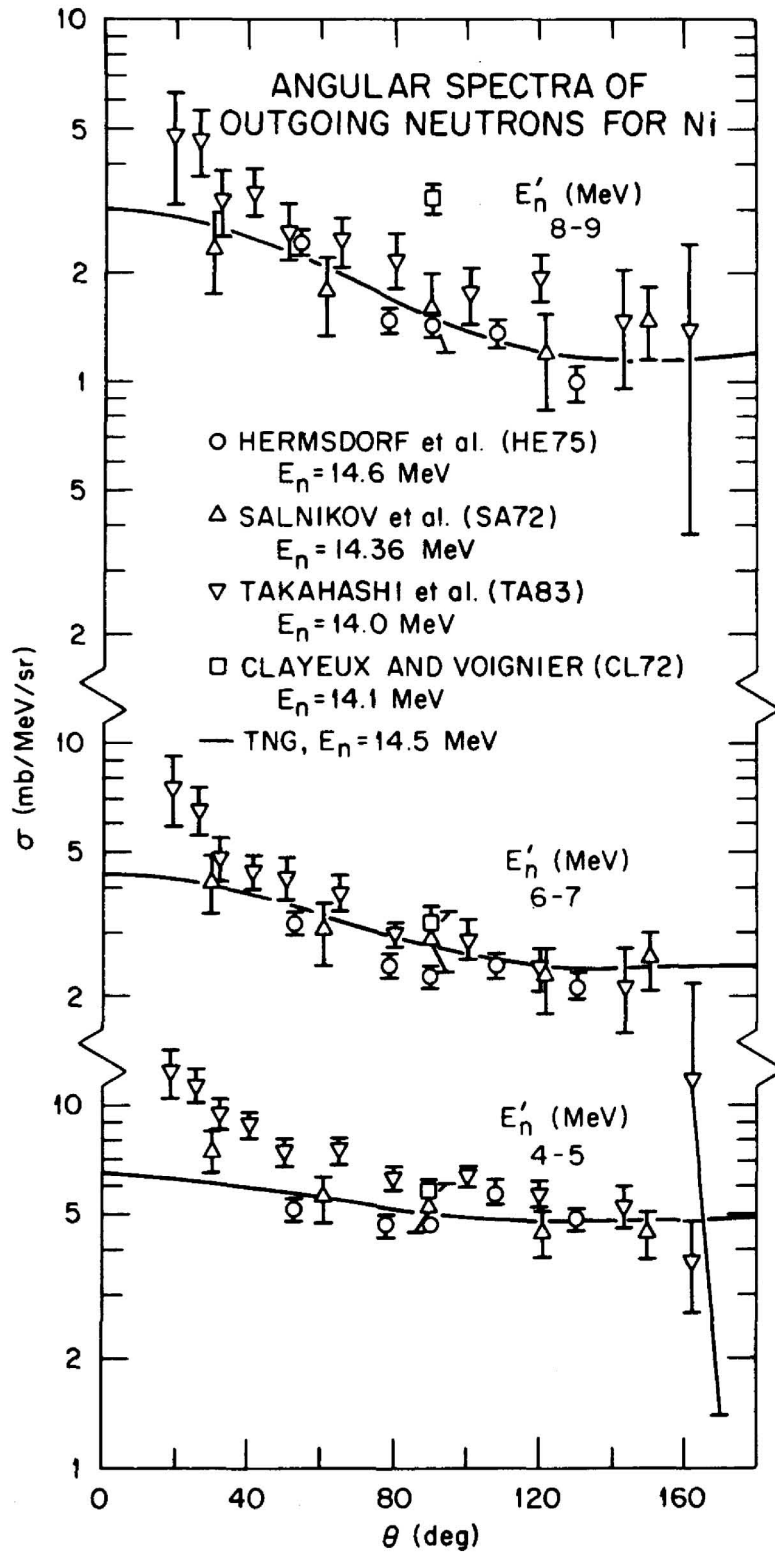


Fig. 53. Comparison of calculated and experimental neutron production cross sections.

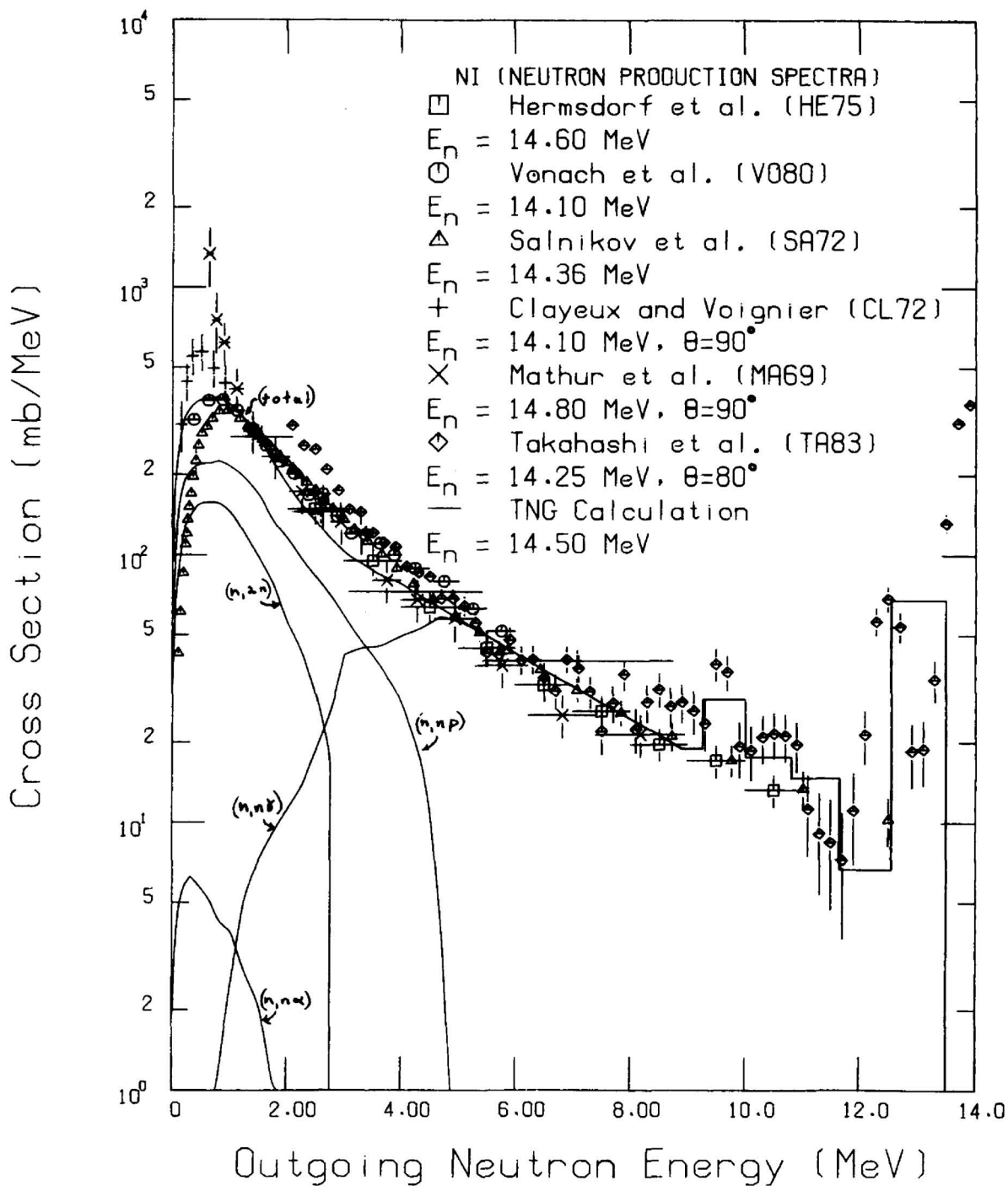


Fig. 54. Neutron emission spectra from the TNG calculation compared with experimental data. The data of Clayeux and Voignier (CL72) and Mathur et al. (MA69) were taken at 90° , the data of Takahashi et al. (TA83) were taken at 80° , and the other measured data sets shown (HE75, VO80, and SA72) are angle integrated. Contributions from the various neutron-producing components are shown (they sum to the total). The curves labeled (n,np) and (n,n α) include the (n,pn) and (n,an) components, respectively.

the data of Takahashi et al. (TA83) were measured at 80° , and the other measurements (HE75, VO80, SA72) are angle integrated. The figure shows the calculated total neutron emission spectra, as well as the calculated emission spectra from the individual contributing reactions. The (n,n') continuum and discrete level computations were combined into the one curve labeled " $(n,n\gamma)$ ". The curve labeled " (n,np) " includes contributions from both the (n,np) and (n,pn) reactions. Likewise, the curve labeled " $(n,n\alpha)$ " includes contributions from both the $(n,n\alpha)$ and $(n,\alpha n)$ reactions. The curve labeled "TNG Calculation" is the computed angle-integrated spectrum and includes the angle-integrated direct inelastic cross sections from the DWUCK code (these were input to the TNG code).

4.9 PROTON AND ALPHA-PARTICLE EMISSION SPECTRA

The calculated (n,xp) and $n,x\alpha$ spectra for both ^{58}Ni and ^{60}Ni are compared to measurements by Grimes et al. (GR79, HA77), Colli et al. (CO62), and Fischer et al. (FI84) in Figs. 55 through 58. The data of Colli et al. were measured at 15° ; the other data are angle integrated. The (n,xp) spectra are sums of the partial spectra from the (n,p) , (n,pn) , and (n,np) reactions. Likewise, the $(n,x\alpha)$ spectra are sums of (n,α) , $(n,\alpha n)$ and $(n,n\alpha)$. The measurements of Grimes et al. were taken at an incident energy of 14.8 MeV, and the data of Colli et al. and Fischer et al. were taken at an incident energy of 14.1 MeV. The TNG results were calculated at an incident energy of 14.5 MeV and are in very good agreement with the data.

4.10 BINARY AND TERTIARY REACTION CROSS SECTIONS

The calculated binary and tertiary cross sections for ^{58}Ni and ^{60}Ni are compared to available data in Figs. 59 through 69. Figure 59 shows the results for $^{58}\text{Ni}(n,p)$. Numerous other data sets were available for $^{58}\text{Ni}(n,p)$ from the CSISRS library (CS86); only those sets with six or more data points are included in Fig. 59. The data are quite discrepant in the region above an incident energy of 13 MeV, but the calculation agrees very well with the data of Pavlik et al. (PA85), Viennot et al. (VI82), and Paulsen and Widera (PA71) in this energy range. The $^{60}\text{Ni}(n,p)$ data and calculation are shown in Fig. 60 with good overall agreement. The computed $^{58}\text{Ni}[(n,np) + (n,pn)]$ excitation function is compared to available data in Fig. 61. Again, the data disagree around an incident energy of 14 MeV, but the calculation is in excellent agreement with the recent data of Pavlik et al. (PA85). Figures 62 and 63 show the calculated total proton emission versus data for ^{58}Ni and ^{60}Ni . In both cases, the calculation agrees well with the data of Grimes et al. (GR79). Note that the measured $^{58}\text{Ni}(n,p)$ and $^{60}\text{Ni}(n,p)$ data from Figs. 59 and 60 for incident energies less than approximately 9.0 MeV could have been included on Figs. 62 and 63, respectively.

Other data sets were available for $^{58}\text{Ni}(n,2n)$ from the CSISRS library (CS86); only those sets with five or more data points are included in Fig. 64. The calculation is smaller than the more recent data of Pavlik et al. (PA82) and Han-Lin et al. (HA82a) for incident energies greater than 14.5 MeV, but does agree well with the measurements of Paulsen and Liskien (PA65), Bormann et al. (BO66), and Hudson et al. (HU78). Comparison of calculation to data for natural nickel is shown in Fig. 65. The solid line represents the ^{58}Ni calculation (multiplied by 0.71) plus the ^{60}Ni calculation (multiplied by 0.29). However, the $(n,2n)$ cross sections are large for the minor isotopes. The dashed line is the sum of the TNG calculations for ^{58}Ni and ^{60}Ni added to the calculations of Divadeenam (DI79) for ^{61}Ni , ^{62}Ni and ^{64}Ni . In this case, the cross sections for each isotope were multiplied by its fractional natural abundance (68.3% for ^{58}Ni , 26.1% for ^{60}Ni , 1.1% for ^{61}Ni , 3.6% for ^{62}Ni , and 0.9% for ^{64}Ni) and summed to obtain the results. The calculated cross sections (dashed curve) are still smaller than the data, but since there are no $(n,2n)$ measurements available for any of the isotopes besides ^{58}Ni , it is difficult to determine whether or not the TNG calculation for either $^{58}\text{Ni}(n,2n)$ or $^{60}\text{Ni}(n,2n)$ is too small.

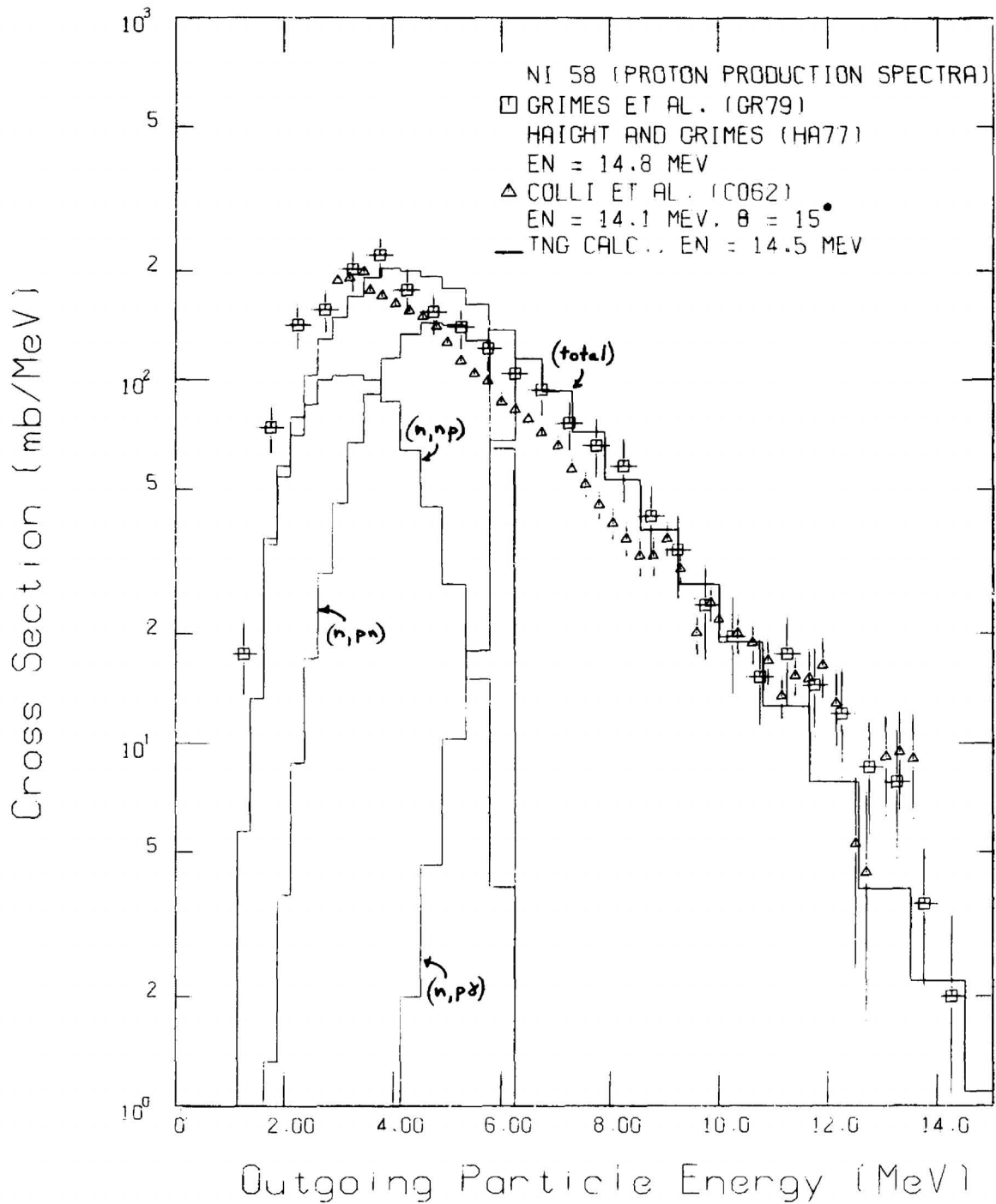


Fig. 55. Comparison of calculated experimental proton production spectra for ^{58}Ni . The measurements were taken at incident energies of 14.8 and 14.1 MeV; the TNG calculation was for $E_n = 14.5$ MeV. The data of Grimes et al. (GR79, HA77) are angle integrated; the data of Colli et al. (CO62) were taken at 15° .

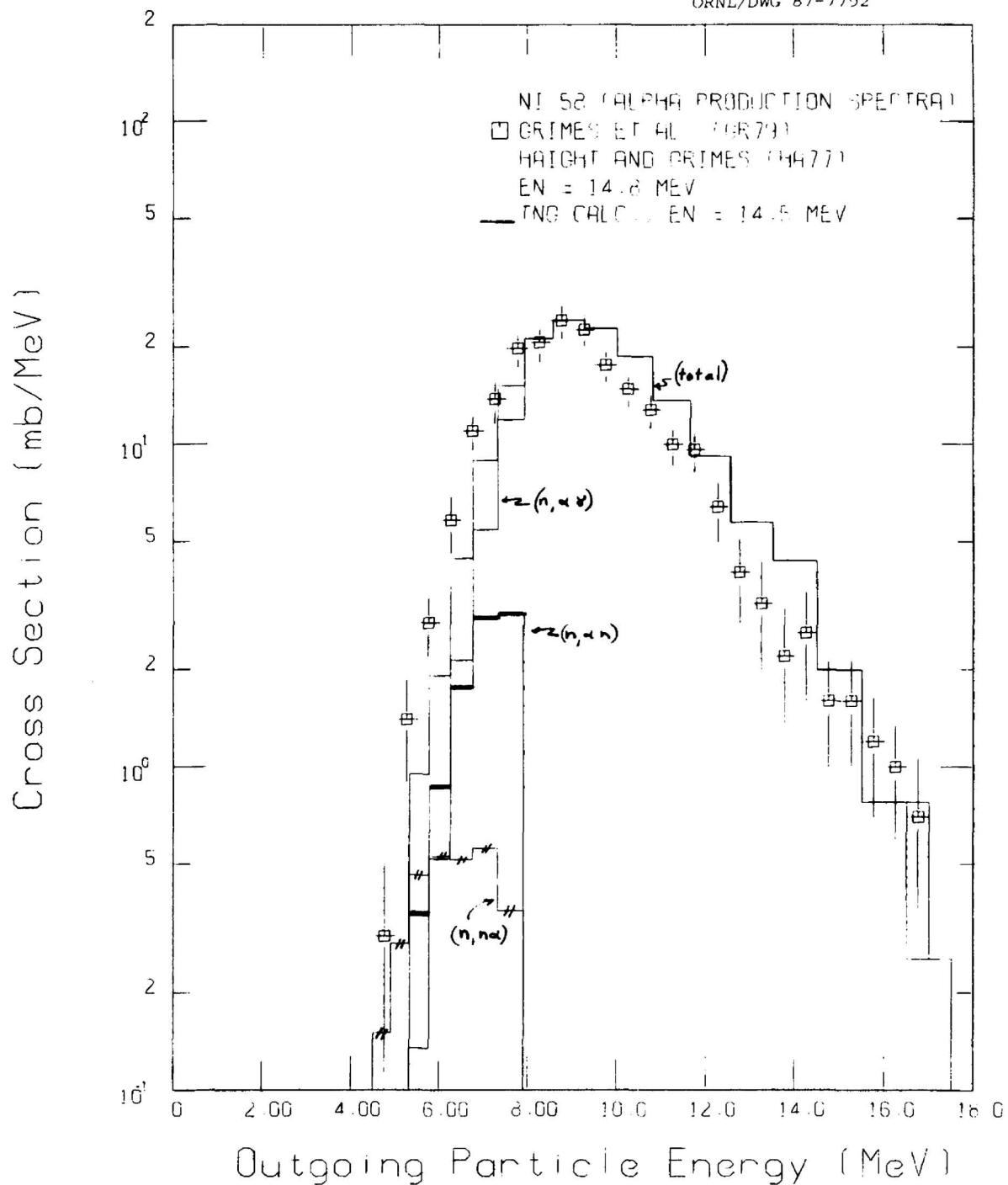


Fig. 56. Comparison of calculated and experimental alpha production spectra for ^{58}Ni . The measurement was taken at an incident energy of 14.8 MeV, the TNG calculation was for $E_n = 14.5$ MeV.

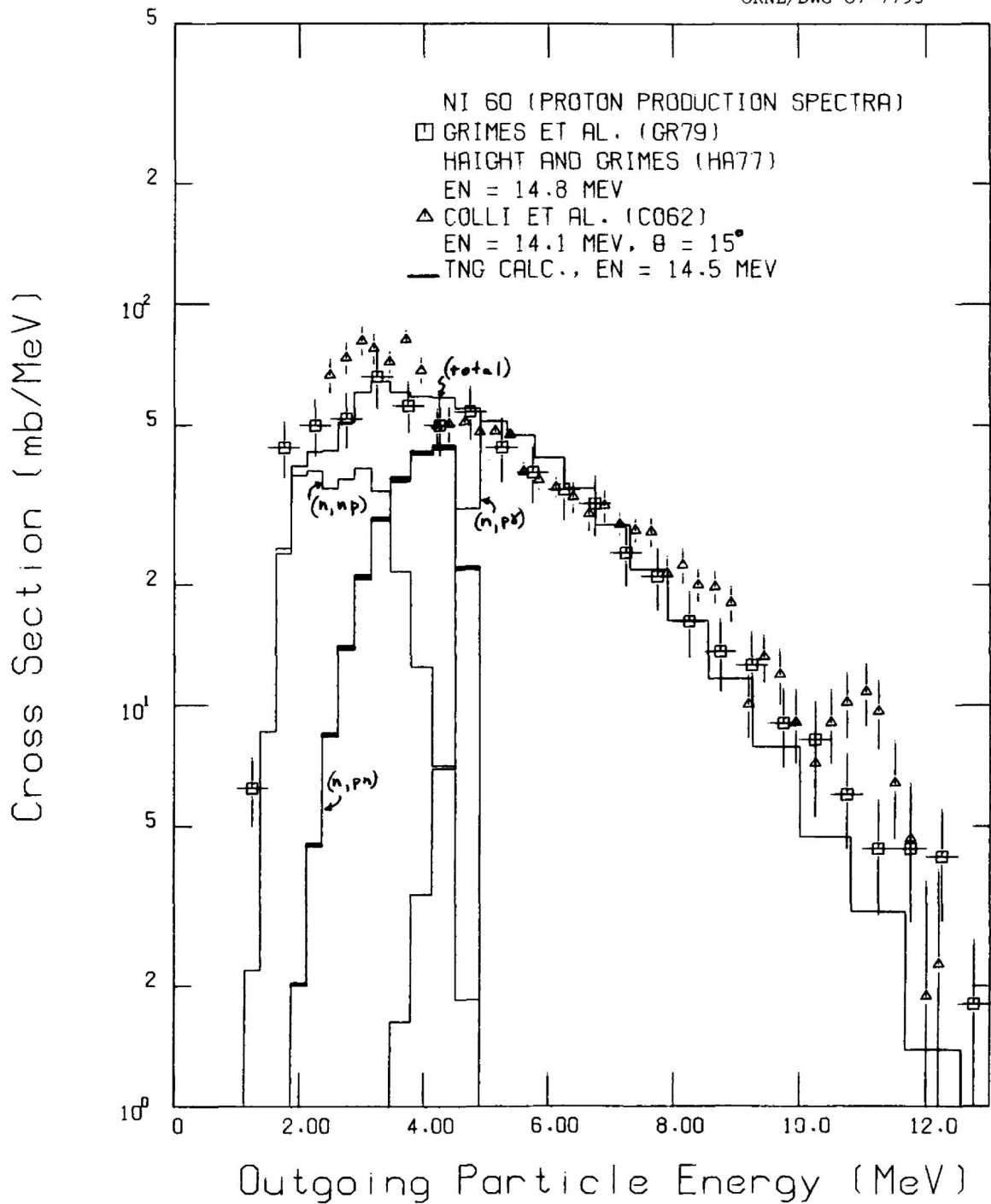


Fig. 57. Comparison of calculated and experimental proton production spectra for ^{66}Ni . The measurements were taken at incident energies of 14.8 and 14.1 MeV; the TNG calculation was for $E_n = 14.5$ MeV. The data of Grimes et al. (GR79, HA77) are angle integrated; the data of Colli et al. (CO62) were taken at 15° .

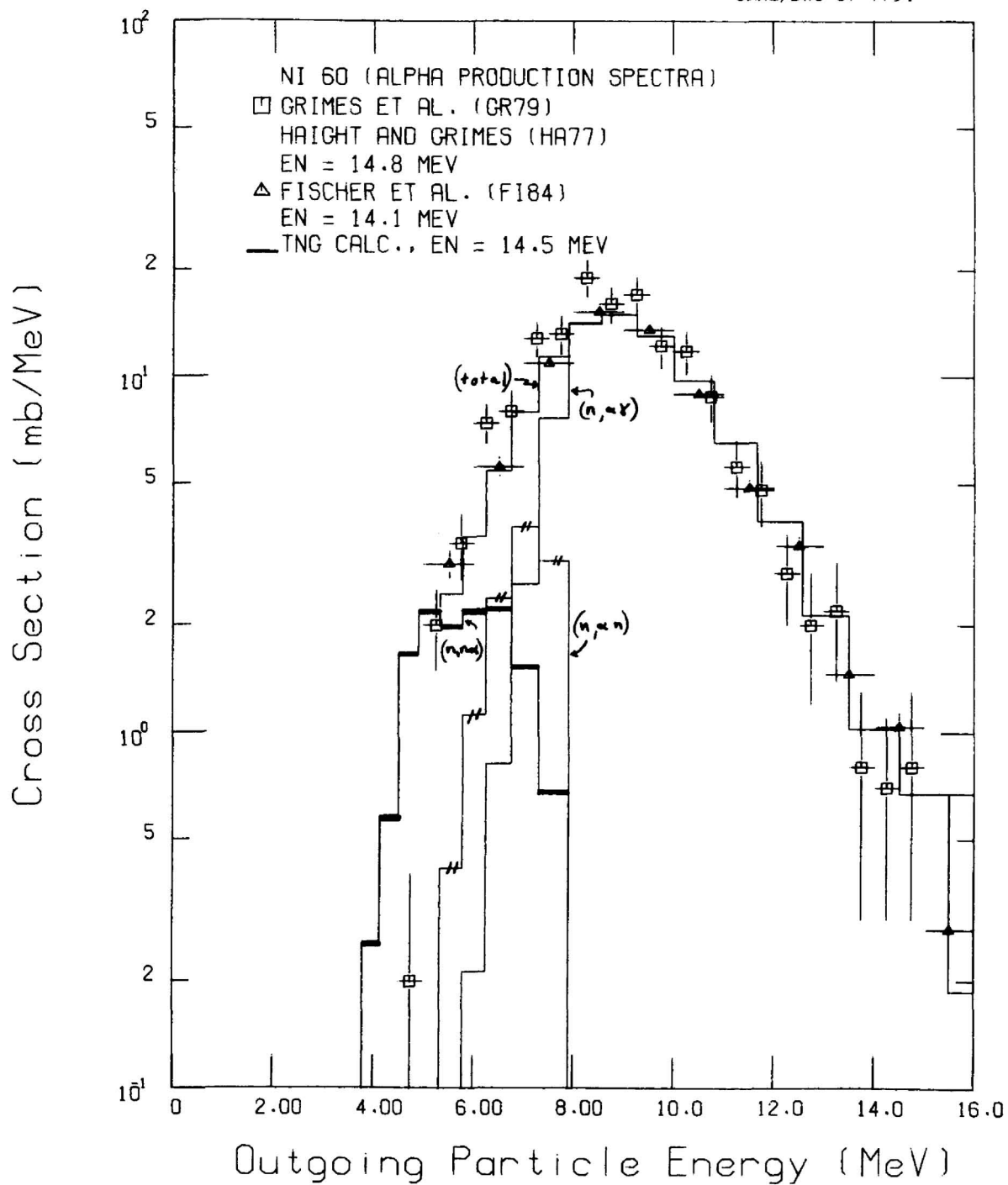
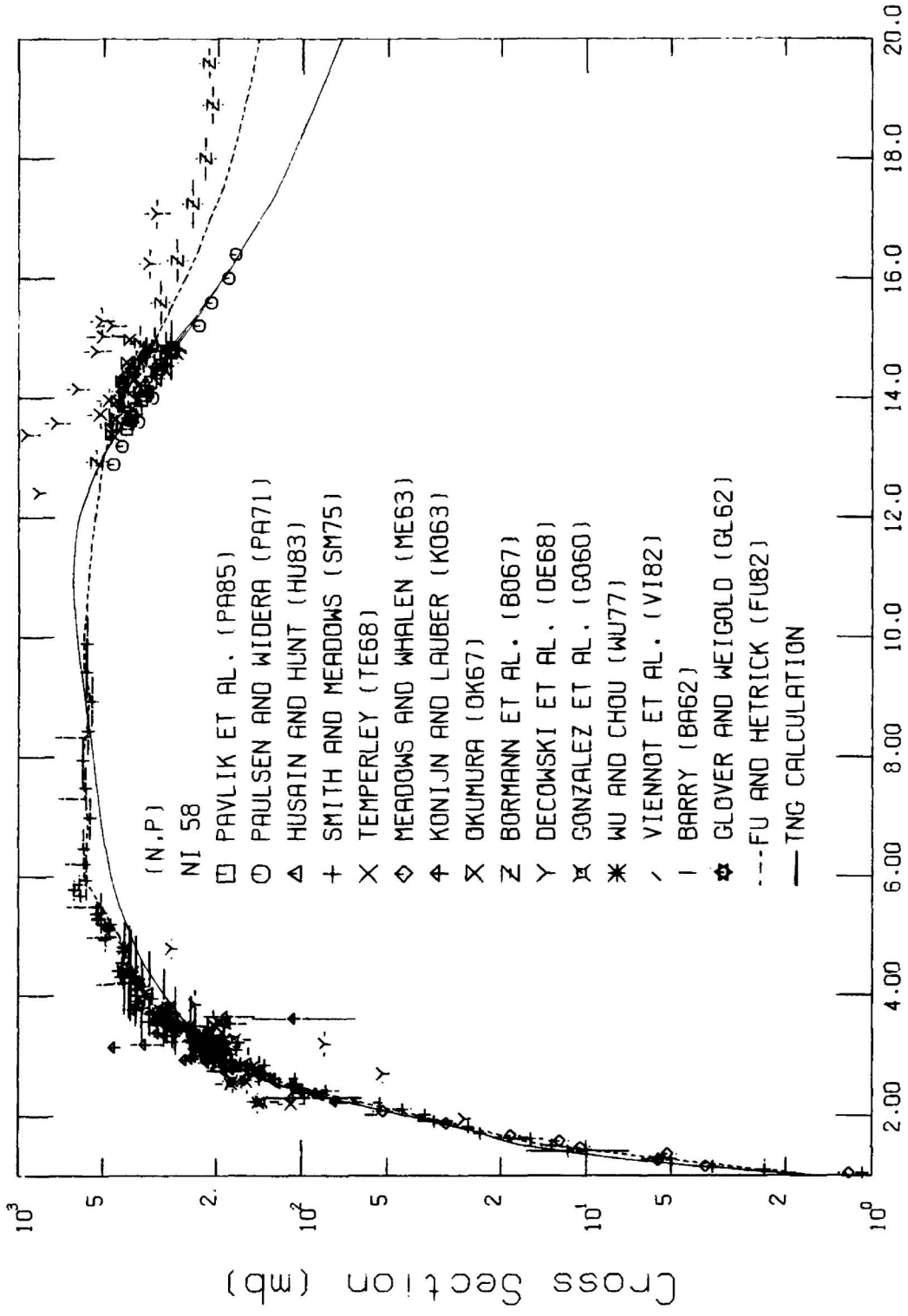


Fig. 58. Comparison of calculated and experimental alpha production spectra for ^{60}Ni . The measurements were taken at incident energies of 14.8 and 14.1 MeV and are angle integrated; the TNG calculation was for $E_n = 14.5$ MeV.

ORNL/DWG 87-7795



Incident Neutron Energy (MeV)

Fig. 59. Comparison of calculated and experimental ⁵⁸Ni(n,p) cross sections.

ORNL/DWG 87-7796

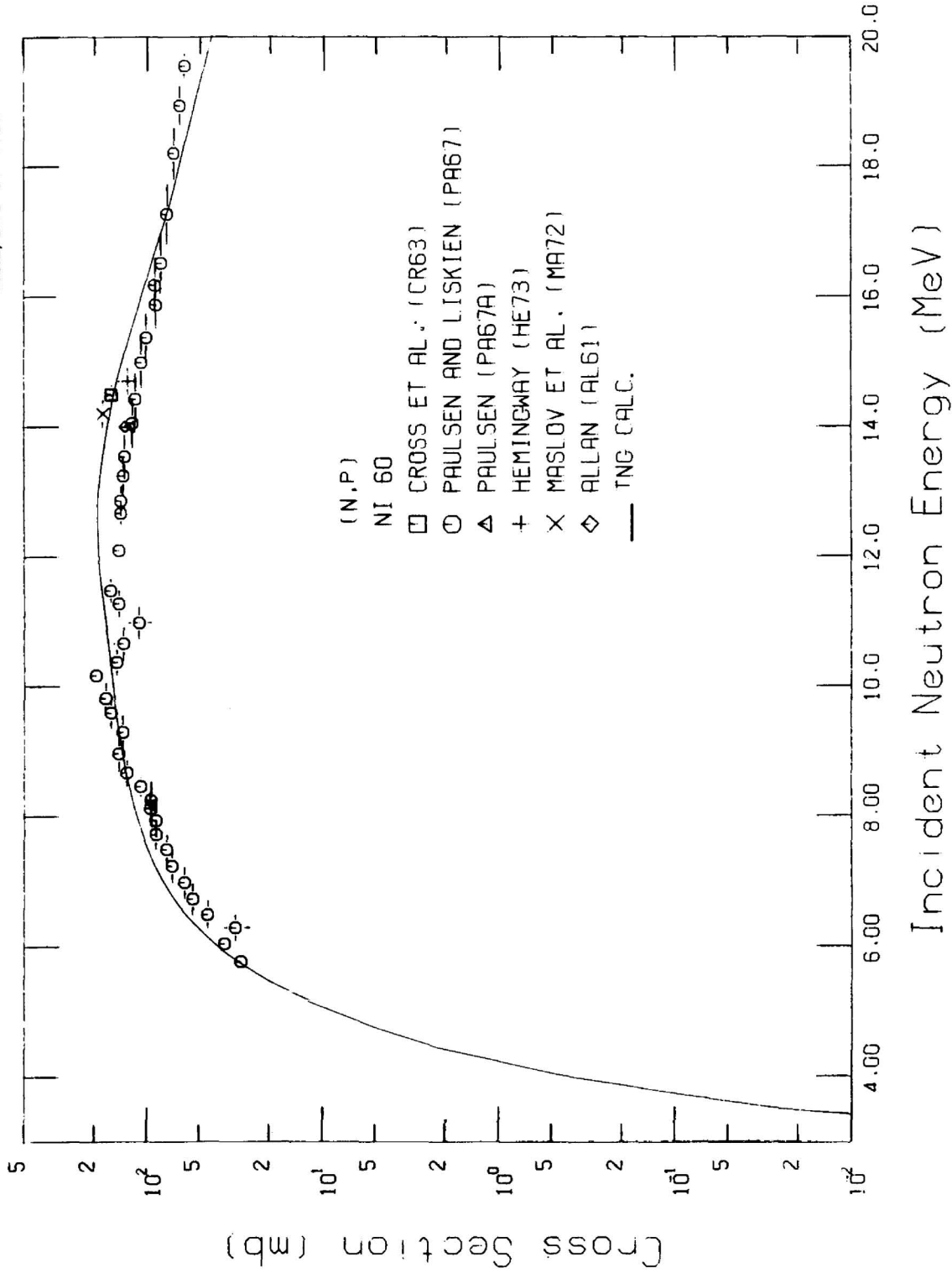


Fig. 60. Comparison of calculated and experimental $^{60}\text{Ni}(n,p)$ cross sections.

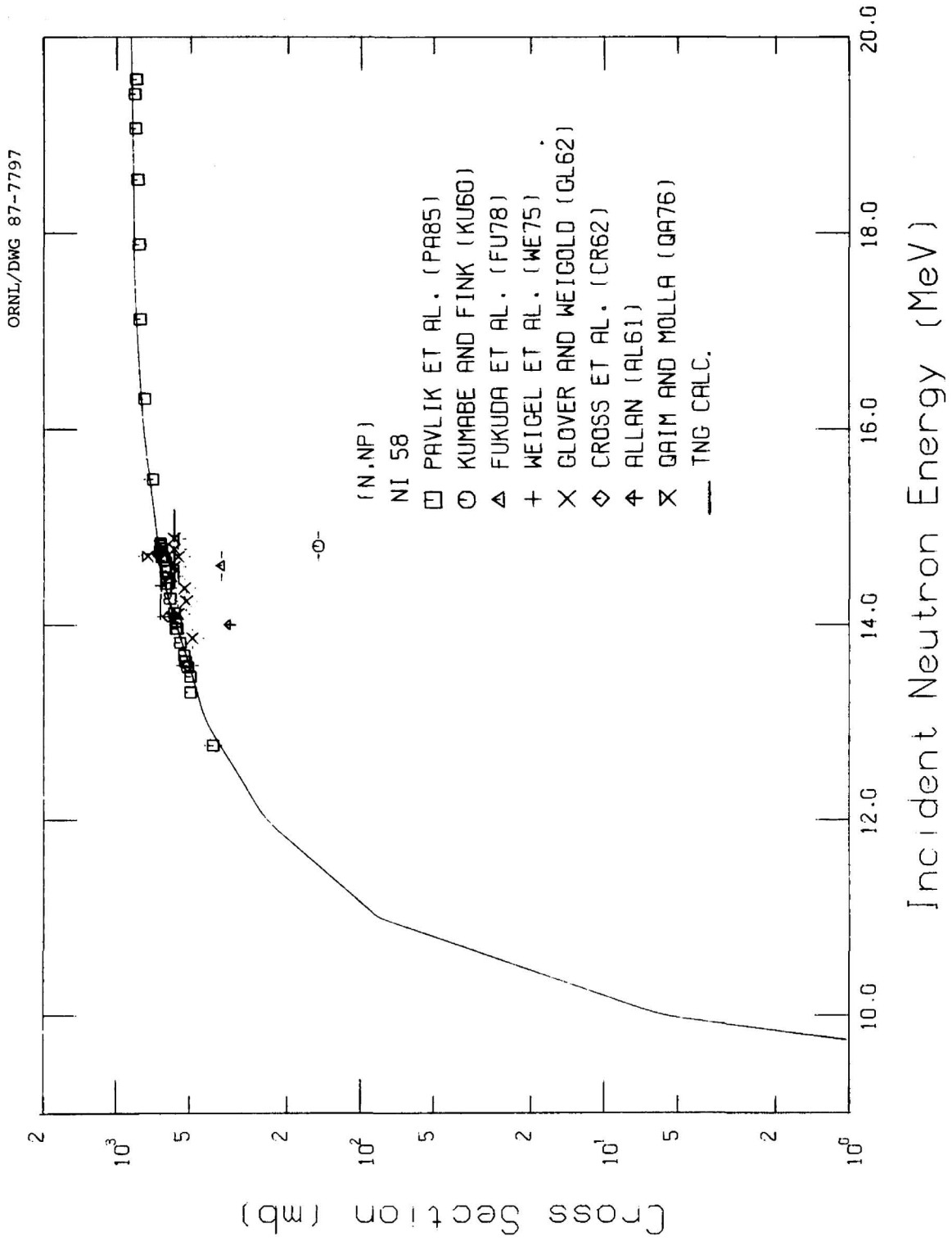


Fig. 61. Comparison of calculated and experimental $^{58}\text{Ni}(n,np) + (n,pn)$ cross sections.

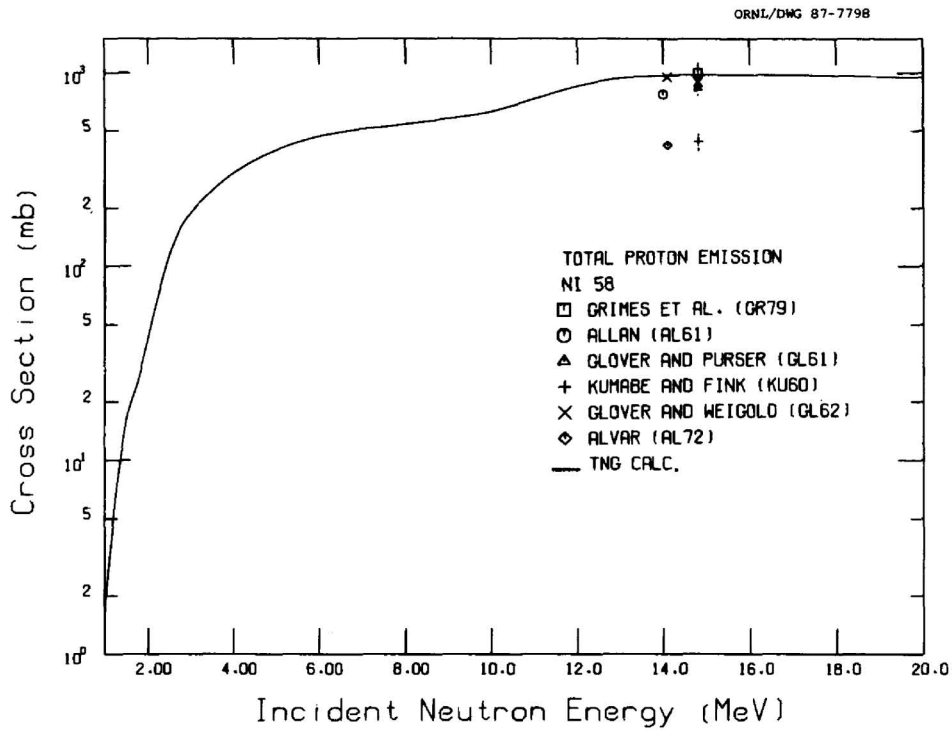


Fig. 62. Comparison of calculated and experimental cross sections for the total proton emission of ^{58}Ni . The $^{58}\text{Ni}(n,p)$ data from Fig. 59 for incident energies less than approximately 9.0 MeV could have been included in this figure.

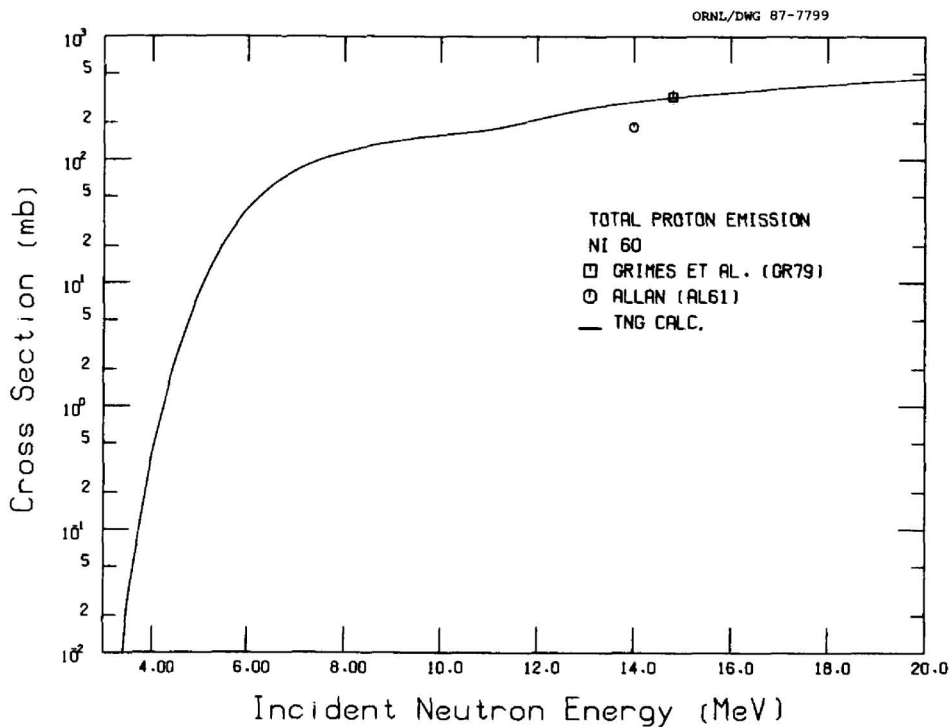


Fig. 63. Comparison of calculated and experimental cross sections for the total proton emission of ^{60}Ni . The $^{60}\text{Ni}(n,p)$ data from Fig. 60 for incident energies less than approximately 10.0 MeV could have been included in this figure.

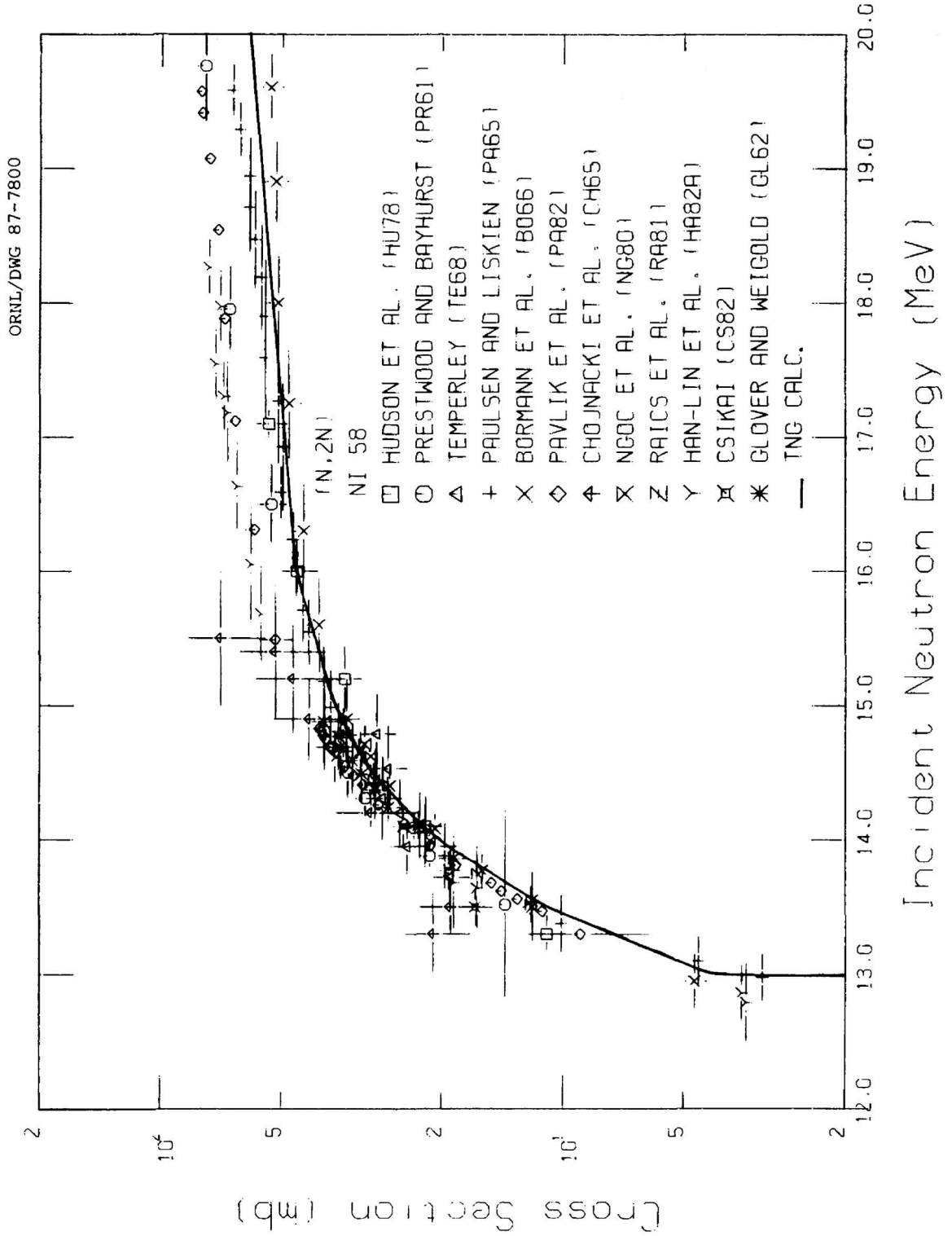


Fig. 64. Comparison of calculated and experimental $^{58}\text{Ni}(n,2n)$ cross sections.

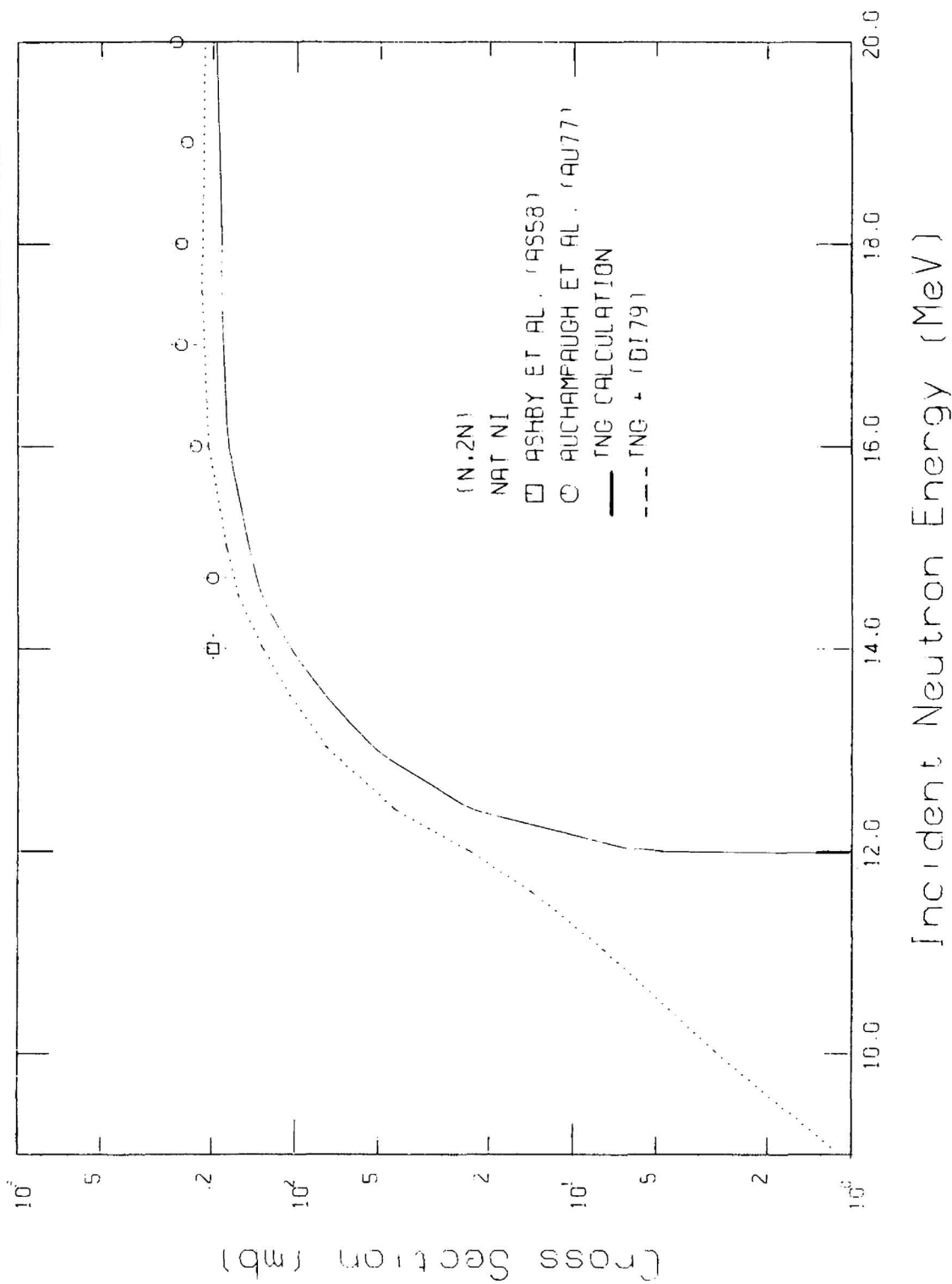


Fig. 65. Comparison of calculated and experimental $^{58}\text{Ni}(n,2n)$ cross sections. The solid line is the sum of the TNG calculations for $^{58}\text{Ni}(n,2n)$ and $^{60}\text{Ni}(n,2n)$ multiplied by 0.71 and 0.29 respectively. The dashed line is the sum of the TNG calculations for ^{58}Ni and ^{60}Ni added to the calculations of Divadeenam (DI79) for ^{61}Ni , ^{62}Ni , and ^{64}Ni (each were multiplied by its fractional natural abundance).

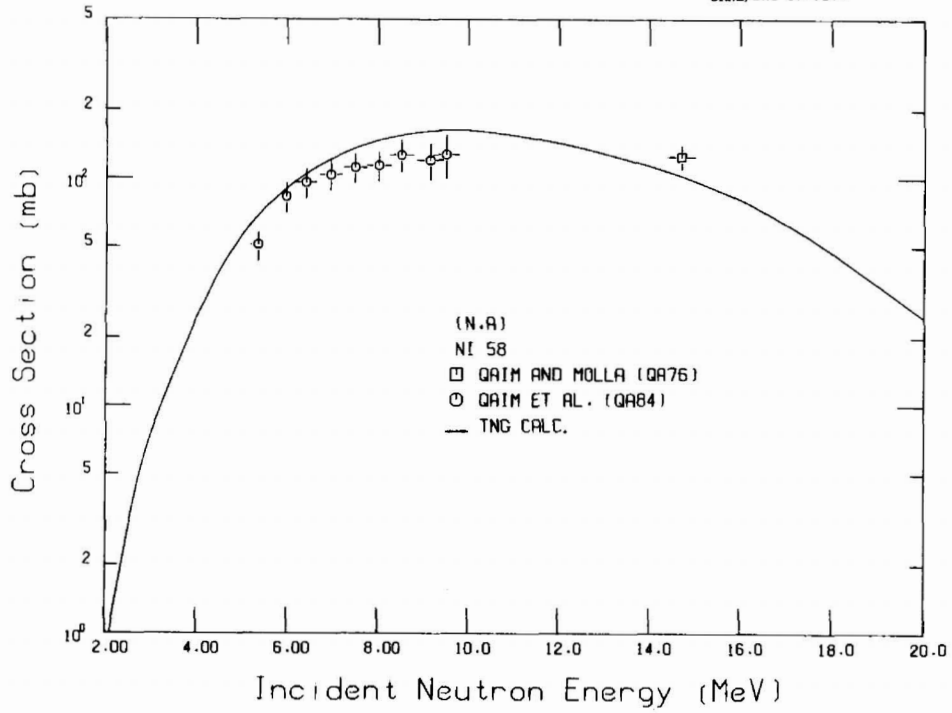


Fig. 66. Comparison of calculated and experimental $^{58}\text{Ni}(n,\alpha)$ cross sections.

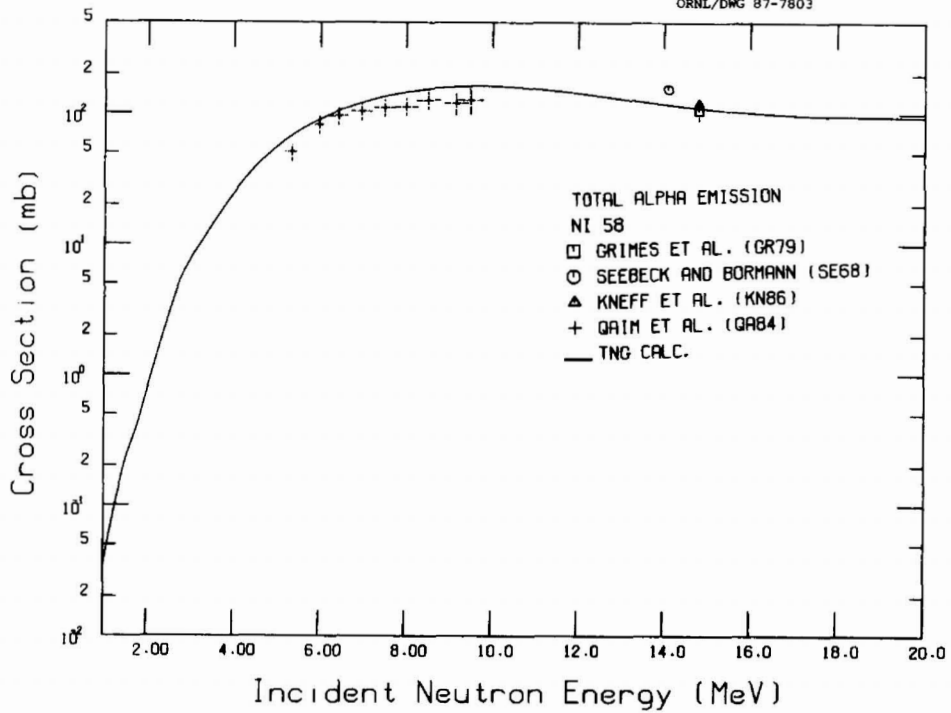


Fig. 67. Comparison of calculated and experimental cross sections for the total alpha emission of ^{58}Ni .

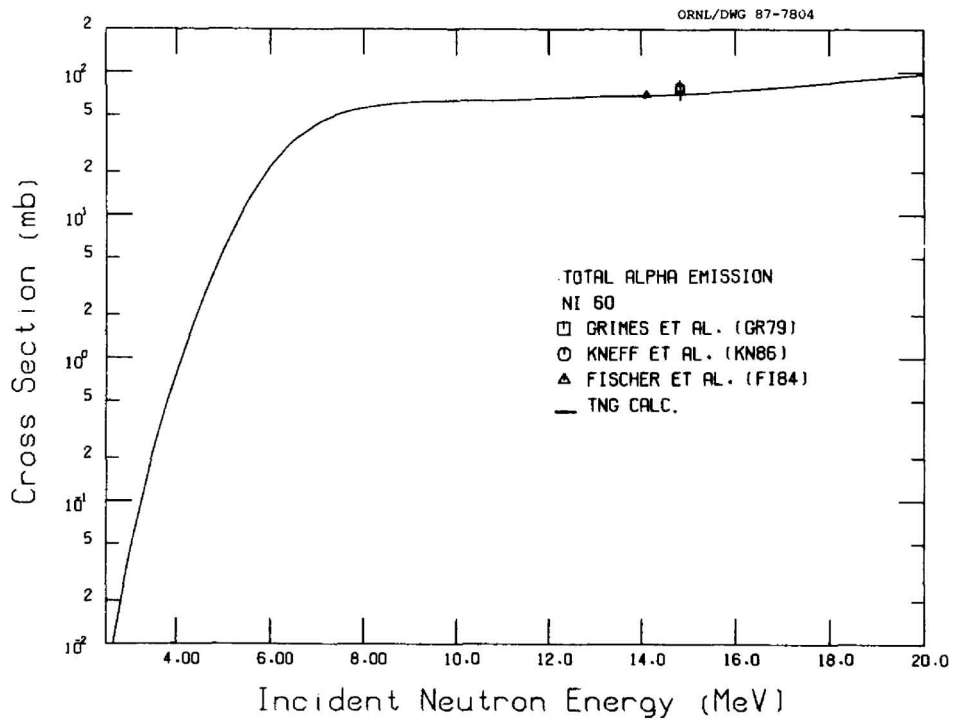


Fig. 68. Comparison of calculated and experimental cross sections for the total alpha emission of ^{60}Ni .

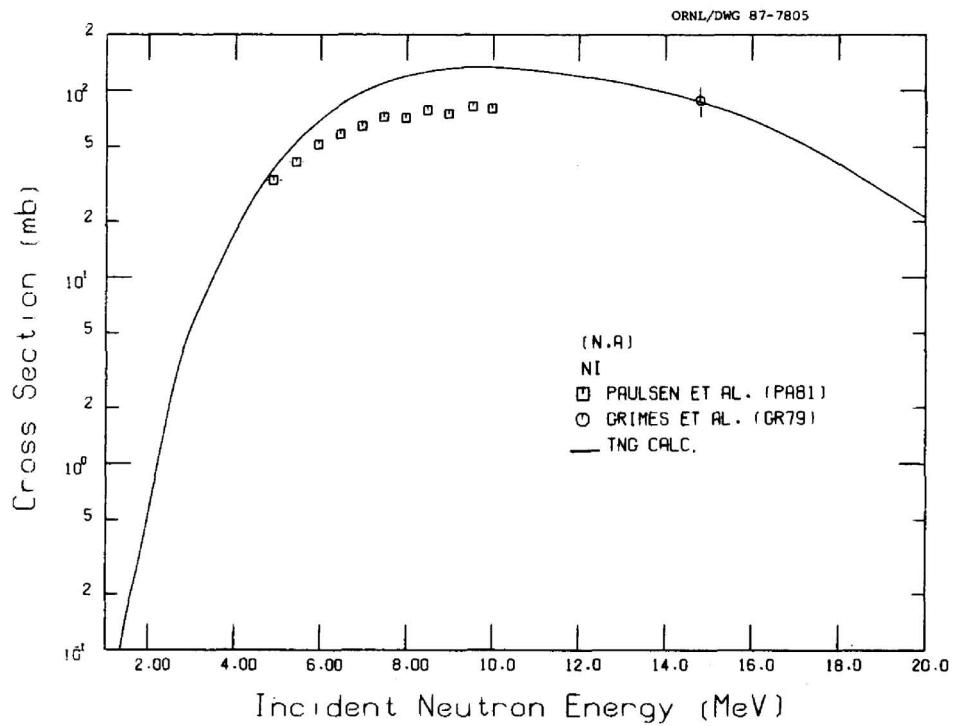


Fig. 69. Comparison of calculated and experimental $^{60}\text{Ni}(n,\alpha)$ cross sections.

The $^{58}\text{Ni}(n,\alpha)$ data and TNG calculations are shown in Fig. 66, and the total alpha emission results for ^{58}Ni and ^{60}Ni are presented in Figs. 67 and 68, respectively. The total alpha-emission calculations agree very well with the available data at 14.5 MeV incident energy, but the $^{58}\text{Ni}(n,\alpha)$ calculation is slightly larger than the data of Qaim et al. (1984) for incident energies less than 10.0 MeV. The TNG calculation for $^{58}\text{Ni}(n,\alpha)$ (multiplied by 0.71) is added to the calculation for $^{60}\text{Ni}(n,\alpha)$ (multiplied by 0.29) and compared to available natural nickel data in Fig. 69. In this figure, the data shown by Grimes et al. (GR79) is their total alpha-emission cross section minus the TNG calculation at 14.5 MeV for $(n,n\alpha) + (n,\alpha n)$. The TNG results in this figure are up to 75% larger than the data of Paulsen et al. (PA81) for incident energies less than 10.0 MeV. However, it should be noted that the data of Qaim et al. (QA84) for $^{58}\text{Ni}(n,\alpha)$ (see Fig. 66), if multiplied by the fractional natural abundance, is approximately 10% larger than the data of Paulsen et al. (PA81) for natural nickel.

The $^{58}\text{Ni}(n,p)$ reaction is one of several reactions used for dosimetry measurements, and we recently performed an evaluation in which this reaction was studied simultaneously with 12 other dosimetry reaction cross sections. This evaluation (FU82) is based on the generalized least-squares technique which includes the impacts of measured ratios and cross-reaction covariances. The $^{58}\text{Ni}(n,p)$ data of Smith and Meadows (SM75) were used in this work. The resultant values for the $^{58}\text{Ni}(n,p)$ differ from the TNG calculations shown in Fig. 59 (see the dashed line versus solid line), and thus, for evaluation purposes, the results of FU82 should be used. From the point of view of the present analysis, however, the TNG calculations have provided a reasonable characterization of the behavior of the binary and tertiary reaction cross sections over a wide range of incident neutron energies.

4.11 GAMMA-RAY EXCITATION FUNCTIONS

Excitation functions for six gamma rays of ^{58}Ni are shown in Figs. 70 through 75 and for nine gamma rays of ^{60}Ni are shown in Figs. 76 through 84. The TNG calculations are in fairly good agreement with the data measured by Larson (1985), Traiforos et al. (TR79) and Dickens et al. (DI73). The data of Voss et al. (VO75) are averaged in the figures and are consistently about 30% smaller than the TNG calculations. The cross sections measured by Nishimura et al. (NI65) are smaller than the calculation (see Fig. 70), as is the datum measured by Yamamoto et al. (YA78) at 15.0 MeV (see Fig. 76). The other measured data sets (BR64, TE75, BR71, JO69, GR74) are inconsistent in their agreement/disagreement with the TNG calculations from one excitation function to the next.

4.12 INTEGRATED YIELD OF SECONDARY GAMMA RAYS

The integrated yield of secondary gamma rays with $E_\gamma \geq 1.0$ MeV for the TNG calculations and measurements are shown in Figure 85. For clarity, the data of Dickens et al. (DI73) were plotted at the midpoints of the incident neutron energy bins. The calculated yields agree with the data of Drake et al. (DR78) and Shin et al. (SH80) reasonably well but are smaller than the data of Dickens et al. for incident energies greater than 5 MeV. However, see the discussion in the next section on the energy conservation constraint in the calculation.

4.13 GAMMA-RAY PRODUCTION CROSS SECTIONS AND SPECTRAL COMPARISONS

The calculated gamma-ray production cross sections are compared to data measured by Dickens et al. (DI73), Drake et al. (DR78), and Shin et al. (SH80) in Figs. 86 through 90. Although the measurements of Dickens et al., as well as the calculations by TNG, were made at numerous incident energies, comparisons are shown only for energies of 5.5, 9.5, and 14.5 MeV. In each figure, the calculated secondary spectra were smeared by a Gaussian function corresponding to the resolution of the detector for the data of Dickens et al. (DI73).

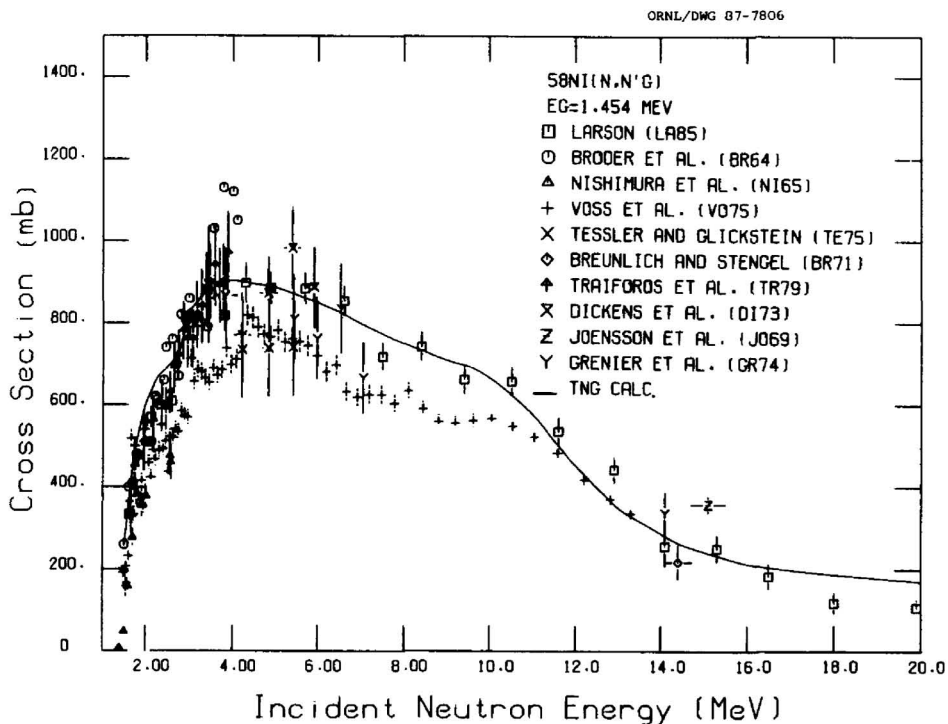


Fig. 70. Comparison of calculated and experimental data of the excitation function for the $E_\gamma = 1.454$ -MeV transition following $^{58}\text{Ni}(n,n'\gamma)$.

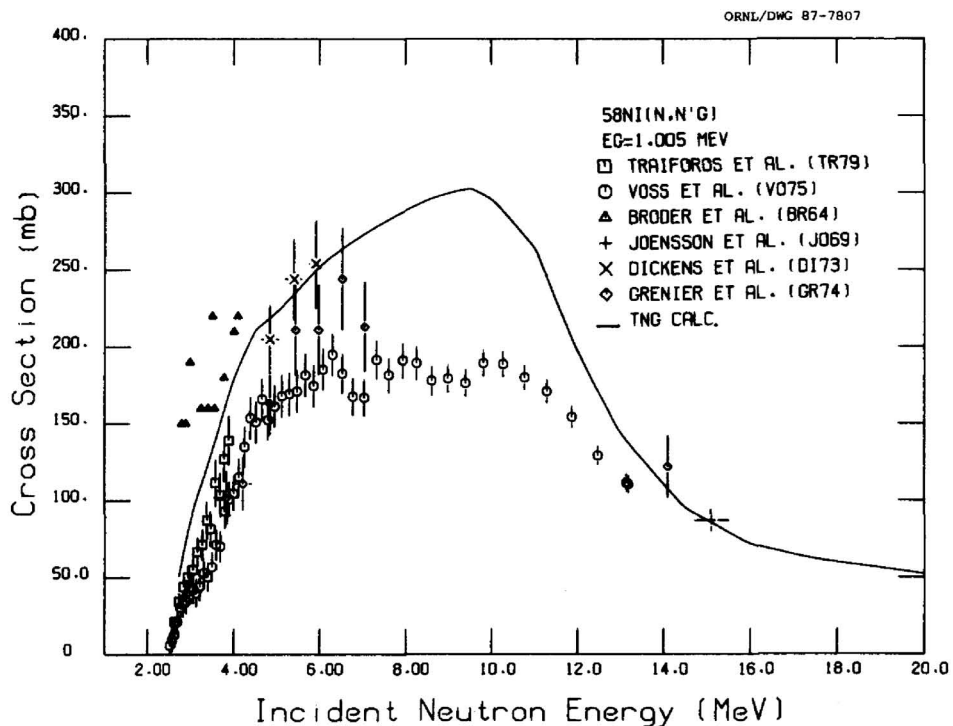


Fig. 71. Comparison of calculated and experimental data of the excitation function for the $E_\gamma = 1.005$ -MeV transition following $^{58}\text{Ni}(n,n'\gamma)$.

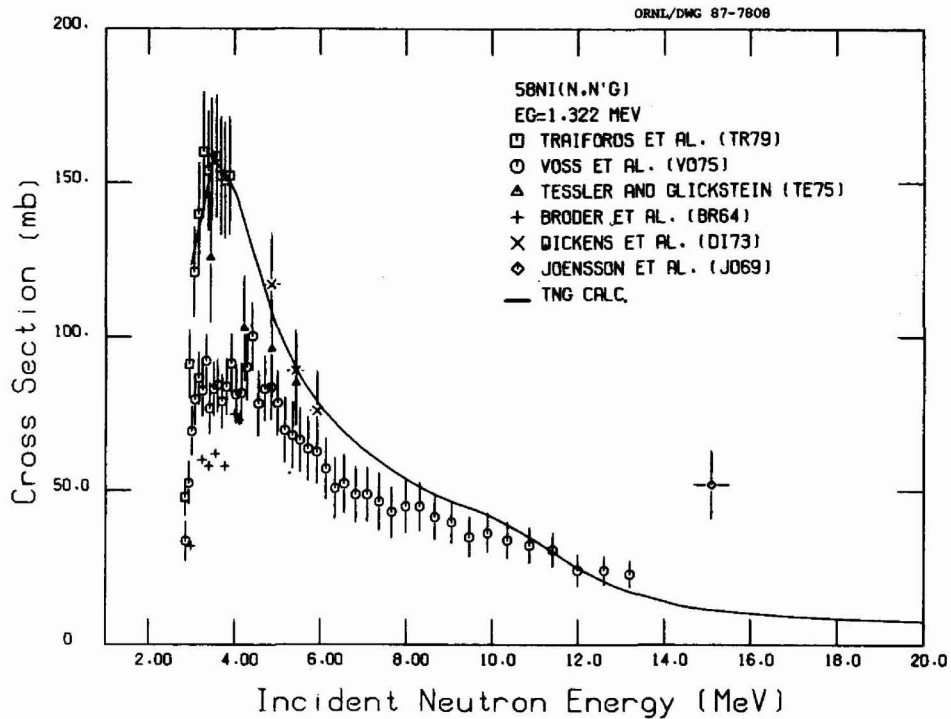


Fig. 72. Comparison of calculated and experimental data of the excitation function for the $E_\gamma = 1.322$ -MeV transition following $^{58}\text{Ni}(n,n'\gamma)$.

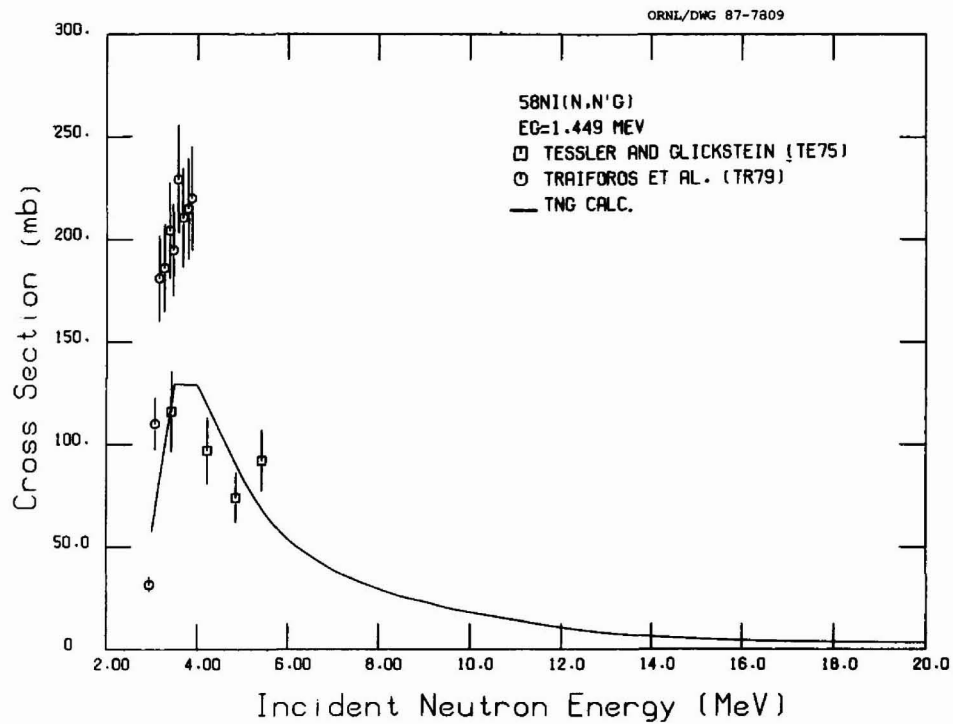


Fig. 73. Comparison of calculated and experimental data of the excitation function for the $E_\gamma = 1.449$ -MeV transition following $^{58}\text{Ni}(n,n'\gamma)$.

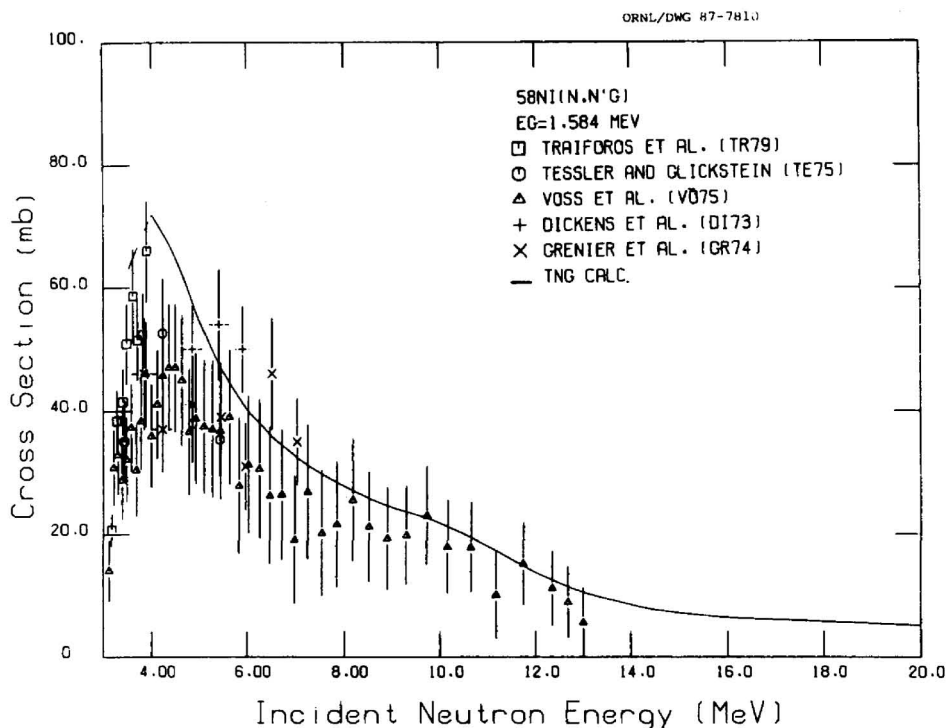


Fig. 74. Comparison of calculated and experimental data of the excitation function for the $E_\gamma = 1.584$ -MeV transition following $^{58}\text{Ni}(n,n'\gamma)$.

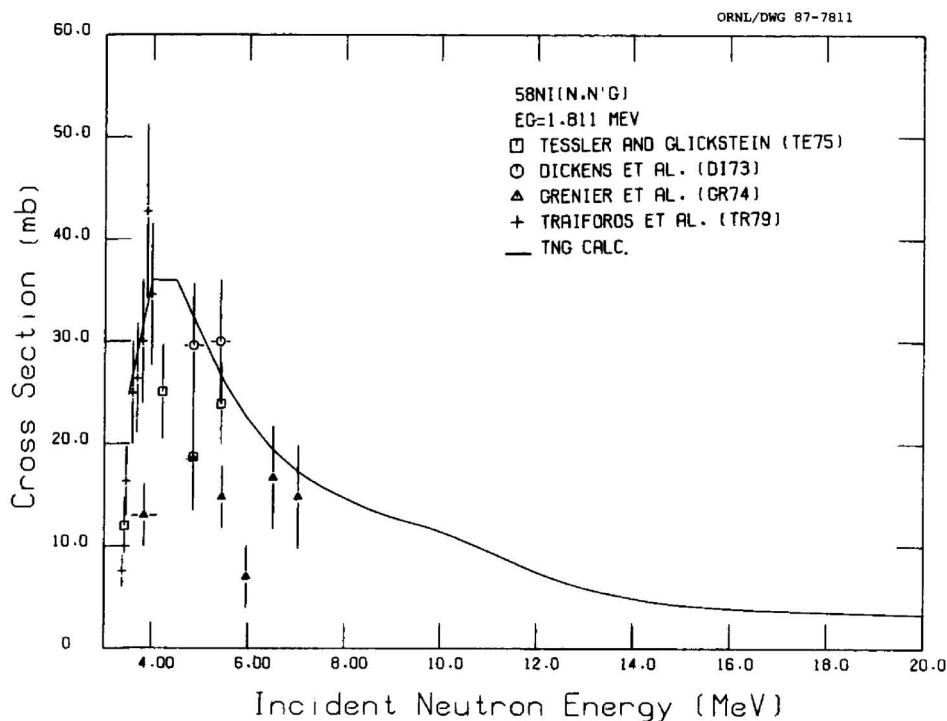


Fig. 75. Comparison of calculated and experimental data of the excitation function for the $E_\gamma = 1.811$ -MeV transition following $^{58}\text{Ni}(n,n'\gamma)$.

ORNL/DWG 87-7812

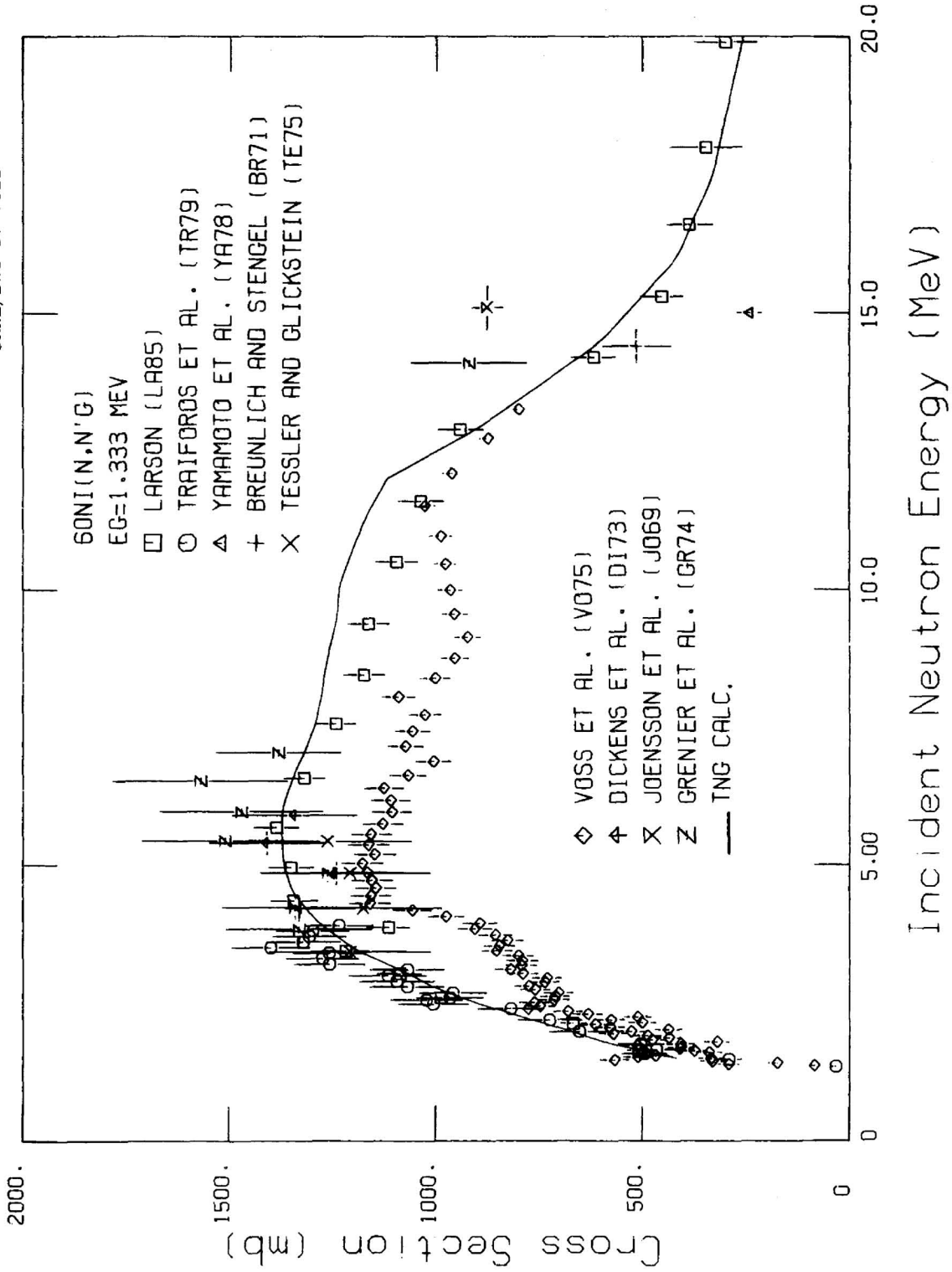


Fig. 76. Comparison of calculated and experimental data of the excitation function for the $E_{\gamma} = 1.333$ -MeV transition following ${}^{60}\text{Ni}(n,n'\gamma)$.

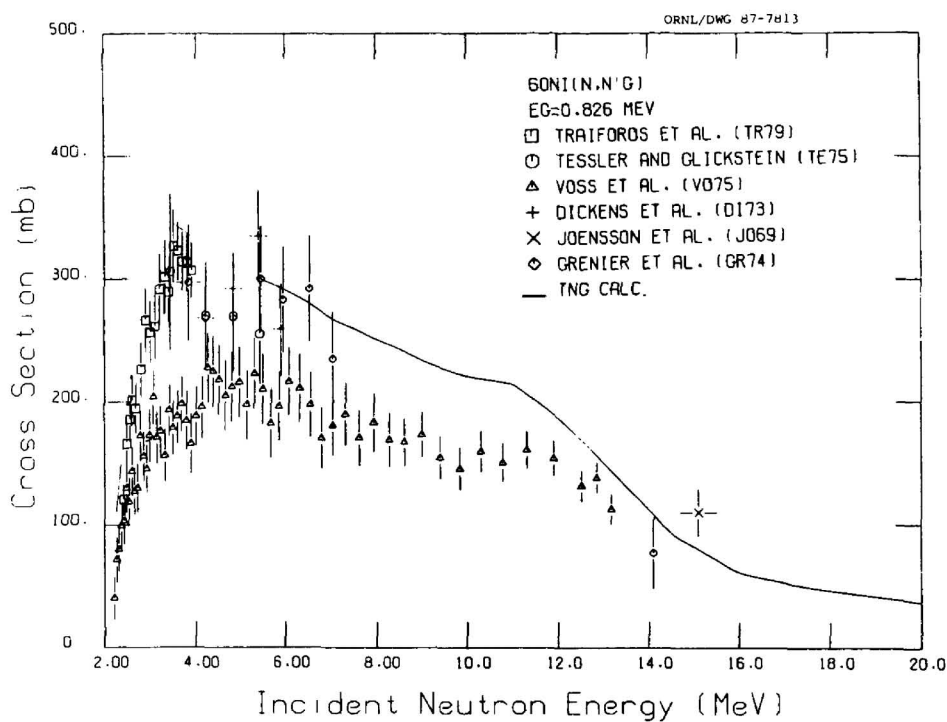


Fig. 77. Comparison of calculated and experimental data of the excitation function for the $E_{\gamma} = 0.826\text{-MeV}$ transition following ${}^{60}\text{Ni}(n,n'\gamma)$.

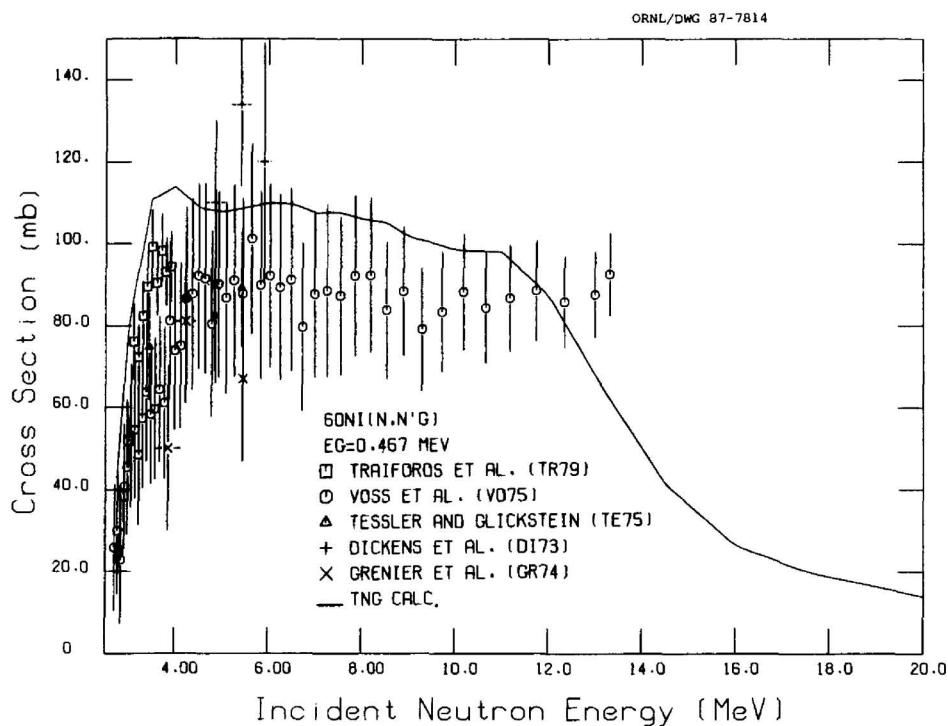


Fig. 78. Comparison of calculated and experimental data of the excitation function for the $E_{\gamma} = 0.467\text{-MeV}$ transition following ${}^{60}\text{Ni}(n,n'\gamma)$.

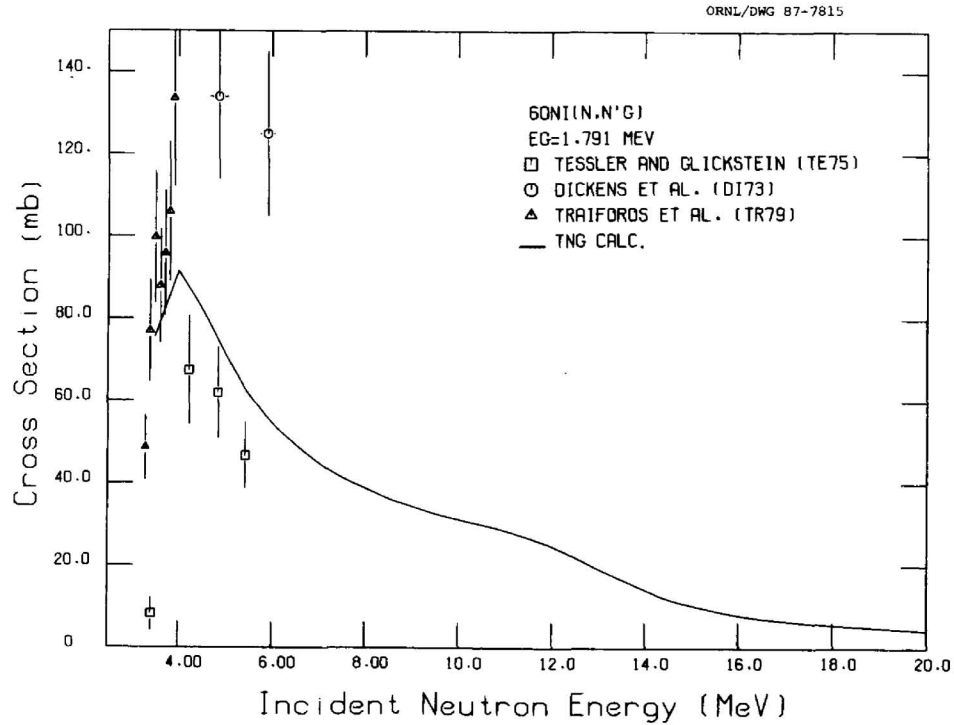


Fig. 79. Comparison of calculated and experimental data of the excitation function for the $E_\gamma = 1.791$ -MeV transition following $^{60}\text{Ni}(n,n'\gamma)$.

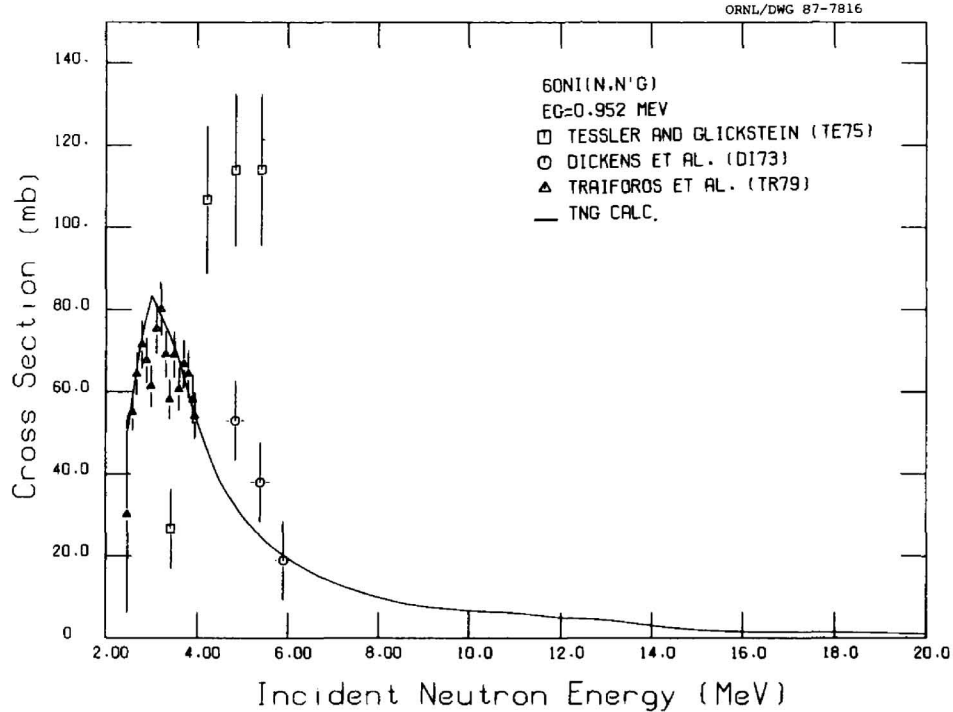


Fig. 80. Comparison of calculated and experimental data of the excitation function for the $E_\gamma = 0.952$ -MeV transition following $^{60}\text{Ni}(n,n'\gamma)$.

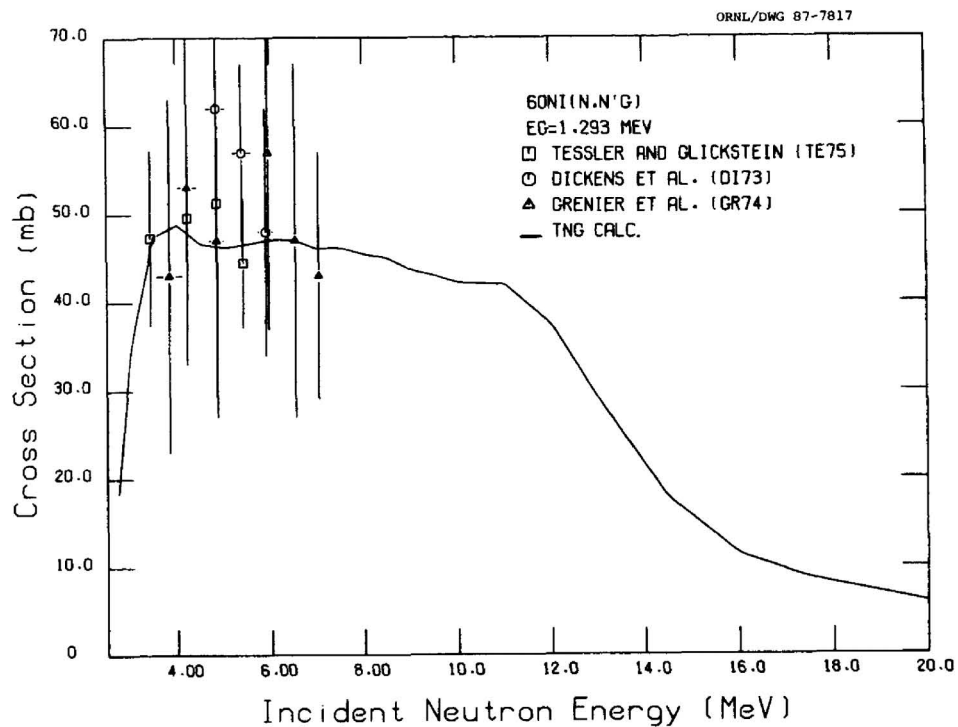


Fig. 81. Comparison of calculated and experimental data of the excitation function for the $E_{\gamma} = 1.293\text{-MeV}$ transition following $^{60}\text{Ni}(n,n'\gamma)$.

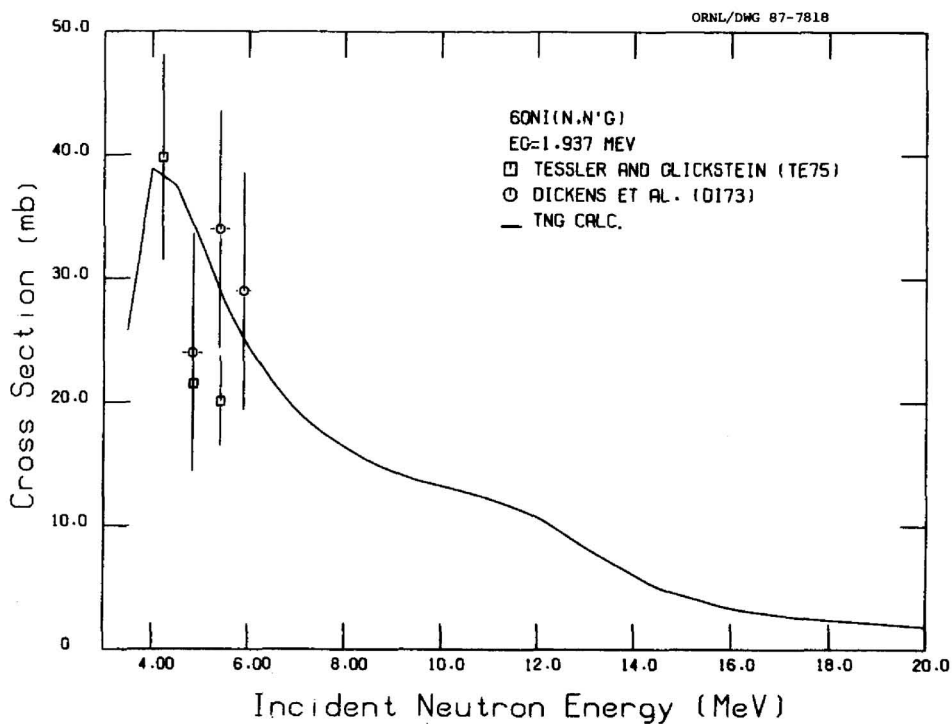


Fig. 82. Comparison of calculated and experimental data of the excitation function for the $E_{\gamma} = 1.937\text{-MeV}$ transition following $^{60}\text{Ni}(n,n'\gamma)$.

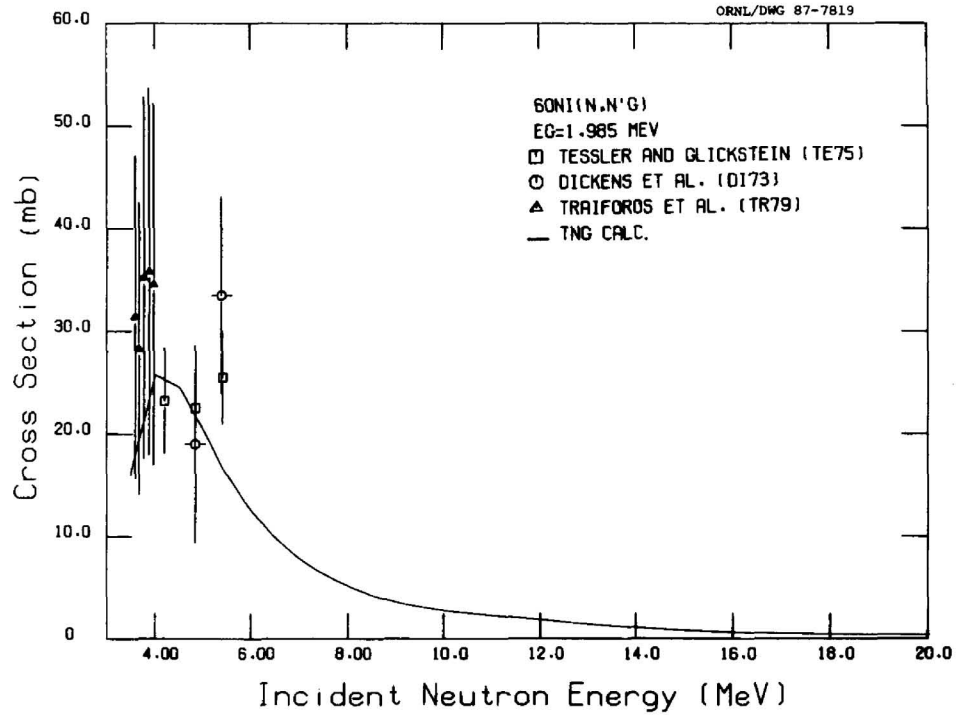


Fig. 83. Comparison of calculated and experimental data of the excitation function for the $E_{\gamma} = 1.985\text{-MeV}$ transition following ${}^{60}\text{Ni}(n,n'\gamma)$.

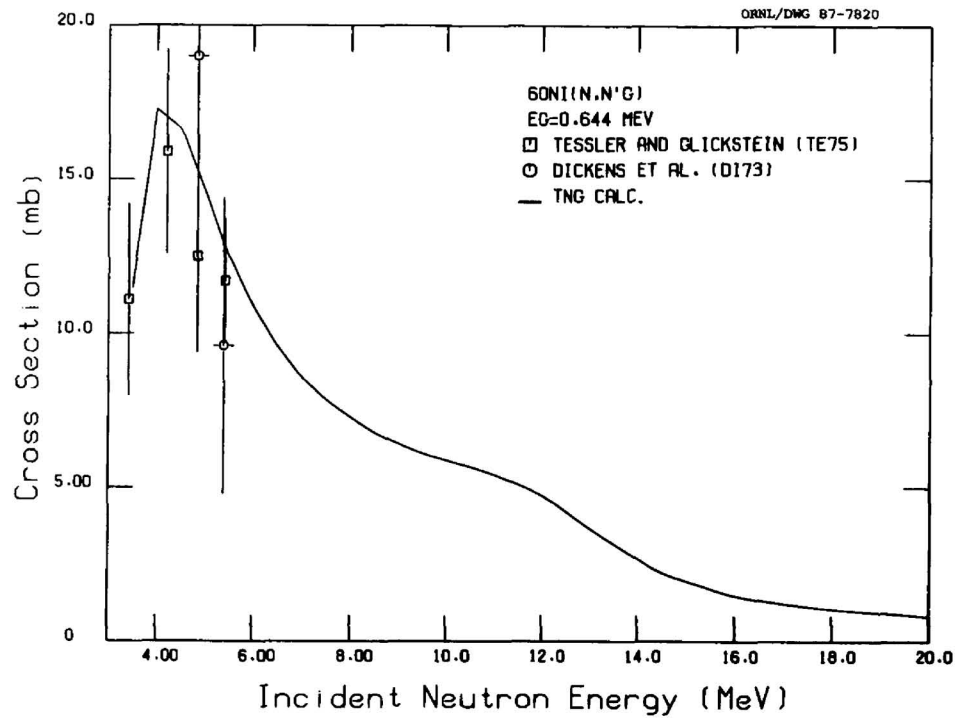


Fig. 84. Comparison of calculated and experimental data of the excitation function for the $E_{\gamma} = 0.644\text{-MeV}$ transition following ${}^{60}\text{Ni}(n,n'\gamma)$.

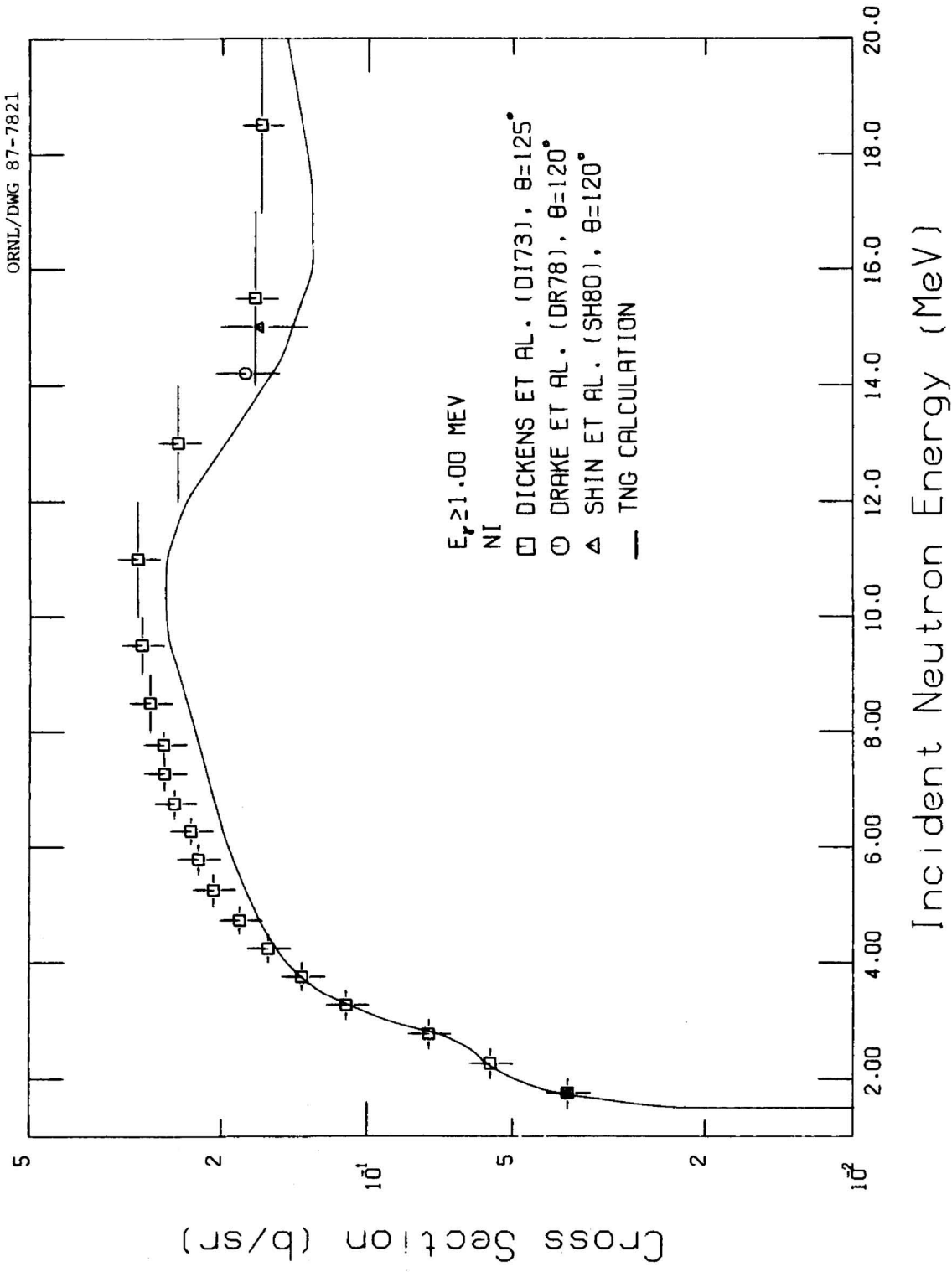


Fig. 85. Integrated yield of secondary gamma rays with $E_\gamma > 1.00$ MeV as a function of incident neutron energy. Gamma-ray scattering angles θ , are given in the legend.

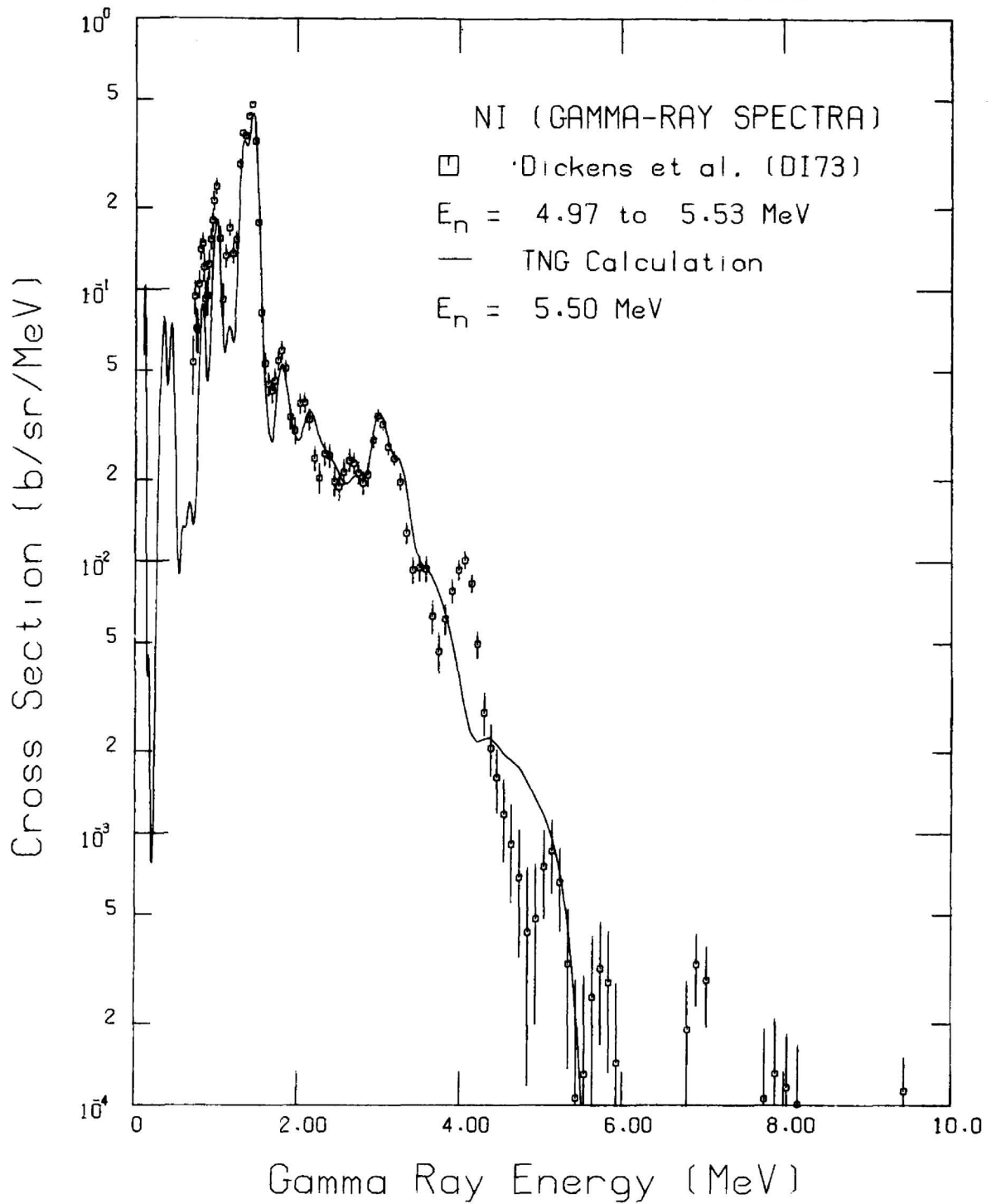


Fig. 86. Secondary gamma-ray spectra versus gamma-ray energy from the TNG calculation (incident energy $E_n = 5.5$ MeV) compared with the data of Dickens et al. (DI73).

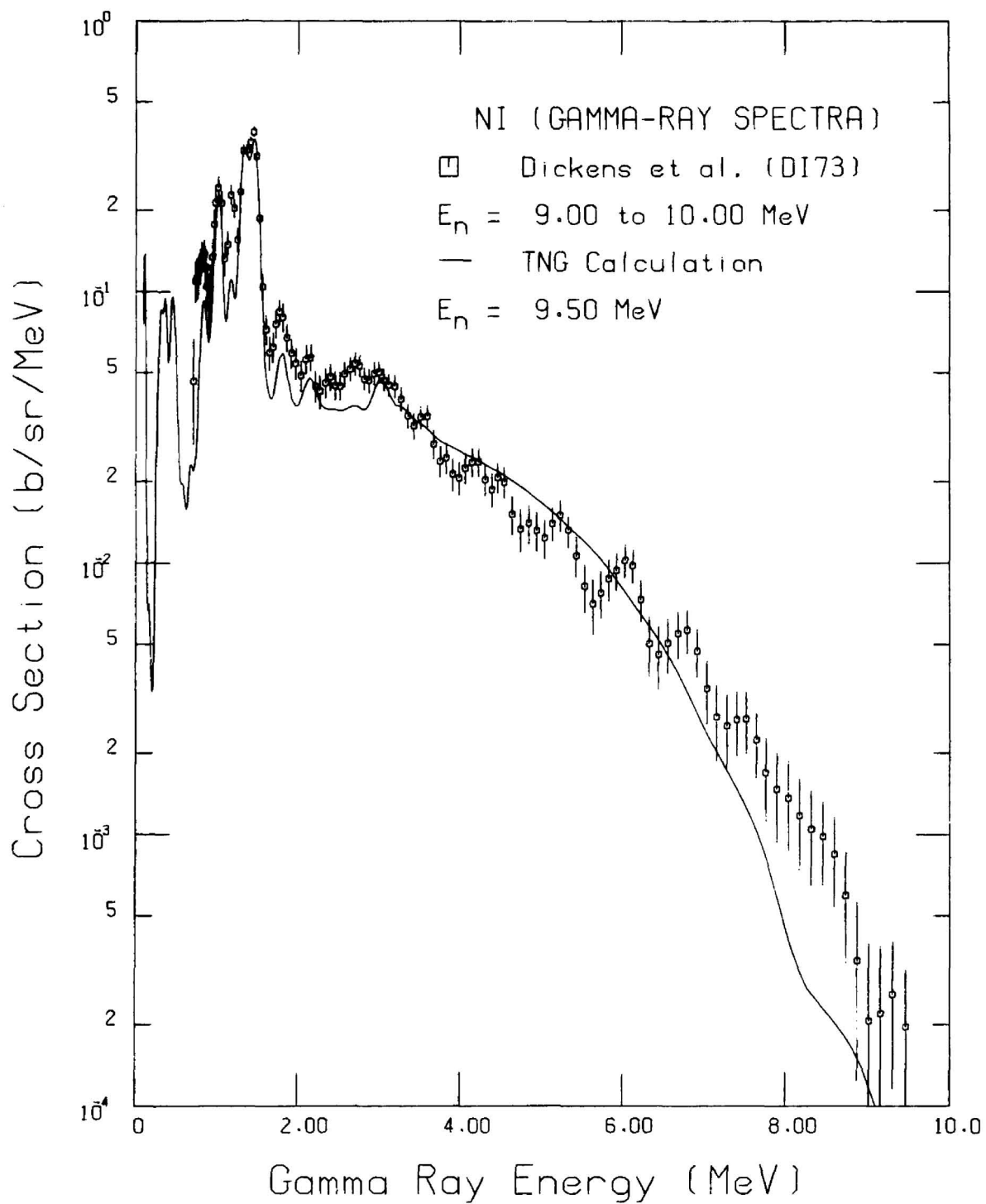


Fig. 87. Secondary gamma-ray spectra versus gamma-ray energy from the TNG calculation (incident energy $E_n = 9.5$ MeV) compared with the data of Dickens et al. (DI73).

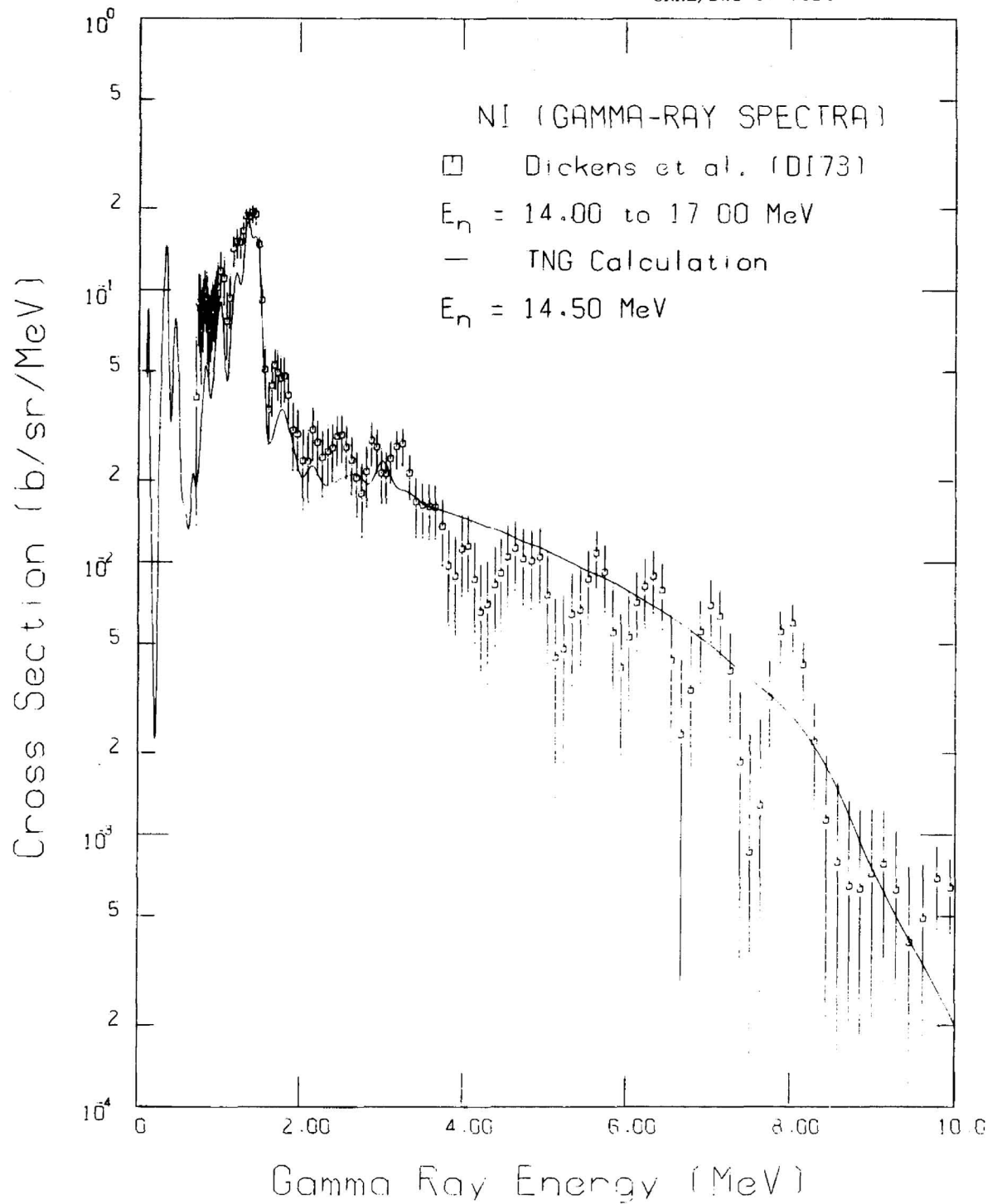


Fig. 88. Secondary gamma-ray spectra versus gamma-ray energy from the TNG calculation (incident energy $E_n = 14.5$ MeV) compared with the data of Dickens et al. (DI73).

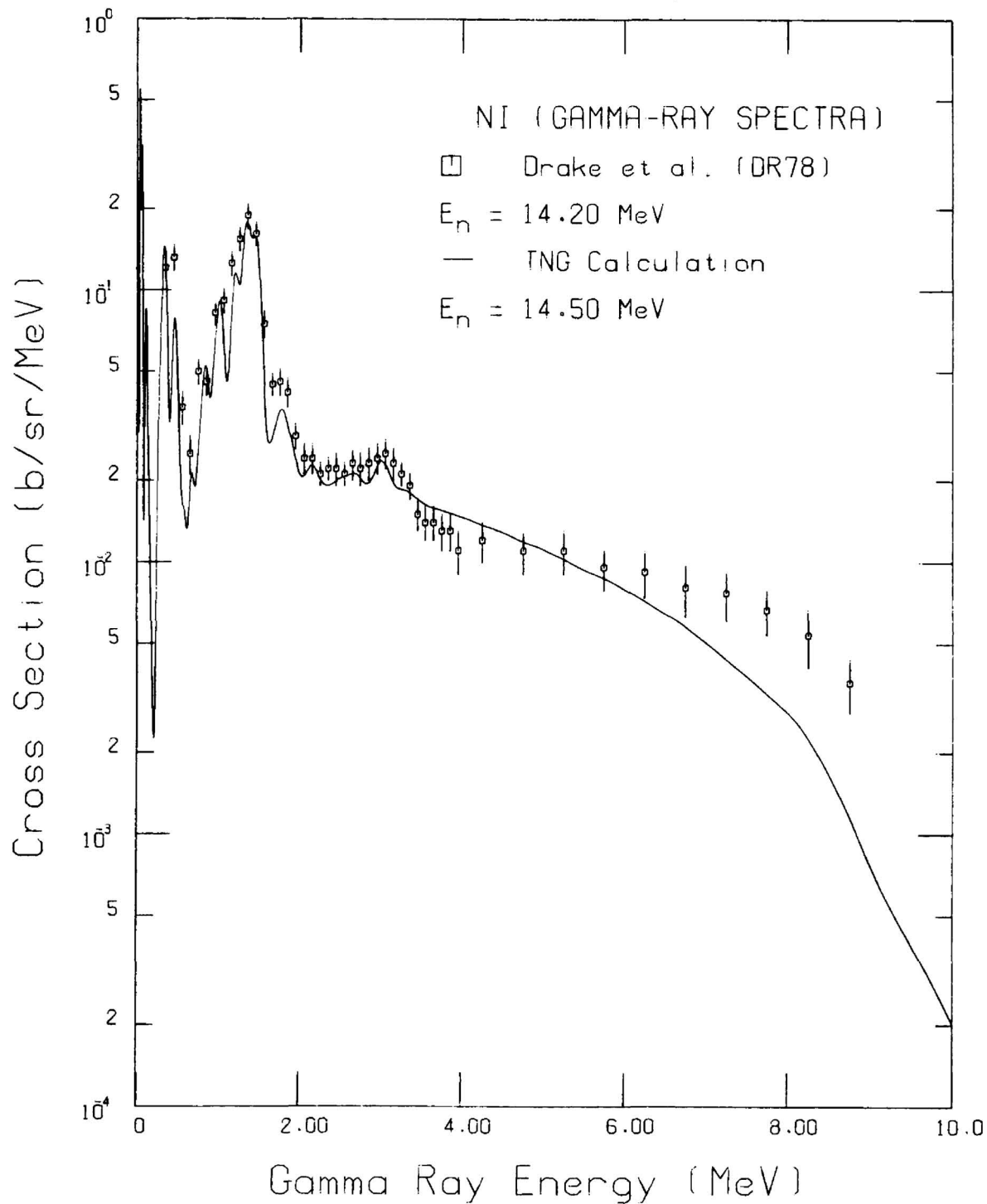


Fig. 89. Secondary gamma-ray spectra versus gamma-ray energy from the TNG calculation (incident energy $E_n = 14.5$ MeV) compared with the data of Drake et al. (DR78).

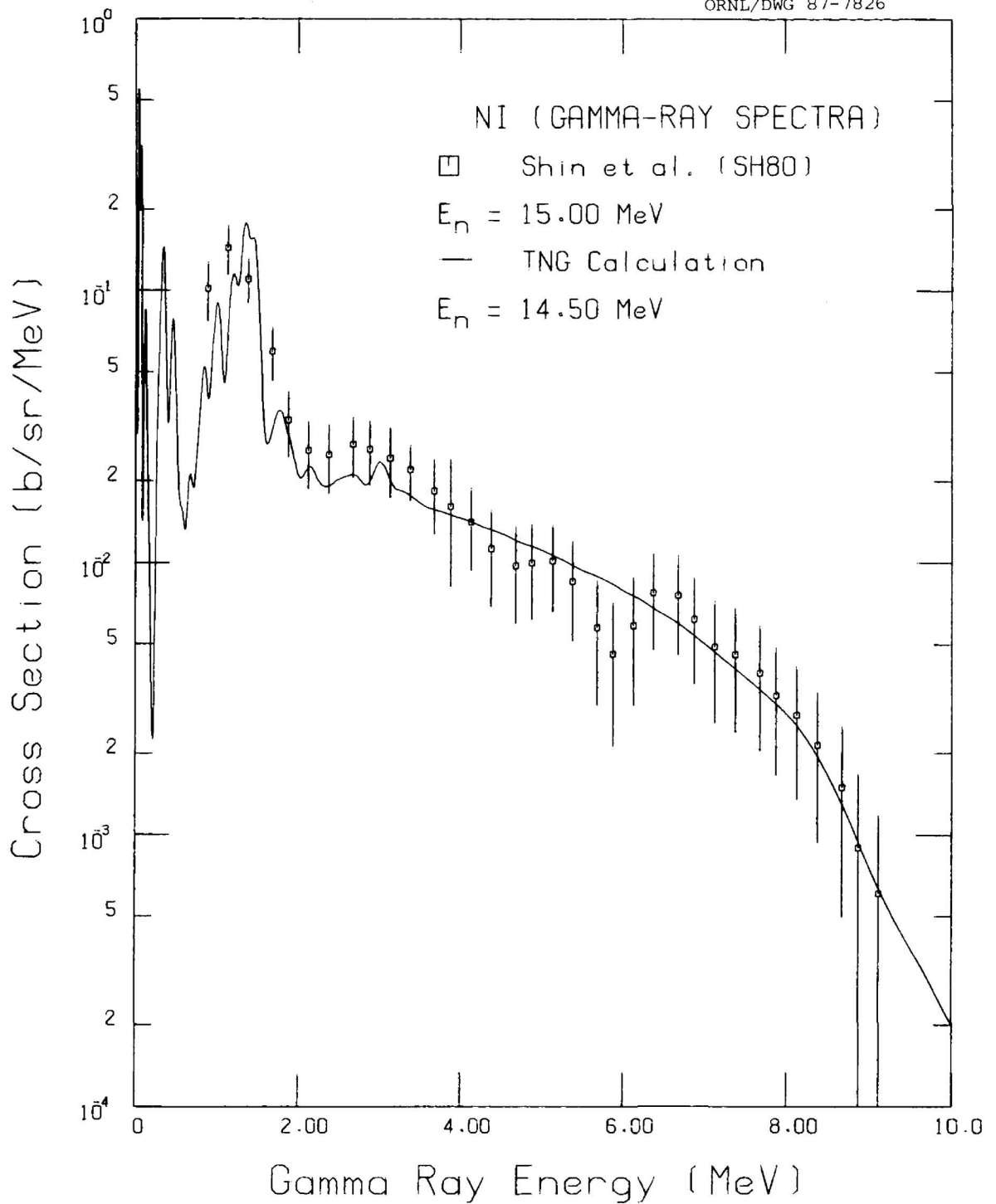


Fig. 90. Secondary gamma-ray spectra versus gamma-ray energy from the TNG calculation (incident energy $E_n = 14.5$ MeV) compared with the data of Shin et al. (SH80).

Before looking at the comparisons between the computed gamma-ray production spectra and measurements cited above, we should first discuss the energy-conservation constraint imposed in the calculation. In each reaction, the sum of the energies of the outgoing particles (including the recoiled heavy particle) and gamma rays equals the incident neutron energy plus the Q value of the reaction. Since there is good overall agreement between calculation and experiment in various partial reaction cross sections and particle-production spectra, the computed gamma-ray production spectra can be regarded as the most consistent possible with these data.

In general, at incident energy of 14.5 MeV the three measurements are fairly consistent with each other and the calculation is smaller than the data at some gamma-ray energies. At this incident neutron energy, the gamma rays produced in the $(n,2n)$ reaction have fairly large contribution for $E_\gamma < 0.5$ MeV, a gamma-ray energy region that has only two data points from the measurement of Drake et al. (DR78) and is not covered by the experiments of Dickens et al. (DI73) or Shin et al. (SH80). The same pattern holds between calculation and experiment for the gamma-ray spectra at incident energies of 5.5 and 9.5 MeV. At these two energies, there are significant contributions from the (n,p) reactions for $E_\gamma < 0.5$ MeV which are not covered by the measurements.

5. COMPARISON OF CALCULATION WITH ENDF/B-V

The TNG calculations are compared to a representative set of cross sections from the ENDF/B-V for nickel (MAT 1328) in Figs. 91 through 101. In each figure, the curves labeled "TNG Calculation" include the sum of the calculated cross sections for ^{58}Ni (multiplied by 0.71) and ^{60}Ni (multiplied by 0.29). Comparison of the total inelastic scattering cross section is given in Fig. 91. The total integrated yield of secondary neutrons as a function of incident neutron energy is shown in Fig. 92. Although the agreement appears quite reasonable in Fig. 92, a look at the neutron emission spectra for incident neutron energies of 5.5, 9.5, and 14.5 in Figs. 93 through 95 reveals significant differences. The evaluated spectra for $E_n = 14.5$ MeV do not project enough high-energy secondary neutrons. This lack can be understood because the ENDF/B-V evaluation does not include a precompound component. It should be noted that the elastic cross section has not been included in Figs. 92 through 95. Comparison of the (n,p) and (n,α) cross sections are given in Figs. 96 and 97, respectively.

Differences are seen when comparing the TNG calculations for gamma rays with the ENDF/B-V values as shown in Figs. 98-101. The total integrated yields of secondary gamma rays from the calculations and from ENDF/B-V are shown in Fig. 98. The computed gamma-ray production cross sections are compared to ENDF/B-V for incident neutron energies of 5.5, 9.5, and 14.5 MeV in Figs. 99-101. In these plots, the secondary spectra were smeared by a Gaussian function; for clarity the broader resolution width due to Morgan (MO79) was used. The ENDF/B-V evaluation used the data of Dickens (DI73) that were shown in Figs. 86 through 88. As mentioned previously, the TNG calculation shows that gamma rays produced in the (n,p) and $(n,2n)$ reactions are significant for $E_\gamma < 0.5$ MeV, a gamma-ray energy region not represented in ENDF/B-V.

6. SUMMARY

This report has presented the nuclear models and parameters used in computing neutron-induced reactions on $^{58,60}\text{Ni}$ between 1 and 20 MeV. The calculations were made using the multistep Hauser-Feshbach/precompound model code TNG. Input parameters for TNG, including optical-model sets, discrete level information, level-density parameters, giant dipole resonance parameters and direct reaction model parameters, were discussed. Once the input parameters were determined for TNG no other parameter adjustments were performed in the model calculations for any of the incident neutron energies for which reactions were computed. The resulting calculated cross-section sets are consistent and energy balance is ensured.

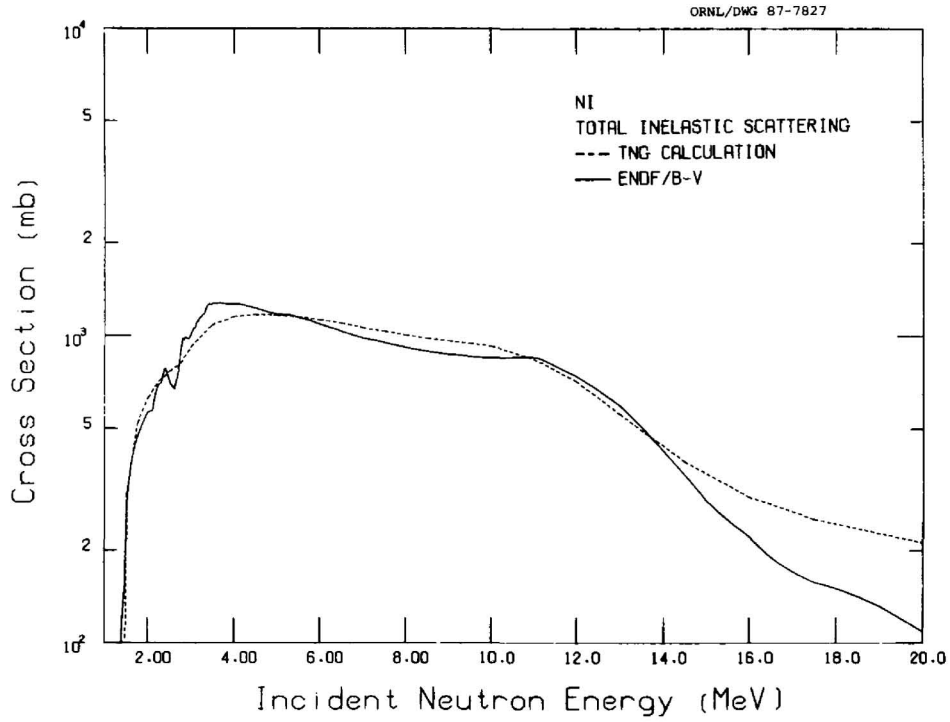


Fig. 91. Comparison of the TNG calculation with ENDF/B-V for the total inelastic scattering cross section.

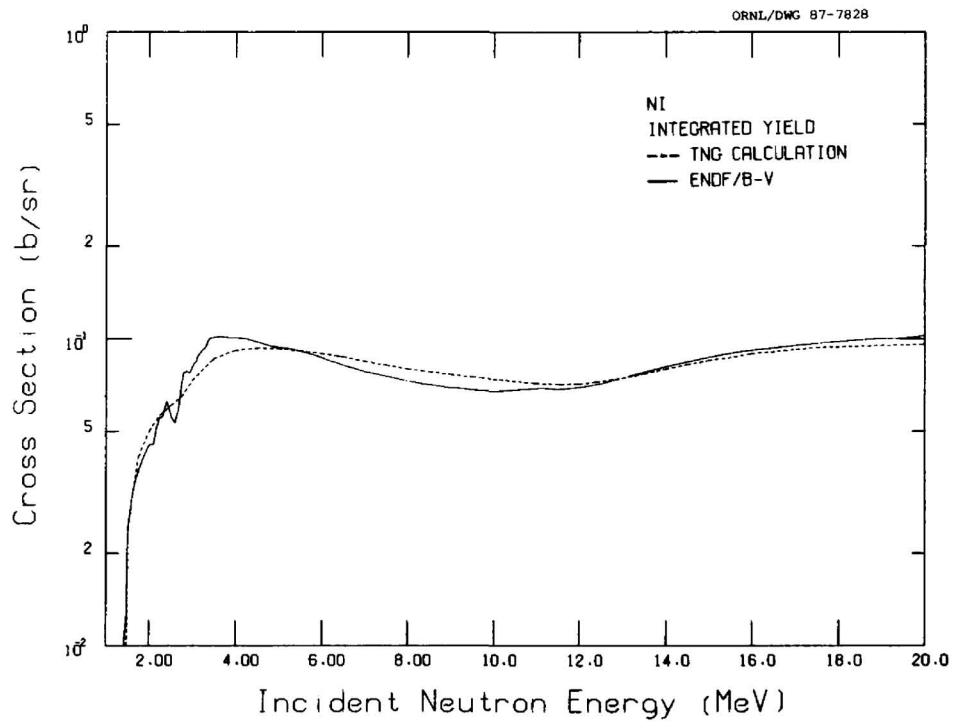


Fig. 92. Comparison of the TNG calculation with ENDF/B-V for the integrated yield of secondary neutrons as a function of incident neutron energy. The elastic contribution is not included.

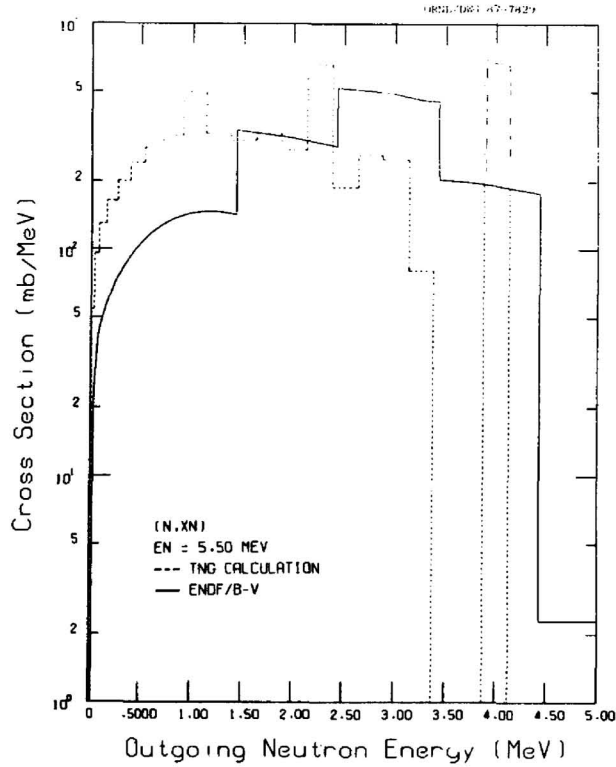


Fig. 93. Comparison of (n,xn) from ENDF/B-V with the TNG calculation for incident neutron energy of 5.5 MeV.

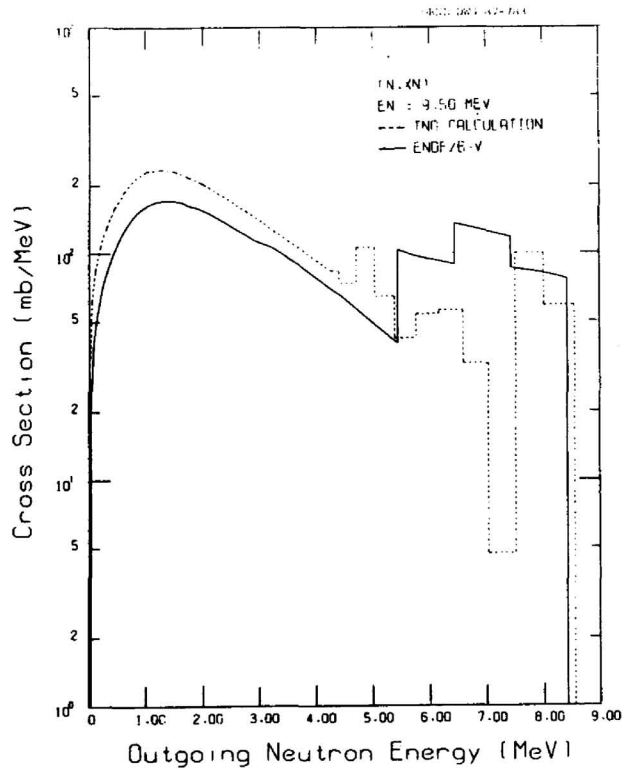


Fig. 94. Comparison of (n,xn) from ENDF/B-V with the TNG calculation for incident neutron energy of 9.5 MeV.

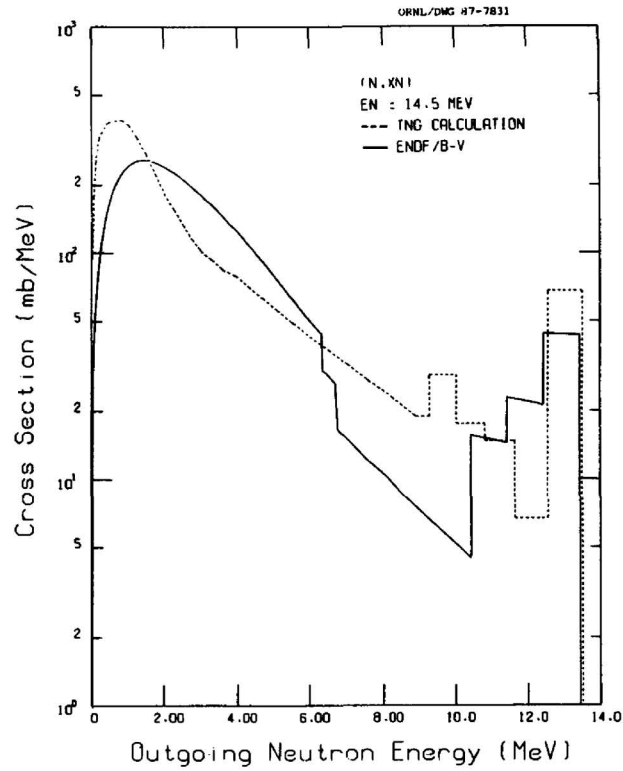


Fig. 95. Comparison of (n,xn) from ENDF/B-V with the TNG calculation for incident neutron energy of 14.5 MeV.

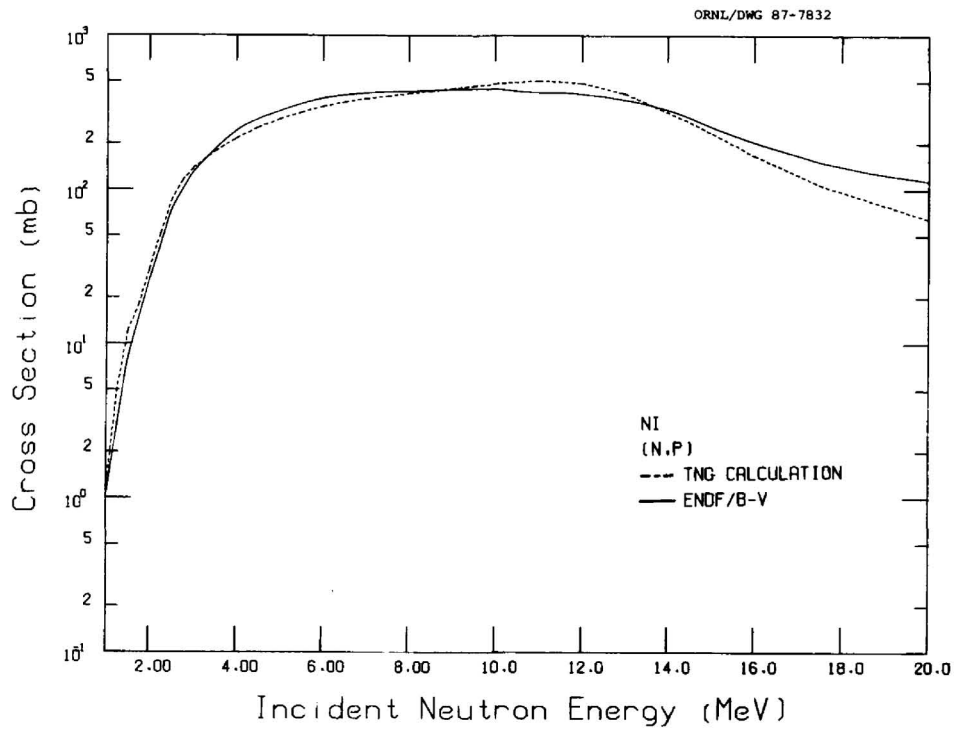


Fig. 96. Comparison of the TNG calculation with ENDF/B-V for the (n,p) cross section.

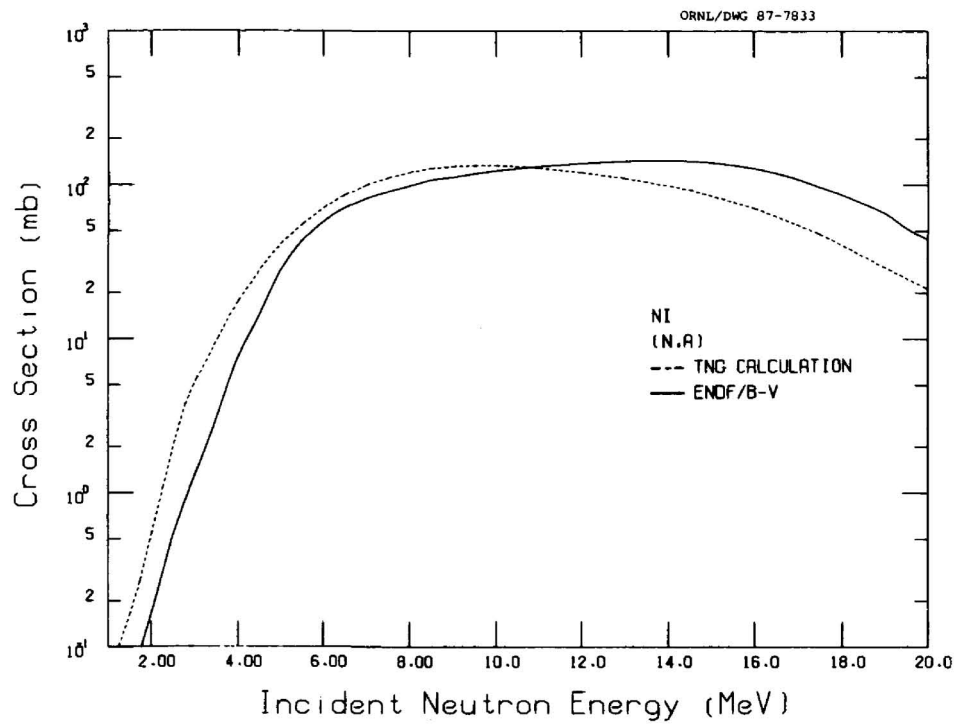


Fig. 97. Comparison of the TNG calculation with ENDF/B-V for the (n,α) cross section.

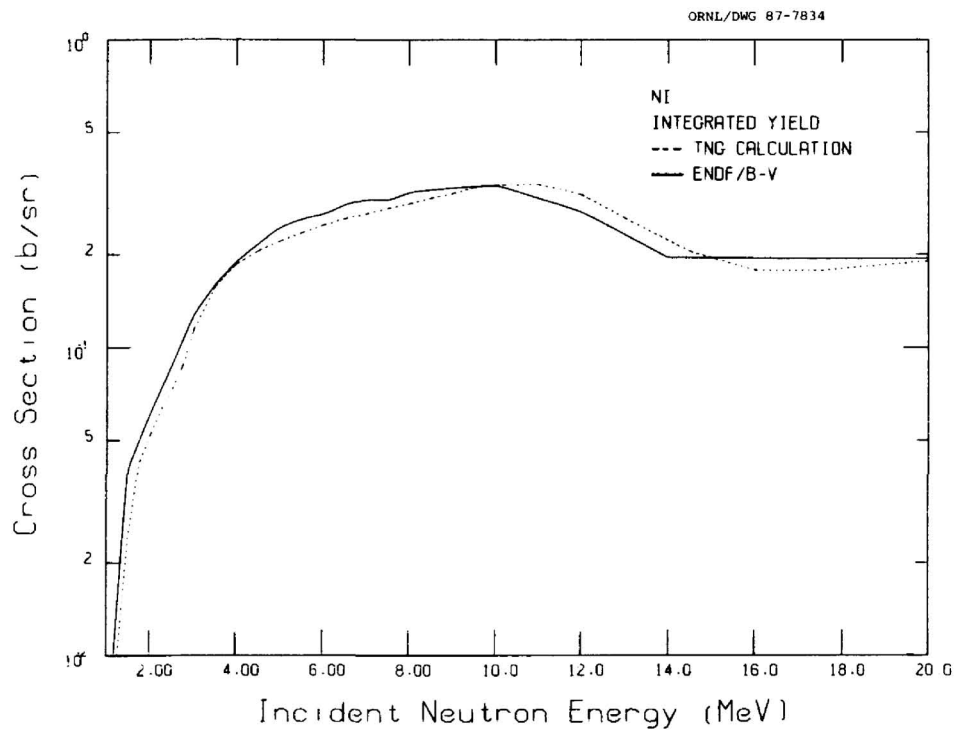


Fig. 98. Comparison of the TNG calculation with ENDF/B-V for the integrated yield of secondary gamma rays as a function of incident neutron energy.

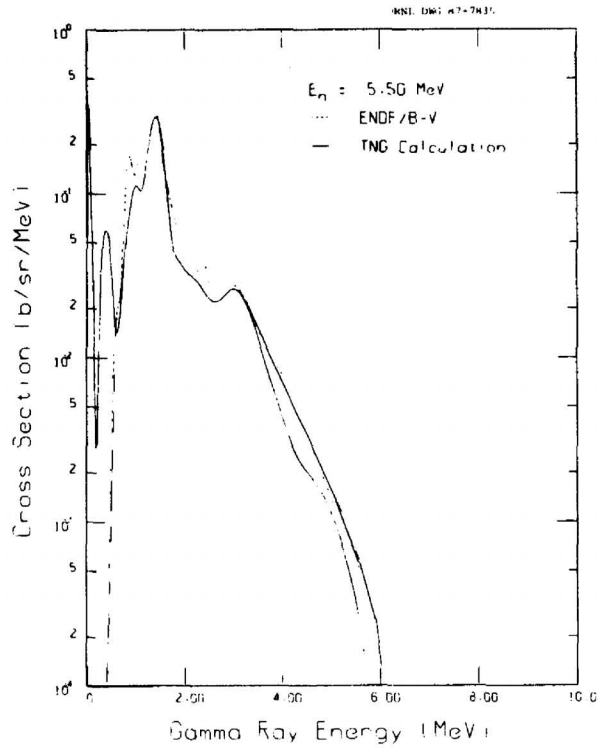


Fig. 99. Comparison of (n,γ) from ENDF/B-V with the TNG calculation for incident neutron energy of 5.5 MeV.

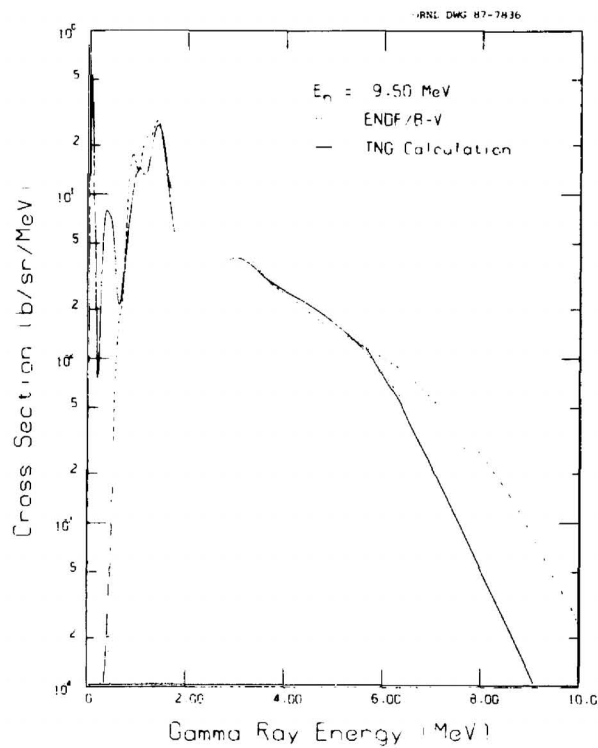


Fig. 100. Comparison of (n,γ) from ENDF/B-V with the TNG calculation for incident neutron energy of 9.5 MeV.

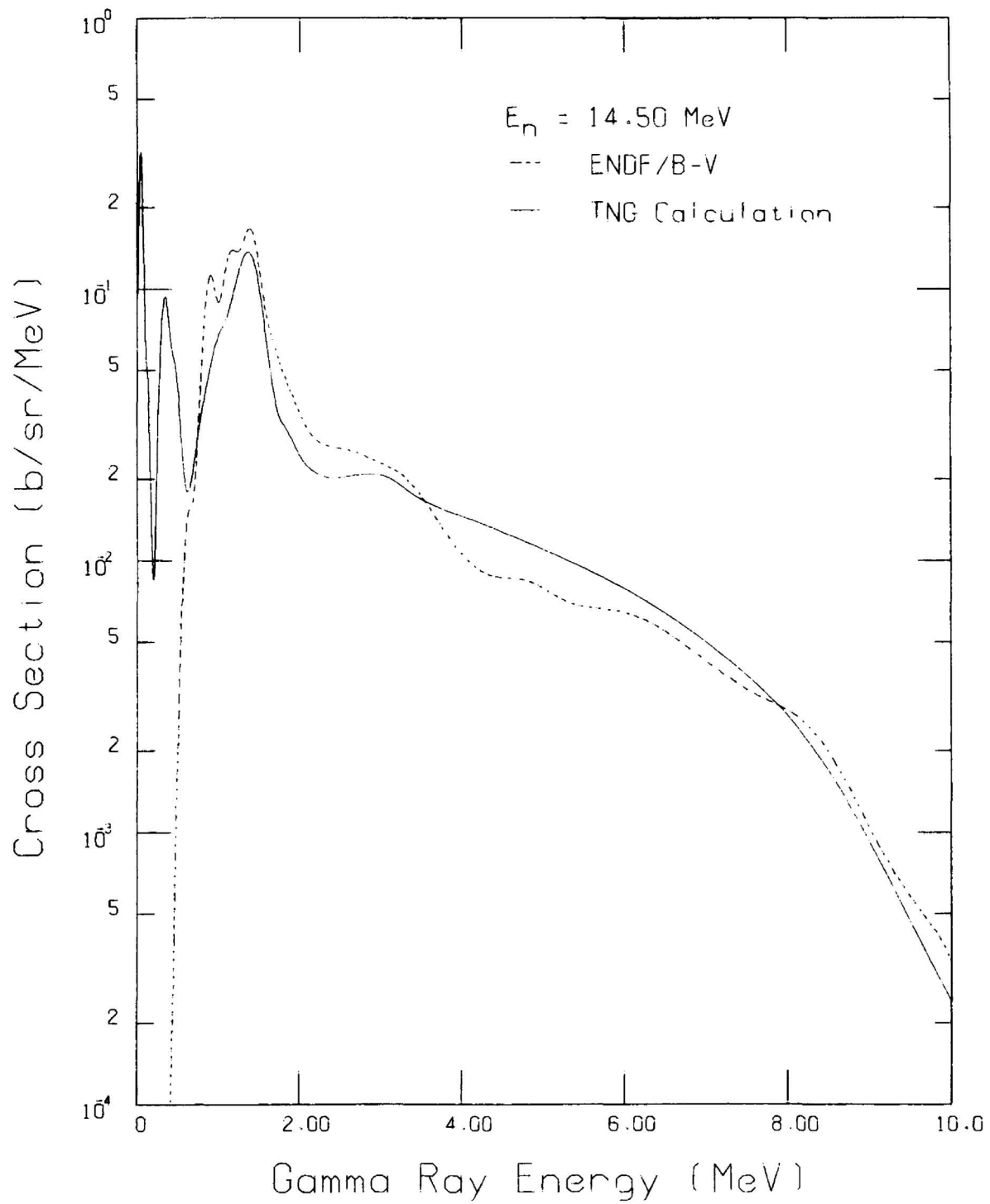


Fig. 101. Comparison of $(n, x\gamma)$ from ENDF/B-V with the TNG calculation for incident neutron energy of 14.5 MeV.

Calculated results were compared extensively to available measured data. The overall quality of the comparisons leads to the acceptance of the TNG calculations as reliable, especially for those reactions for which little or no measured data exist; for example, energy-angular distributions of the continuum neutrons for all E_n except 14.5 MeV. Also, it should be recognized from the comparisons that TNG can be used to resolve discrepancies among experimental data sets. The present work verifies that advanced nuclear-model codes can lead to internally consistent evaluations that are in good overall agreement with measured data.

The computed data were compared to cross sections from the current ENDF/B-V evaluation for Ni. The comparisons reveal serious problems in the current ENDF/B-V evaluation for natural nickel neutron-emission cross sections and spectra, as well as gamma-ray production cross sections and spectra. These problems probably lead to difficulties with energy balance in the ENDF/B-V Ni evaluation, which can cause erroneous results for the KERMA (Kinetic Energy Release in Material) factor, as noted by FU (FU80b).

REFERENCES

- AB62 A. I. Abramov, *Atomnaja Energija* **12**, 62 (1962).
- AL61 D. L. Allan, *Nucl. Phys.* **24**, 274 (1961).
- AL72 K. R. Alvar, *Nucl. Phys.* **A195**, 289 (1972).
- AS58 V. J. Ashby, H. C. Catron, L. L. Newkirk, and C. J. Taylor, *Second Internat. At. En. Conf., Geneva* **15**, 3 (2494) (September 1958).
- AU77 G. F. Auchampaugh, D. M. Drake, and L.R. Veesser, "Neutron Cross Section Programs in the Energy Region from 1 to 24 MeV at the LASL Van de Graaff Facilities," *Symp. on Neutron Cross Sections from 10 to 40 MeV, Upton, N.Y., May 3-5, 1977*, BNL-NCS-50681, p. 231, Brookhaven National Laboratory.
- AU77a R. L. Auble, *Nuclear Data Sheets* **20**, 253 (1977).
- AU79 R. L. Auble, *Nuclear Data Sheets* **28**, 103 (1979).
- BA62 J. F. Barry, *J. Nucl. Energy* **16**, 467 (1962).
- BA63 R. W. Bauer, J. D. Anderson, and L. J. Christensen, *Nucl. Phys.* **48**, 152 (September 1963).
- BA74 F. T. Baker, S. Davis, C. Glashauser, and A. B. Robbins, *Nucl. Phys.* **A233**, 409-424 (1974).
- BE55 J. R. Beyster, R. L. Henkel, R. A. Nobles, and J. M. Kister, *Phys. Rev.* **98**, 1216 (June 1955).
- BE56 J. R. Beyster, M. Walt, E. W. Salmi, *Phys. Rev.* **104**, 1319 (1956).
- BE66 T. S. Belanova, A. A. Vankov, F. F. Mikhailus, and Yu. Ya. Stavisskii, *Nuclear Data for Reactors Conf., Paris (17-21 Oct. 1976)*. Published by IAEA, Vienna, STI/PUB/140 I,455(96) (1967).
- BE69 F. D. Becchetti and G. W. Greenlees, *Phys. Rev.* **182**, 1190 (1969).
- BE83 Z. W. Bell, J. K. Dickens, D. C. Larson, and J. H. Todd, *Nucl. Sci. Eng.* **84**, 12 (1983).
- BH74 M. R. Bhat, *Neutron and Gamma-Ray Production Cross-Sections for Nickel*, BNL 50435 (ENDF-207) (1974).
- BI75 T. Biro, S. Sudar, J. Csikai, and Z. Dezso, *J. Inorg. Nucl. Chem.* **37**, 1583 (1975).

- BO66 M. Bormann, F. Dreyer, and U. Zielinski, *Reports from Euratom to European-American Nuclear Data Committee Documents -66*, 42 (February 1966).
- BO67 M. Bormann, F. Dreyer, H. Neuert, I. Riehle, and U. Zielinski, *Nuclear Data for Reactors Conf. 1*, 225 (1967).
- BO71 P. Boschung, J. T. Lindow, and E. F. Shrader, *Nucl. Phys. A161*, 593 (February 1971).
- BR64 D. L. Broder, V. E. Kolesov, A. I. Lashuk, I. P. Sadokhin, and A. G. Dovbenko, *Atomnaja Energija 16*, (2), 103 (February 1964).
- BR64a D. L. Broder, A. I. Lashuk, and I. P. Sadokhin, ANL-Trans-177 (1964).
- BR70 D. L. Broder, A. F. Gamalii, A. I. Lashuk, and I. P. Sadokhin, *Second Int. Conf. on Nuclear Data for Reactors, Helsinki, 2*, 359 (1970).
- BR71 W. Breunlich and G. Stengel, *Z. Naturforsch. A 26*, 451 (March 1971).
- BR78 E. Browne, J. M. Dairiki, R. E. Doebler, A. A. Shihab-Eldin, L. J. Jardine, J. K. Tuli, and A. B. Buyrn, *Table of Isotopes*, Seventh Edition, Edited by C. M. Lederer and V. S. Shirley, John Wiley and Sons, Inc., New York (1978).
- BU82 C. Budtz-Jorgensen, P. T. Guenther, A. B. Smith, and J. F. Whaler, *Zeitschrift Fuer Physik A306*, 265 (August 1982).
- CH65 S. Chojnacki, P. Decowski, E. Gierlik, W. Grochulski, A. Marcinkowski, K. Siwek, I. Sledzinska, and Z. Wilhelmi, *Inst. Badan Jad. (Nucl. Res.)* - 680 (December 1965).
- CH83 P. R. Christensen, S. Pontoppidan, F. Videbaek, P. D. Bond, Ole Hansen, C. E. Thorn, M. J. LeVine, and J. Cheng-Lie, *Phys. Rev. C28*, 159 (1983).
- CL67 R. L. Clarke and W. G. Cross, *Nucl. Phys. A95*, 320 (April 1967).
- CL72 G. Clayeux and J. Voignier, *Centre d' Etudes de Limeil*, CEA-R-4279 (1972).
- CO62 L. Colli, I. Iori, S. Micheletti, and M. Pignanelli, *Nuovo Cimento 21*, 966 (1962).
- CR63 W. G. Cross, R. L. Clarke, K. Morin, G. Slinn, N. M. Ahmed, and K. Beg, *Canadian Reports to European-American Nuclear Data Committee Documents - 16,1* (January 1963).
- CS82 J. Csikai, *Int. Conf. on Nuclear Data for Science and Technology, Antwerp (B27)* (September 1982).
- CS86 CSISRS Library, National Nuclear Data Center, Brookhaven National Laboratory, Upton, New York 11973.
- DE68 P. Decowski, W. Grochulski, A. Marcinkowski, K. Siwek, I. Sledzinska, and Z. Wilhelmi, *Nucl. Phys. A112*, 513 (May 1968).
- DI60 B. C. Diven, J. Terrell, A. Hemmendinger, *Phys. Rev. 120*, 556 (October 1960).
- DI73 J. K. Dickens, T. A. Love, and G. L. Morgan, *Gamma-Ray Production From Neutron Interactions with Nickel for Incident Neutron Energies Between 1.0 and 10 MeV: Tabulated Differential Cross Sections*, ORNL/TM-4379 (November 1973).
- DI79 M. Divadeenam, *Ni Elemental Neutron Induced Reaction Cross-Section Evaluation*, BNL-NCS-51346, ENDF-294 (1979).
- DJ82 A. Djaloeis, C. Alderliesten, J. Bojowald, W. Oelert, and P. Turek, *Physica Scripta 26*, 46-50 (1982).
- DR78 D. M. Drake, E. D. Arthur, and M. G. Silbert, *Nucl. Sci. Eng. 15*, 54 (1978).
- EK83 L. P. Ekström and J. Lyttkens, *Nuclear Data Sheets 38*, 463 (1983).

- ET73 M. A. Etemad, *Aktiebolaget Atomenergi- 481*, Stockholm/Studsvik (December 1973).
- FA68 U. Facchini and E. Saetta-Menichella, *Energia Nucleare* **15**, 54 (1968).
- FI84 R. Fischer, G. Traxler, M. Uhl, and H. Vonach, *Phys. Rev.* **C30**, 72 (1984).
- FU72 I. Fujita, M. Sonoda, A. Katase, Y. Wakuta, H. Tawara, M. Hyakutake, and K. Iwatani, *J. Nucl. Sci. and Tech.* **9**, 301 (1972).
- FU73 E. G. Fuller, H. M. Gerstenberg, H. Vander Molen, and T. C. Dunn, "Photonuclear Reaction Data, 1973," U.S. Dept. of Commerce, National Bureau of Standards (March 1973).
- FU76 C. Y. Fu, *Atomic Data and Nuclear Data Tables*, **17**, 127 (1976).
- FU78 K. Fukuda, K. Matsuo, S. Shirahama, and I. Kumabe, *Japanese Reports to Nucl. En. Agency Nuclear Data Committee Documents - 56/U*, 44 (September 1978).
- FU80 C. Y. Fu, "A Consistent Nuclear Model for Compound and Precompound Reactions with Conservation of Angular Momentum," *Proc. Int. Conf. Nuclear Cross Sections for Technology, Knoxville, TN, Oct. 22-26, 1979*, NBS-594, p. 757, U.S. National Bureau of Standards. Also, ORNL/TM-7042 (1980).
- FU80a C. Y. Fu, "Development and Applications of Multi-Step Hauser-Feshbach/Pre-Equilibrium Model Theory," *Symp. Neutron Cross Sections from 10 to 50 MeV, Upton, NY, May 12-14, 1980*, BNL-NCS-51425, p. 675, Brookhaven National Laboratory.
- FU80b C. Y. Fu, "Evaluation of Photon Production from Neutron-Induced Reactions," *Proc. of the Conference on Nuclear Data Evaluation Methods and Procedures, Upton, NY, September 22-25, 1980*, BNL-NCS-51363, Vol. II, p. 753, Brookhaven National Laboratory.
- FU82 C. Y. Fu and D. M. Hetrick, "Experience in Using the Covariances of Some ENDF/B-V Dosimetry Cross Sections: Proposed Improvements and Addition of Cross-Reaction Covariances," *Proc. Fourth ASTM-EURATOM Symp. on Reactor Dosimetry, Gaithersburg, Maryland, March 22-26, 1982*, p. 877, U.S. National Bureau of Standards.
- GI61 J. H. Gibbons, R. L. Macklin, P. D. Miller, and J. H. Neiler, *Phys. Rev.* **122**, 2695 (1961).
- GI65 A. Gilbert and A.G.W. Cameron, *Can. J. of Phys.* **43**, 1446-1477 (1965).
- GL61 R. N. Glover and K. H. Purser, *Nucl. Phys.* **24**, 431 (1961).
- GL62 R. N. Glover and E. Weigold, *Nucl. Phys.* **29**, 309 (1962).
- GO60 L. Gonzalez, J. Rapaport, and J. J. Van Loef, *Phys. Rev.* **120**, 1319 (November 1960).
- GR74 G. Grenier, B. Duchemin, and D. Paricot, Centre D'Etudes Nucleaires, Saclay, Report-4634 (November 1974).
- GR79 S. M. Grimes, R. C. Haight, K. R. Alvar, H. H. Barschall, and R. R. Borchers, *Phys. Rev. C*.
- HA73 L. F. Hansen, J. D. Anderson, S. M. Grimes, J. L. Kammerdiener, T. Komoto, C. M. Logan, Report, U.S. Nuclear Data Committee - 9, 84 (November 1973).
- HA77 R. C. Haight and S. M. Grimes, Lawrence Livermore Laboratory, Report UCRL-80235 (1977).
- HA81 Ole Hansen, F. Videbaek, E. R. Flynn, J. C. Peng, and J. A. Cizewski, *Nucl. Phys.* **A364**, 144-158 (1981).
- HA82 R. C. Harper and W. L. Alford, *J. Phys. G: Nucl. Phys.* **8**, 153-160 (1982).
- HA82a L.Han-Lin, H. Jian-Zhou, F. Pei-Guo, C. Yun-Feng, and Z. Wen-Rong, IAEA - Nucl. Data Services - 30637 (July 1982).

- HA83 Ole Hansen, P. D. Bond, S. Kubono, M. J. LeVine, and C. E. Thorn, *Nucl. Phys.* **A398**, 325-342 (1983).
- HE73 J. D. Hemingway, *J. Nucl. Energy* **27**, 241 (April 1973).
- HE75 D. Hermsdorf, A. Meister, S. Sassonoff, D. Seeliger, K. Seidel, and F. Shahin, Zentralinstitut Fur Kernforschung Rossendorf Bei Dresden, Zfk-277 (U) (1975).
- HE79 D. M. Hetrick, D. C. Larson, and C. Y. Fu, *Status of ENDF/B-V Neutron Emission Spectra Induced by 14-MeV Neutrons*, ORNL/TM-6637, ENDF-280 (April 1979).
- HO67 B. Holmqvist and T. Wiedling, Aktiebolaget Atomenergi - 303, Stockholm/Studsvik (December 1967).
- HO69 B. Holmqvist and T. Wiedling, Aktiebolaget Atomenergi - 366, Stockholm/Studsvik (June 1969).
- HO70 B. Holmqvist, S. G. Johansson, G. Lodin, M. Salama, and T. Wiedling, Aktiebolaget Atomenergi - 385, Stockholm/Studsvik (September 1970).
- HU62 J. R. Huizenga and G. Igo, *Nucl. Phys.* **29**, 462-473 (1962).
- HU78 C. G. Hudson, W. L. Alford, and S. K. Ghorai, *Ann. of Nucl. Energy* **5**, 589 (1978).
- IN68 M. Inoue, *Nucl. Phys.* **A119**, 449 (1968).
- IN81 A. Ingemarsson, T. Johansson, and G. Tibell, *Nucl. Phys.* **A365**, 426-456 (1981).
- JA67 O. N. Jarvis, B. G. Harvey, D. L. Hendrie, and J. Mahoney, *Nucl. Phys.* **A102**, 625 (1967).
- JO65 R. K. Jolly, *Phys. Rev.* **139**, B318 (1965).
- JO69a R. K. Jolly, M. D. Goldberg, and A. K. Sengupta, *Nucl. Phys.* **A123**, 54 (1969).
- JO69 B. Joensson, K. Nyberg, and I. Bergqvist, *Ark. Fys.* **39**, 295 (1969).
- KA63 S. V. Kapchigashev and Yu. P. Popov, *Atomnaja Energija* **15**, 120 (1963).
- KA65 L. Ya. Kasakov, V. F. Kolesov, V. I. Popov, O. A. Salnikov, V. M. Sluhevskaja, and V. I. Trikova, *Proc. Nucl. Structure Conf., Antwerp*, **576** (200) (1965).
- KI74 W. E. Kinney and F. G. Perey, *Natural Nickel and ⁶⁰Ni Neutron Elastic and Inelastic Scattering Cross Sections from 4.07 to 8.56 MeV*, ORNL-4807 (January 1974).
- KI76 H. J. Kim, *Nuclear Data Sheets* **17**, 485 (1976).
- KI85 Y. Kikuchi and N. Sekine, *Evaluation of Neutron Nuclear Data of Natural Nickel and Its Isotopes For JENDF-2*, Report JAERI-M 85-101 (July 1985).
- KN86 D. W. Kneff, B. M. Oliver, H. Farrar IV, and L. R. Greenwood, *Nucl. Sci. Eng.* **92**, 491-524 (1986).
- KO63 J. Konijn and A. Lauber, *Nucl. Phys.* **48**, 191 (October 1963).
- KO67 I. A. Korzh, V. A. Mischenko, M. V. Pasechnik, N. M. Pravdivy, I. E. Sanzhur, and I. A. Totsky, *Ukr. Fig. Zh.* **12**, (9), 1571 (September 1967).
- KO71 E. S. Konobeevskij, R. M. Musaelyan, V. I. Popov, and I. V. Surkova, *Izv. Akad. Nauk. SSSR, Ser. Fiz.* **35**, (11), 23, 45 (November 1971).
- KO71a I. A. Korzh, T. A. Kostjuk, V. A. Mishchenko, N. M. Pravdivy, and I. E. Sanzhur, *Izv. Akad. Nauk SSSR, Ser. Fiz.* **35**, (4), 823 (April 1971).

- KO76 I. A. Korzh, V. A. Mishchenko, E. N. Mozhzhukhin, A. A. Golubova, N. M. Pravdivy, I. E. Sanzhur, and M. V. Pasechnik, *All Union Conf. on Neutron Phys., Kiev, published in Nejtronnaja Fizika*, **4**, 220 (May 1976).
- KO76a D. C. Kocher and R. L. Auble, *Nuclear Data Sheets* **19**, 445 (1976).
- KO76b D. C. Kocher, *Nuclear Data Sheets* **18**, 463 (1976).
- KU60 I. Kumabe and R. W. Fink, *Nucl. Phys.* **15**, 316 (February 1960).
- KU72 P. D. Kunz, "Distorted Wave Code DWUCK72," University of Colorado, unpublished (1972).
- LA80 D. C. Larson, "ORELA Measurements to Meet Fusion Energy Neutron Cross Section Needs," *Proc. Symp. on Neutron Cross Sections from 10 to 50 MeV*, BNL-NCS-51245, Brookhaven National Laboratory (July 1980).
- LA85 D. C. Larson, "High-Resolution Structural Material ($n, x\gamma$) Production Cross Sections for $0.2 < E_n \leq 40$ MeV," *Proc. Conf. on Nucl. Data for Basic and Applied Science, Santa Fe, New Mexico*, **1**, 71 (1985).
- MA57 M. H. MacGregor, W. P. Ball, and R. Booth, *Phys. Rev.* **108**, 726 (1957).
- MA59 M. K. Machwe, D. W. Kent, Jr., and S. C. Snowdon, *Phys. Rev.* **114**, 1563 (1959).
- MA67 R. L. Macklin and J. H. Gibbons, *Phys. Rev.* **159**, 1007 (1967).
- MA69 S. C. Mathur, P. S. Buchanan, and I. L. Morgan, *Phys. Rev.* **186**, 1038 (October 1969).
- MA72 G. N. Maslov, F. Nasyrov, and N. F. Pashkin, *Jadernye Konstanty* -9, 50 (1972).
- MA72a S.G. Malmkog, Aktiebolaget Atomenergi, Stockholm, Prog. Report -444, 2 (January 1972).
- ME63 J. W. Meadows and J. F. Whalen, *Phys. Rev.* **130**, 2022 (1963).
- MO79 G. L. Morgan, *Cross Sections for the Cu(n, xn) and Cu($n, x\alpha$) Reactions Between 1 and 20 MeV*, ORNL-5499, ENDF-273 (1979).
- ND83 *Compilation of Requests for Nuclear Data*, compiled and edited by the National Nuclear Data Center for the DOE Nuclear Data Committee, BNL-NCS-51572, DOE/NDC-28/U (January 1983).
- NG80 P. N. Ngoc, S. Gueth, F. Deak, and A. Kiss, *All Union Conf. on Neutron Phys., Kiev* **1**, 259 (Sept. 15-19, 1980).
- NI65 K. Nishimura, K. Okano, and S. Kikuchi, *Nucl. Phys.* **70**, 421 (August 1965).
- OK67 S. Okumura, *Nucl. Phys.* **A93**, 74 (March 1967).
- PA55 M. V. Pasechnik, First. *U.N. Conf. on Peaceful Uses of Atomic Energy, Geneva*, **2**, 3 (P/714) (Aug. 8-20, 1955).
- PA65 A. Paulsen and H. Liskien, *Nukleonik* **7**, 117 (March 1965).
- PA67 A. Paulsen and H. Liskien, *Nukleonik* **10**, 91 (July 1967).
- PA67a A. Paulsen, *Zeitschrift Fuer Physik* **205**, 226 (August 1967).
- PA71 A. Paulsen and R. Widera, " ^{58}Ni (n, p) ^{58}Co and ^{54}Fe (n, p) ^{54}Mn Cross Section Measurements for Use as Threshold Detectors," *Proc. BNES Conf. Chemical Nuclear Data, Canterbury, U.K., September 1971*, British Nuclear Energy Society (1971).
- PA72 M. V. Pasechnik, M. B. Fedorov, and T. I. Jakovenko, Neutron Physics Conf., Kiev (1971), proc. published as *Nejtronnaja Fizika* **1**, 277 (1972).

- PA81 A. Paulsen, H. Liskien, F. Arnotte, and R. Widera, *Nucl. Sci. Eng.* **78**, (4), 377 (August 1981).
- PA82 A. Pavlik, G. Winkler, H. Vonach, A. Paulsen, and H. Liskien, *Int. Conf. on Nuclear Data for Science and Technology, Antwerp*, 400 (September 1982).
- PA85 A. Pavlik, G. Winkler, and M. Uhl, *Nucl. Sci. Eng.* **90**, 186-202 (1985).
- PE70 F. G. Perey, C. O. LeRigoleur, and W. E. Kinney, *Nickel-60 Neutron Elastic- and Inelastic-Scattering Cross Sections from 6.5 to 8.5 MeV*, ORNL-4523 (April 1970).
- PE76 C. M. Perey and F. G. Perey, *Atomic Data and Nuclear Data Tables* **17**, 1-101 (1976).
- PE83 C. M. Perey, J. A. Harvey, R. L. Macklin, and F. G. Perey, *Phys. Rev.* **27**, 2556 (1983).
- PO56 K. R. Poze and N. P. Glazkov, *Zh. Eksp. Teor. Fiz* **30**, 1017 (1956).
- PR60 J. T. Prud' Homme, I. L. Morgan, J. H. McCrary, J. B. Ashe, and O. M. Hudson, Jr., *Air Force Spec. Weap. Centre Kirtland Report -60-30* (1960).
- PR61 R. J. Prestwood and B. P. Bayhurst, *Phys. Rev.* **121**, 1438 (March 1961).
- QA76 Qaim and Molla, *Proc. of the Ninth Symp. on Fusion Tech.*, Garmisch (Pergammon, Oxford, 1976), pp. 589-595.
- QA76a S. M. Qaim and G. Stoecklin, *Nucl. Phys.* **A257**, 233 (1976).
- QA84 S. M. Qaim, R. Wolfle, M.M. Rahman, and H. Ollig, *Nucl. Sci. Eng.* **88**, 143-153 (1984).
- RA65 L. A. Rayburn and E. O. Wollen, *Nucl. Phys.* **61**, 381 (1965).
- RA81 P. Raics, F. Paszti, S. Daroczy, and S. Nagy, *Atomki (Atommag Kut. Intez.) Kozlem* **23**, 45 (June 1981).
- RI76 C. Le Rigoleur, A. Arnaud, and J. Taste, *Centre D'Etudes Nucleaires, Saclay, Report -4788* (October 1976).
- RO67 W. L. Rodgers, E. F. Shrader, and J. T. Lindow, *Chicago Operations Office, AEC Report C00-1573-33, 2* (1967).
- RO71 V. C. Rogers, L. E. Beghian, F. M. Clikeman, and F. S. Mahoney, *Nucl. Sci. Eng.* **45**, 297 (September 1971).
- SA70 O. A. Salnikov, G. N. Lovchikova, G. V. Kotelnikova, N. I. Fetisov, and A. M. Trufanov, *Second Int. Conf. on Nuclear Data for Reactors, Helsinki, 2*, 359 (1970).
- SA72 O. A. Salnikov, G. N. Lovchikova, G. V. Kotelnikova, A. M. Trufanov, and N. I. Fetisov, *Differential Cross Sections of Inelastic Scattering Neutrons on Nuclei Cr, Mn, Fe, Co, Ni, Cu, Y, Zr, Nb, W, Bi*, Report *Jadernye Konstanty -7*, 102 (March 1972).
- SE68 U. Seebeck and M. Bormann, *Nucl. Phys.* **68**, 387 (1965).
- SH80 K. Shin, T. Hasegawa, and T. Hyodo, *Nucl. Sci. and Tech.* **17**, 7, 531 (July 1980).
- SH86 K. Shibata and C. Y. Fu, *Recent Improvements of the TNG Statistical Model Code*, ORNL/TM-10093 (August 1986).
- SM75 D. L. Smith and J. W. Meadows, *Nucl. Sci. Eng.* **58**, 314 (November 1975).
- SM81 A. B. Smith, P. T. Guenther, and J. F. Whalen, *Nucl. Sci. Eng.* **77**, 110 (1981).
- SO73 L. S. Sokolov, M. B. Fjodorov, E. V. Korbetskij, N. T. Surovitskaja, T. I. Jakovenko, *Ukr. Fiz. Zh.* **18**, (2), 263 (February 1973).
- SP68 L. M. Spitz, E. Barnard, and F. D. Brooks, *Nucl. Phys.* **A121**, 655 (December 1968).

- ST56 V. I. Strizhak, *Zh. Eksp. Teor. Fiz.* **31**, 907 (1956).
- ST57 V. I. Strizhak, *Atomnaja Energija* **2**(1), 68 (January 1957).
- ST61 Yu. Ya Stavisskii and A. V. Shapar, *Atomnaja Energija* **10**, 264 (1961).
- ST71 R. G. Stieglitz, R. W. Hockenbury, and R. C. Block, *Nucl. Phys.* **A163**, 592 (1971).
- SU79 S. Sudar and J. Csikai, *Nucl. Phys.* **A319**, 157 (1979).
- TA55 H. L. Taylor, O. Lonsjo, and T. W. Bonner, *Phys. Rev.* **100**, 174 (1955).
- TA83 A. Takahashi, J. Yamamoto, T. Murakami, K. Oshima, H. Oda, K. Fujimoto, M. Ueda, M. Fukazawa, Y. Yanagi, J. Mizaguchi, and K. Sumita, Oktavian Report A-83-01, Osaka University, Japan (June 1983).
- TE68 J. K. Temperley, *Nucl. Sci. Eng.* **32**, 195 (1968).
- TE75 G. Tessler and S. Glickstein, *Proc. Conf. on Nuclear Cross Sections and Technology, Washington, D.C.*, **2**, 934 (March 1975).
- TO67 J. H. Towle and R. O. Owens, *Nucl. Phys.* **A100**, 257 (1967).
- TR69 S. Traiforos, A. Mittler, W. A. Schier, B. K. Barnes, L. E. Beghian, and P. Harihar, *Nucl. Sci. Eng.* **72**, 191 (1979).
- TS69 K. Tsukada, S. Tanaka, Y. Tomita, and M. Maruyama, *Nucl. Phys.* **A125**, 641 (March 1969).
- VE78 H. Verheul and R. L. Auble, *Nuclear Data Sheets* **23**, 455 (1978).
- VI82 M. Viennot, A. Ait Haddou, A. Chiadli, and G. Paic, *Int. Conf. on Nuclear Data for Science and Technology, Antwerp*, 406 (September 1982).
- VO75 F. Voss, S. Cierjacks, D. Erbe, and G. Scmalz, *Proc. Conf. on Nuclear Cross Sections and Technology, Washington, D.C.*, **2**, 916 (March 1975).
- VO80 H. Vonach, A. Chalupka, F. Wenninger, and G. Staffel, "Measurement of the Angle-Integrated Secondary Neutron Spectra from Interaction of 14 MeV Neutrons with Medium and Heavy Nuclei," *Proc. Symp. on Neutron Cross-Sections from 10 to 50 MeV*, BNL-NCS-51245, Brookhaven National Laboratory (July 1980).
- WA54 M. Walt and H. H. Barschall, *Phys. Rev.* **93**, 1062 (March, 1954).
- WE75 H. Weigel, R. Michel, and W. Herr, *Radiochimica Acta* **22**, 11 (1975).
- WI64 D. Wilmore and P. E. Hodgson, *Nucl. Phys.* **55**, 673 (1964).
- WI80 C. Williamson, A. Galonsky, R. Huffman, and R. Markham, *Phys. Rev.* **C21**, 1344 (1980).
- WI82 G. Winkler, A. Pavlik, and H. Vonach, *Proc. Int. Conf. on Nuclear Data for Science and Technology*, 400 (September 1982).
- WU77 M. W. Wu and J. C. Chou, *Nucl. Sci. Eng.* **63**, 268 (July 1977).
- XI82 S. Xiamin, W. Yongshun, S. Ronglin, X. Jinqiang, and D. Dazhav, *Proc. Int. Conf. on Nuclear Data for Science and Technology, Antwerp*, 373 (Sept. 6-10, 1982).
- YA78 Yamamoto et al., *Nucl. Sci. and Tech.* **15**, 797 (November 1978).
- YO85 P. G. Young, "Global and Local Optical Model Parameterizations," pp. 127-45 in *NEA Nuclear Data Committee report NEANDC-222 'U', Paris*, (1985).

INTERNAL DISTRIBUTION

- | | | | |
|--------|---|-----|---------------------------------|
| 1. | R. G. Alsmiller, Jr. | 28. | R. W. Roussin |
| 2. | H. P. Carter/G. E. Whitesides/
CS X-10 library | 29. | R. T. Santoro |
| 3. | J. K. Dickens | 30. | R. R. Spencer |
| 4-8. | C. Y. Fu | 31. | A. Zucker |
| 9. | T. A. Gabriel | 32. | P. W. Dickson, Jr. (consultant) |
| 10-14. | D. M. Hetrick | 33. | G. H. Golub (consultant) |
| 15. | J. T. Holdeman | 34. | R. M. Haralick (consultant) |
| 16-20. | D. C. Larson | 35. | D. Steiner (consultant) |
| 21. | N. M. Larson | 36. | Central Research Library |
| 22. | F. C. Maienschein | 37. | Document Reference Section |
| 23. | B. F. Maskewitz | 38. | K-25 Plant Library |
| 24. | B. D. Murphy | 39. | Laboratory Records |
| 25. | M. R. Patterson | 40. | Laboratory Records - RC |
| 26. | R. W. Peelle | 41. | ORNL Patent Section |
| 27. | F. G. Perey | 42. | EPMD Reports Office |

EXTERNAL DISTRIBUTION

43. E. D. Arthur, T-2, MS-243, Los Alamos National Laboratory, P. O. Box 1663, Los Alamos, NM 87545.
44. S. E. Berk, G234, Division of Development and Technology, Office of Fusion Energy, U.S. Department of Energy, Washington, DC 20545
45. P. Rose, Building 197D, National Nuclear Data Center, Brookhaven National Laboratory, Upton, NY 11973.
46. Chief, Mathematics and Geoscience Branch, U.S. Department of Energy, Washington, DC 20545.
47. Herbert Goldstein, 211 Mudd Columbia University, 520 West 120th St., New York, NY 10027.
48. Robert MacFarlane, T-2, MS-243, Los Alamos National Laboratory, P. O. Box 1663, Los Alamos, NM 87545.
49. F. M. Mann, W/A-4, Westinghouse Hanford, P. O. Box 1970, Richland, WA 99352.
50. G. L. Morgan, Los Alamos National Laboratory, P. O. Box 1663, Group P-15, MS D406, Los Alamos, NM 87545.
51. J. N. Rogers, Division 8324, Sandia Laboratories, Livermore, CA 94550.
52. R. E. Schenter, Westinghouse Hanford, P. O. Box 1970, Richland, WA 99352.
53. D. L. Smith, Building 314, Applied Physics Division, Argonne National Laboratory, 9700 South Cass Avenue, Argonne, IL 60439.
54. S. L. Whetstone, Division of Nuclear Sciences, Office of Basic Energy Sciences, U.S. Department of Energy, Washington, DC 20545.

55. P. G. Young, T-2, MS-243, Los Alamos National Laboratory, P. O. Box 1663, Los Alamos, NM 87545.
56. Office of Assistant Manager for Energy Research and Development, U.S. Department of Energy, Oak Ridge Operations, Oak Ridge, TN 37831.
- 57-181. April Donegain, National Nuclear Data Center, ENDF, Brookhaven National Laboratory, Upton, NY 11973.
- 182-212. Technical Information Center, Oak Ridge, TN 37831.

